UC Berkeley
UC Berkeley Electronic Theses and Dissertations

Title
Isotopic dynamics of C, O and U in soils and their relation to climate

Permalink
https://escholarship.org/uc/item/5tw4j3pm

Author
Oerter, Erik

Publication Date
2015

Peer reviewed|Thesis/dissertation

eScholarship.org Powered by the California Digital Library
University of California

Isotopic dynamics of C, O and U in soils and their relation to climate

by

Erik Joseph Oerter

A dissertation submitted in partial satisfaction of the

requirements for the degree of

Doctor of Philosophy

in

Environmental Science, Policy and Management

in the

Graduate Division

of the

University of California, Berkeley

Committee in charge:

Professor Ronald G. Amundson, Chair
Professor Todd E. Dawson
Professor David L. Shuster

Spring 2015

Abstract

Isotopic dynamics of C, O and U in soils and their relation to climate

by

Erik Joseph Oerter

Doctor of Philosophy in

Environmental Science, Policy and Management

University of California, Berkeley

Professor Ronald G. Amundson, Chair

The development of soil is driven by environmental conditions, and soil properties are reflective of those conditions. Pedogenic carbonate is widespread in arid and semi-arid soils and its stable C and O isotope composition is often used as a paleoclimate indicator. However, questions remain about the precise meaning of those signals, and most importantly the season(s) that the isotopic composition most closely reflects. Chapter 1 examines the soil conditions that lead to carbonate formation, and describes research on a climosequence of four sites on Holocene soils in Fish Lake Valley, Nevada (western USA), where Mean Annual Precipitation ranges from ~80mm yr^{-1} to ~220mm yr^{-1}. Continuous measurements of soil temperature, soil volumetric water content, air temperature, and air humidity were recorded in 0.5hr intervals. Precipitation and samples of soil atmosphere from 10, 25, 50 and 100cm were collected at various intervals for CO_2 concentration, $\delta^{13}C$ and $\delta^{18}O$ values (which are a proxy for soil water $\delta^{18}O$). This climosequence indicates that the C and O stable isotope composition of soil CO_2, H_2O and carbonate change systematically with elevation and climate. At the lowest elevation site, soil carbonate $\delta^{13}C$ and $\delta^{18}O$ values reflect constant conditions nearly year round, especially in the 25-50cm soil depth interval. At the mid-elevation sites, spring through summer conditions appear to be recorded in $\delta^{13}C$ and $\delta^{18}O$ values of pedogenic carbonate. At the highest elevation site of 2602m, the C and O isotopes of carbonate never reflected the measured soil CO_2 and H_2O isotopes. These results indicate that there is inherent difficulty or complexity in assigning a definitive timing of carbonate formation based on short-term (one or two year) field measurements of soil CO_2 and H_2O, but also suggests that short-term monitoring, despite its weaknesses, helps to reveal the nature of the long term record isotopically recorded in soil carbonate.

Chapter 2 presents the first continuous millennial-scale paleoclimate reconstruction based on O, C and U isotopes in dense, laminated pedogenic carbonate. The record is from the Wind River Basin of Wyoming, and provides isotopic proxies for climate and vegetation conditions in the North American mid-continent for the last 120ka. Accurate and precise $^{230}Th/U$ ages were obtained from laser ablation ICP-MS spots of 93um diameter size. The resulting carbonate growth calculations indicate that ~100μm sampling regions represent 10ka to 0.1ka at growth

rates of 10 to 1000μm ka^{-1}. The U-series transects were coupled to $\delta^{13}C$ and $\delta^{18}O$ values obtained by ion probe on 10um diameter spots. Modern soil carbonate in the region has $\delta^{18}O$ and $\delta^{13}C$ values that are similar to the youngest (early Holocene) samples acquired in the laminations, strengthening the interpretation that the carbonate reflects soil isotopic conditions at the time of formation. The carbonate lamination record from 120 to 80ka is somewhat sparse due to slowly forming carbonate, but records conditions that change in phase with summer solar insolation, and indicate that relatively warm and dry conditions prevailed during the penultimate deglaciation and last interglacial period. The paleoclimate signal in the soil carbonate $\delta^{18}O$ values during this time period are similar to that recorded in the well-studied Devils Hole phreatic carbonate $\delta^{18}O$ record from the Mojave Desert in southwestern North America. From 75 to 55ka, carbonate $\delta^{18}O$ values sharply increase by ~2‰, a change also recorded by speleothems from central North America, but not seen in the Devil's Hole record. Atmospheric circulation during this time appears to have changed from a state dominated by westerly winds to one influenced by meridional flow from the south along the western limb of a strong and west-based North Atlantic Subtropical High, a condition that increased the proportion of summer to winter precipitation by 20-33%. $\delta^{13}C$ and $^{234}U/^{238}U_i$ values from 75 to 55ka also indicate a shift towards wetter conditions and are supported by regional fossil pollen records suggesting a change to prairie-like ecosystems with wetter summers during this time. Subsequently, the carbonate record suggests that climate in mid-latitude central North America became progressively more arid during the onset of the last glaciation (both $\delta^{13}C$ and $^{234}U/^{238}U_i$ values become more positive), culminating in peak aridity during the Last Glacial Maximum. Carbonate formation rates during these colder conditions increased and the temporal resolution of the Wind River record increased as a result, allowing it to capture sub-millenial abrupt climate changes associated with Dansgaard-Oeschger cycles 6 through 3, Heinrich Stadials 2 through 0 (Younger Dryas), as well as the dramatic Bolling-Allerod warming at 14.5ka. The Wind River pedogenic carbonate record shows the potential to develop similar high temporal resolution paleoclimate records form soil carbonate deposits that are relatively common worldwide.

The Cenozoic paleoclimate of the Atacama Desert is not well known. Chapter 3 presents the results of a study of 14 Oligocene to early Miocene paleosols exposed in the El Tesoro Mine, near Calama, Chile. The paleosols developed on an aggrading alluvial fan system, and lie above mineralized gravels that host a copper ore body. Soil forming conditions that oscillated between chemical weathering and clay production (humid: analogous to modern Alfisols) to environments favoring the accumulation of pedogenic carbonate (arid to semi-arid: analogous to modern Aridisols) are indicated. In contrast, the region is presently hyperarid, and soils accumulate sulfate, chlorides, and nitrates. While total chemical analyses clearly reveal the accumulation of Ca by the carbonate rich paleosols, none of the soils revealed significant losses of elements by leaching. The $\delta^{18}O$ values of the carbonates range from -13.81‰ to -3.16‰ (VPDB). The O isotope data, when combined with published data from the region, revealed a significant divergence in the O isotope composition of precipitation in the eastern and western margins of the Andean plateau since the Oligocene, suggesting that simple interpretations of declines in $\delta^{18}O$ values of carbonate with increasing elevation may not be appropriate. These paleosols clearly indicate that wetter conditions prevailed in what is now the Atacama Desert during the Oligocene to early Miocene.

Chapter 4 presents findings from a study examining a special case of interactions between soil water oxygen isotopes and cations adsorbed to clay minerals in the soil matrix. In isotope-enabled hydrology, soil and vadose zone sediments have been generally considered to be

isotopically inert with respect to the water they host. This is inconsistent with knowledge that clay particles possessing an electronegative surface charge and resulting cation exchange capacity (CEC) interact with a wide range of solutes which, in the absence of clays, have been shown to exhibit $\delta^{18}O$ isotope effects that vary in relation to the ionic strength of the solutions. To investigate the isotope effects caused by high CEC clays in mineral-water systems, we created a series of monominerallic-water mixtures at gravimetric water contents ranging from 5 to 32%, consisting of pure deionized water of known isotopic composition with homoionic (Mg, Ca, Na, K) montmorillonite. Similar mixtures were also created with quartz to determine the isotope effect of non-, or very minimally-, charged mineral surfaces. The $\delta^{18}O$ value of the water in these monominerallic soil analogs was then measured by isotope ratio mass spectrometry (IRMS) after direct headspace CO_2 equilibration. Mg- and Ca-exchanged homoionic montmorillonite depleted measured $\delta^{18}O$ values up to 1.55‰ relative to pure water at 5% water content, declining to 0.49‰ depletion at 30% water content. K-montmorillonite enriched measured $\delta^{18}O$ values up to 0.86‰ at 5% water content, declining to 0.11‰ enrichment at 30% water. Na-montmorillonite produces no measureable isotope effect. The isotope effects observed in these experiments may be present in natural, high-clay soils and sediments. These findings have relevance to the interpretation of results of direct CO_2-water equilibration approaches to the measurement of the $\delta^{18}O$ value of soil water. The adsorbed cation isotope effect may bear consideration in studies of pedogenic carbonate, plant-soil water use and soil-atmosphere interaction. Finally, the observed isotope effects may prove useful as molecular scale probes of the nature of mineral-water interactions.

This dissertation is dedicated to the memory of my grandmother

Margaret Adena Hudson
"Maama"

and her son

Ronald Kent Hudson

Table of Contents

Acknowledgements

A heartfelt thanks goes to Ronald Amundson, my primary advisor and guiding professor during this PhD work. Ron is tireless in all things he does and he always supported and encouraged me to work on things that I was interested in. Todd Dawson's class Stable Isotope Ecology changed my life by broadening my thinking about Earth's Critical Zone and the ways that ecology and earth science are connected. David Shuster provided candor and scientific encouragement and advice at all phases of this work. George Brimhall was my Master's degree advisor and served on my qualifying exam committee, and his penetrating scientific insight and good humor have always been a benefit to me. Many people at Berkeley helped me to prepare samples, perform analytical tasks and to analyze the results, these people deserve thanks and include: Tim Teague, Paul Brooks, Wenbo Yang, Heather Dang and Stefania Mambelli. My teaching mentors include John Battles, Garrison Sposito and Bob Hass who all personify the best qualities of the teachers I worked with at Berkeley and stand as examples of how I hope to teach in the future. My graduate student colleagues also deserve thanks for their good company along the way: Kari Finstad, Marco Pfeiffer, Sarah Reed, and Luiz Mesquita. Good friends outside of school made life more fun and interesting and include: Chris Belnap, Karrie Weaver and Carmen Goodell.

My family has always been there to support me through all of the phases of my life and I am so grateful for: my grandmother Margaret "Maama" Hudson, my mother Ann and her husband Robert, my dad John and his wife Lucia, my sister Lara and her husband Brian, my brother Joel and his fiancé Ashley, and the newer addition of my wife's parents Jim and Jan. Gravy the Pug has been my constant companion and sidekick and always lowers my blood pressure.

The most significant thanks and appreciation go to Megan. She has been a constant source of love and strength for me, and her ability to see past my numerous shortcomings is simply amazing. She is also a scientific role model for me, and is probably the smartest person I know. She is a prime example of how lucky and fortunate I am.

Introduction

This dissertation consists of four chapters reporting research organized around the theme of how the isotopic compositions of C, O and U in soils are related to climate and soil conditions. The research projects are somewhat organized by the timescales of the pedogenic and climatic processes that influence both the isotope composition of various phases in the soil but also the record of those conditions in pedogenic carbonate mineral. Soil carbonate commonly forms in arid and semi-arid soils worldwide, and occurs in a range of forms from small bits disseminated in the fine soil matrix, to dense accumulations on stones in soils, to extreme accumulations of massive calcrete.

Chapter 1 presents and discusses the results of a field study conducted in Fish Lake Valley, Nevada where I established a network of four sites ranging in elevation, and therefore climate. Pedogenic carbonate has formed in these soils and in order to examine the seasonal timing of carbonate formation and the conditions occurring during these times we dug soil pits to sample the soils and installed a variety of instruments to measure various aspects of the climate and soil environment. We examined very young soils in this study on purpose to constrain the age of the pedogenic carbonate to the youngest possible, in this case approximately 3,800 years, and therefore tie its composition to modern conditions in so far as is possible. The evidence that emerges from the soils of Fish Lake Valley is that the timing of soil carbonate formation during the year is difficult to determine and sometimes inconclusive. This is in contrast to recent studies that indicate a discrete and reliable time of carbonate formation can be determined. The implications of my study are that short-term monitoring of soil conditions is useful in understanding the variability in soil conditions through the year. This chapter is being prepared for publication as:

> Oerter, E., Amundson, R., Seasonal C and O isotope dynamics of soil CO_2, H_2O, and carbonate in the western Great Basin, *in preparation for submission to Geoderma.*

Chapter 2 presents a continuous record of paleoclimate in mid-continent North America for the last 120,000 years based on micro-analyses of laminated pedogenic carbonate coatings on soil clasts. The fluvial terraces in the Wind River Basin, Wyoming have soils on their surfaces that have formed dense accumulations of carbonate coatings on gravels and cobbles. When these stones and their carbonate rinds are cut in half with a rocksaw and polished, it is evident that the carbonate coatings have formed in concentric bands much like the annual growth rings in a tree, except that these laminations form over timescales of several hundred years. Modern micro-analytical techniques allow the carbonate layers to be dated and to be analyzed for stable O and C isotopes, which as we have seen in Chapter 1, are related to the climatic conditions in which they formed. The resulting dataset and paleoclimate record is the first of its kind, with a continuity and detail that rivals currently existing paleoclimate records and adds to our understanding of North America climate history during the most recent ice ages. The picture that emerges suggests dynamic climates that may have differed from other parts of North America in ways that were previously unknown. This chapter is being prepared for publication as:

Oerter, E., Sharp, W., Oster, J., Ebeling, A., Valley, J., Kita, N., Ludwig, K., Hellstrom, J., Woodhead, J., Hergt, J., Chadwick, O., Amundson, R., Climate variability in North America during the last 120,000 years revealed by pedogenic carbonate, *in preparation for submission to Science.*

Chapter 3 goes further back in time to examine and discuss soils that formed from 25 to 15 million years ago in South America. We interpret these paleosols to have formed in climates that oscillated from rainy and humid to dry and desert-like, in a region that today is the driest environment on Earth. The Atacama Desert of northern Chile and southern Peru is a fascinating place, partly because of the fact that it has never rained in some places, and partly because we do not have a good sense of how long ago in Earth's history this very stable, precipitation free climate became established. The paleosols exposed in the El Tesoro copper mine indicate that during the Oligocene and Miocene epochs, the climate was much more dynamic and there were periods of time when there was enough rain to prevent the formation of pedogenic carbonate and instead to facilitate the formation of clay minerals. These wet conditions alternated with dry times that did lead to the formation of carbonate and a record of climate and atmospheric circulation that we are familiar with from Chapters 1 and 2. The stable O isotopes in the carbonate reveal a fascinating change that appears to be associated with the rise of the Andes Mountains. As the Andes attained sufficient height through tectonic activity, they began to disrupt atmospheric circulation over the South American continent and this signal is recorded in the carbonate. This chapter is being prepared for publication as:

Oerter. E., Amundson, R., Heimsath, A., Jungers, M. Chong, G., Renne, P., Oligocene to Early Miocene Climatic Oscillations in the Atacama Desert of Northern Chile, *in preparation for submission to Palaeogeography, Palaeoclimatalogy, Palaeoecology.*

Chapter 4 presents findings from a study examining a special case of interactions between soil water oxygen isotopes and cations adsorbed to clay minerals in the soil matrix. In isotope-enabled approaches to hydrology, the soil matrix is typically assumed to be inert with respect to the water oxygen isotopes in the system. We show that Mg, and Ca ions adsorbed to clay minerals exert an effect on the water molecules nearby that tends to concentrate the H_2O molecules with an ^{18}O atom around each metal ion, while K ions tend to attract ^{16}O. This effectively sequesters them from the rest of the water, thereby changing the isotopic composition of that water. Our report is the first observation and quantification of this effect and raises the notion that this effect may be present in natural soils that have high Cation Exchange Capacity, high clay contents and high cation concentrations. This effect may be a mechanism to explain unusual soil water isotope behavior observed in many instances. This chapter grew out of a project for the class Stable Isotope Ecology at UC-Berkeley, and was published as:

Oerter, E., Finstad, K., Schaefer, J., Goldsmith, G. R., Dawson, T., and Amundson, R., 2014, Oxygen isotope fractionation effects in soil water via interaction with cations (Mg, Ca, K, Na) adsorbed to phyllosilicate clay minerals: Journal of Hydrology, v. 515, p. 1-9.

The four lines of research described in this dissertation have the common thread of isotopes running through each of them, but they also have many other unifying aspects. These many commonalities are inevitable because soils and their associated pedogenic processes are so

diverse and numerous in character that similarities and contrasts are inevitable. Each aspect of a soil contains so much potential information about its formation and history that a rich story may emerge, and with some investigation, becoming compelling. I hope I have conveyed some of the fascinating climatic evidence in the soils discussed here beyond just the isotope systems I discuss in detail.

Chapter 1:
Seasonal C and O isotope dynamics of soil CO_2, H_2O, and carbonate in the western Great Basin

1. Introduction

The development of soil is driven by environmental conditions (Jenny, 1941), and soil properties are reflective of those conditions. Pedogenic carbonate is common in modern soils in arid and semi-arid climates worldwide, and when preserved in the geological record its stable C and O isotopic composition is frequently utilized as a record of paleoenvironmental conditions. Several decades ago, the theoretical framework for using the stable C isotope composition of carbonate as a climate proxy was discovered (Cerling, 1984), greatly increasing the utility of soils in paleoclimate research. However, there remain questions about the specific nature of the information that carbonates isotopically reflect, particularly whether they record specific seasonal information or long term annual averages.

When pedogenic carbonate (typically low-Mg calcite, $CaCO_3$) precipitates in soil, its C isotopic composition ($\delta^{13}C$) is controlled by the $\delta^{13}C$ value of soil CO_2 (Cerling, 1984), which is related to vegetation metabolic pathways (Cerling et al., 1991) and biological respiration rates (Raich and Schlessinger, 1992). O isotopes in soil carbonate ($\delta^{18}O$) are a function of the temperature of mineral formation and the $\delta^{18}O$ value of soil water, which is received from precipitation, itself a complex product of climate and atmospheric circulation patterns (Dansgaard, 1964; Gat, 1996).

Pedogenic carbonate precipitates when the soil solution becomes supersaturated due to evaporation, a decrease in soil *p*CO2, or soil temperature increases (Breecker et al., 2009). These conditions may be occur during various times of the year and vary across soil sites in close proximity to each other, especially in intermontane environments where local climates are influenced dramatically by steep elevation gradients. For example, pedogenic carbonate has been interpreted to form in the hot and dry conditions of late spring (Breecker et al., 2009), summer (Amundson et al, 1989), after dry-down from seasonal precipitation inputs (Peters et al., 2013), and even in winter (Quade et al., 1989), depending on the location and study.

In order to better understand the timing of pedogenic carbonate forming conditions in the western Great Basin, we established a climosequence of four study sites. At these sites we measured climate and soil conditions over the course of a year. Here, we report and evaluate these data. It appears carbonate forming conditions vary spatially and temporally, suggesting complexities in interpreting the precise meaning of the C and O isotope values in soil carbonate.

2. Study Location and Methods

2.1 Study Location

The soils studied are in the Trail Canyon area of Fish Lake Valley, Nevada, located on the northeastern flank of the White Mountains (Figure 1). Chiatovich and Rock Creek(s) have formed an easily accessible flight of alluvial fans and inset terraces with associated soils. A climosequence of four study sites was established at various elevations from 1482 to 2602m (Table 1). The ages of the soils at the lower three sites ("A, B and C") are estimated to be 3.8ka, based on radiocarbon dates on charcoal found in soils in the area and geomorphic correlations (Harden et al., 1991, Reheis and Block, 2007). The age of the highest elevation site ("D") is less well constrained, but is likely <10ka based on its position adjacent to the Rock Creek modern

floodplain. These soils reflect soil forming conditions since the mid-Holocene and should have integrated properties similar to modern conditions.

2.2 Field Soil Description and Sampling Methods

Soil pits were excavated to at least 1m. Soil profile descriptions and sampling followed typical pedological procedures (Soil Survey Staff, 1999; Schoeneberger et al., 2012). Bulk samples were taken from each soil horizon, and samples of carbonate-bearing <2 mm fines (and clasts with carbonate rinds) were collected every 10 cm where present.

Samples for soil water $\delta^{18}O$ isotope analyses were taken in duplicate as ~5g samples into 12mL glass vials with screw top septum caps for direct equilibration with CO_2, and 2) as ~25g samples into 30mL borosilicate glass vials with polyseal caps for vacuum distillation (as discussed below). Samples collected for soil water $\delta^{18}O$ analyses were collected immediately from excavated surfaces to avoid evaporative isotope enrichment.

Dielectric resistivity-based volumetric soil water content (g H_20 g^{-1} soil) and temperature sensors (Decagon Instruments, model EC-TM) were installed in the soil pit walls at 10cm, 25cm, 50cm, and 100cm depths and connected to data loggers (Decagon Instruments, model EM-50) located in lidded vaults, buried to a depth allowing several cm of soil cover. Each soil pit was carefully backfilled and tamped in approximately 25cm levels to emulate the native soil bulk density. Air temperature and relative humidity sensors (Decagon Instruments, model VP-3) were installed on posts 50cm above the ground surface adjacent to each soil installation. Readings from all sensors were taken every 30 minutes and recorded in non-volatile Flash memory in the data loggers.

Vegetation surveys were made using four 50 m transects randomly chosen by azimuth direction. Plant samples adjacent to the soil gas wells and soil water sensors were collected by clipping stem material adjacent to the main stem. These samples were immediately placed into polyseal-capped glass vials and wrapped with Parafilm, for subsequent vacuum extraction of water for O isotope analysis.

Precipitation was collected in non-evaporating collectors consisting of a 10 cm funnel draining into a Nalgene bottle, both of which were attached to a lightweight steel post. A small plastic ball in the funnel was used to block the funnel throat, and a ~1cm layer of silicon oil was added to the collection bottle in order to completely cover the collected water surface. Collected precipitation amounts were normalized to the funnel opening area. A duplicate precipitation collector was installed at Site C.

In order to conduct repeated, non-destructive sampling of soil water for O isotopes, the O isotope composition of soil CO_2 was used as a probe of soil water (Stern et al., 1998; Breecker and Sharp, 2008). Soil gas wells were constructed from 6.35 mm OD, 2mm wall, stainless steel tubing with a 30mm long 11.1mm solid stainless steel rod welded to one end and sharpened to form a drive point. Approximately 20, 2mm diameter holes spaced every ~5mm were drilled into the bottom end of the tubing immediately above the drive point to create a ~2cm perforated interval. The wells were driven to depths of 10cm, 25cm and 50cm (38cm at Site D) at each site, and to 100cm at Site A and to 78cm at Site B. At sites C and D the high gravel and clast content of the soil did not allow for direct drive placement of soil gas wells to deeper depths. At these sites, a channel was cut into the soil pit wall to a depth of approximately 70cm, and the gas well was driven 3 cm into the channel floor, thereby achieving a 100cm depth. Soil gas wells were sealed with replaceable rubber septa caps. At Site A, two additional sets of soil gas wells were installed to assess intra-site variability.

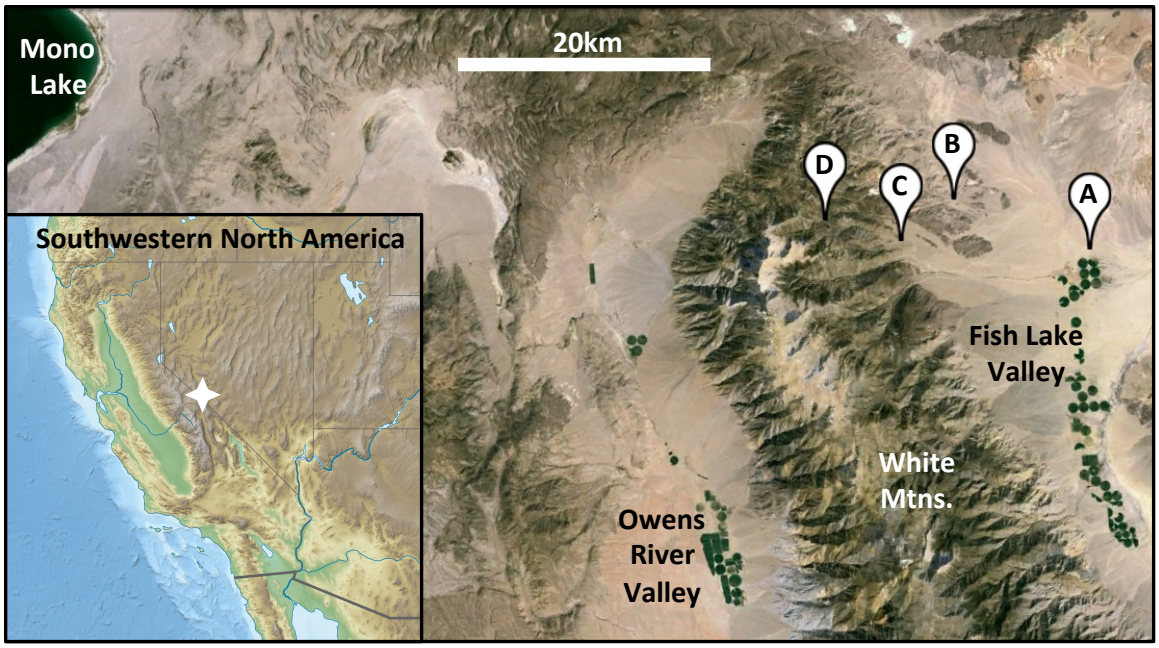

Figure 1. Inset: Map of Southwestern North America with Fish Lake Valley denoted by white star. Main Map: Fish Lake Valley region with study sites A-D denoted.

Table 1. Geographic, climatic, precipitation $\delta^{18}O$ values, soil and vegetation properties of study sites.

	Site A "Saltbush"	Site B "Blackbrush"	Site C "Sagebrush"	Site D "Pinon"
Latitude	37° 50' 19.68"	37° 52' 52.43"	37° 51' 19.33"	37° 52' 16.64"
Longitude	-118° 4' 32.70"	-118° 10' 49.58"	-118° 13' 48.50"	-118° 17' 46.97"
Elevation (m)	1482	1745	2140	2602
MAAT (°C)[1]	12.2	12.8	10.0	7.0
MAP (mm/yr)[2]	78	134	178	214
$\delta^{18}O$ precip summer[3]	-4.51	-6.63	-7.92	-8.08
$\delta^{18}O$ precip winter[4]	-14.25	-15.23	-15.48	-15.36
$\delta^{18}O$ weighted ave	-12.37	-11.49	-11.70	-12.80
Soil Classification	Typic Haplocalcid	Typic Haplocalcid	Typic Haplocalcid	Ustic Haplocalcid
Soil Texture	Sandy	Sandy Loam	Sandy Loam	Loamy Sand
C3/C4[5]	0.01	0.94	0.99	0.99
Vegetation species	*Atriplex spinifera 70%* *Atriplex confertifoli 25%* *Atriplex cenescens 4%* *Coleogyne sp. 1%*	*Coleogyne sp. 76%* *Grayia spinosa. 16%* *Cylindropuntia sp. 4%* *Atriplex confertifoli 2%* *Ephedra nevadensis 2%*	*Artemisia tridentata 46%* *Grayia spinosa 19%* *Ericameria cooperi 19%* *Chrysothamnus nauseosus 8%* *Ephedra nevadensis 4%* *Artemisia spinescens 4%* *Peucephyllum schotti 4%* *Bunch grasses undet. (rare)*	*Artemisia tridentata 46%* *Purshia mexicana 31%* *Fraxinus anomala 14%* *Pinus monophylla 9%* *Bunch grasses undet. (rare)*

[1] Average air temp. during the period: 18 May 2013 - 18 May 2014
[2] Average precip. collected during the monitroring period (380 days) and normalized to 365 days
[3] Summer precip collected 26 August 2013
[4] Winter precip collected 30 Nov 2013, 19 April 2014, 31 May 2014
[5] CAM-type included with C4 group

Sample vials of 12mL volume were first acid washed with dilute HCl, and oven dried. The vials were then purged with dry N_2 for 10 sec at >1 L/min flow rate before closing with a dry septum screw cap. Soil gas was sampled from each well with a 60mL syringe attached to a 1.6cm diameter x 5cm long cartridge filled with 10-20 mesh sized Drierite^{TM} desiccant ($CaSO_4$), and a 10cm long x 22ga deflected point septum-piercing needle. The desiccant is necessary to prevent the condensation of water vapor in the vials and subsequent isotope exchange (Gemery, et al., 1996). Because the desiccant cartridge must have the pre-existing atmosphere purged, 36mL of soil air was withdrawn from each well allowing a purging of both the well bore (0.43 to 4.3mL interior volume) and desiccant cartridge with soil air. The collected soil air inside the syringe was expelled into the atmosphere. Another 36mL of soil gas was withdrawn from the well and slowly injected into the sample vial while the pre-existing N_2 was expelled through a 1cm 22ga vent needle inserted into the septum. Both needles were quickly removed following sample transfer. Atmospheric air samples were also taken by the same method from a few centimeters above the land surface.

Replicate samples were collected for $\delta^{13}C$ and $\delta^{18}O$ analyses, as well as for *p*CO2. In total, 180mL of soil air (5 withdrawals of 36 mL: 1 purge, 4 samples) were removed from soils during each sampling. Assuming a porosity of 50%, this represents a sphere of influence of 3.5cm radius around each well's perforated interval.

During each sampling (dates listed in Table 1) the following data or samples were collected: soil moisture and temperature, air temperature and humidity, accumulated precipitation, plant stem samples, soil gas samples, atmospheric air samples, surface water samples from Rock Creek nearby Site D and an intermittent ground water spring nearby Site B. Seasons discussed in this paper are defined as, spring: March, April, May; summer: June, July, August; fall: September, October, November; winter: December, January, February.

2.3 Laboratory and analytical methods

Bulk samples were passed through a 2mm sieve. Munsell soil color value determinations were made on the dry <2mm fine fraction. Particle size determinations were made with the hydrometer method (Gee and Bauder, 1986). Presence of carbonate in the <2mm fine fraction was determined by reaction with dilute HCl. Small (~5g) sub-samples of carbonate-bearing fine material were passed thru a 0.5mm sieve to remove coarse sand, ground by hand in deionized water with a mortar and pestle and dried overnight at 60°C. Gravels and clasts with carbonate coatings were scraped to remove carbonate with a stainless steel dental pick. Carbonate material from several clasts in each horizon was combined and lightly ground by hand with a mortar and pestle and dried overnight at 60°C. Carbonate $\delta^{13}C$ and $\delta^{18}O$ isotope analyses were performed on a dual inlet GV Isoprime gas source isotope ratio mass spectrometer with MultiCarb sample introduction interface at the Laboratory for Environmental and Sedimentary Isotope Geochemistry at UC-Berkeley.

Soil water $\delta^{18}O$ values were determined by two methods, each in replication. In the first approach, soil water was distilled with heat in a vacuum line and cryogenically collected for 240 minutes to ensure complete volumetric water recovery. The second approach utilized soil collected directly into 12mL autosampler-specific vials in the field, and brought back to the laboratory. Sample vial headspace was purged with 0.2% CO_2 in He and allowed to equilibrate directly with water in the soil matrix in the vial at room temperature for 5 days (Hsieh et al., 1998; Ferretti et al., 2003) and subsequently analyzed as described below.

Plant xylem water was distilled and collected in a vacuum line in a manner similar to that of soil water. The extracted soil and plant waters, as well as the precipitation water and surface water samples, were subsampled in 50µL aliquots and equilibrated in 12mL glass vials with 0.2% CO_2 in He at room temperature for 5 days (Epstein and Mayeda 1953). These and the direct-equilibration samples were analyzed for $\delta^{18}O$ values on a Thermo Delta V Isotope Ratio Mass Spectrometer (IRMS) instrument in continuous flow mode with Thermo Gas Bench II interface and CTC Analytics Combi-PAL autosampler at the Center for Stable Isotope Biogeochemistry, UC Berkeley. Long-term external precision on this instrument is ±0.12‰ for $\delta^{18}O$ of water.

Isotopic analyses for $\delta^{13}C$ and $\delta^{18}O$ values on soil and atmospheric air were conducted on the same IRMS instrument as water but with reference standards of CO_2 in air (-8.795‰ $\delta^{13}C_{VPDB}$, 35.537 $\delta^{18}O_{VSMOW}$, $[CO_2]$=373 ppm) included every 6th sample during analyses to monitor and correct for instrumental drift. Analyses were begun with six of these reference standards to condition the ion source and establish stable instrument performance. $\delta^{13}C$ and $\delta^{18}O$ values on soil and atmospheric air reported are the average of measurements on two replicate samples.

Isotope δ values are defined as:

$$\delta = (R_{sample} / R_{standard} - 1) \times 1000$$

where R_{sample} and $R_{standard}$ are the $^{13}C/^{12}C$ or $^{18}O/^{16}O$ ratios for the sample and standard, respectively. $\delta^{13}C$ and $\delta^{18}O$ values on carbonate are reported in per mille (‰) referenced to the Vienna Pee Dee Belemnite (VPDB) standard and all $\delta^{18}O$ values of equilibrated CO_2 or H_2O are reported in in per mille (‰) referenced to Vienna Standard Mean Ocean Water (VSMOW).

Soil water $\delta^{18}O$ values were calculated from soil CO_2 $\delta^{18}O$ values using the oxygen isotope fraction between CO_2 and H_2O (Brenninkmeijer et al., 1983; Breecker and Sharp, 2008) calculated from the average soil temperatures measured at each soil gas well depth for the 24 hour interval prior to soil gas collection.

Comparison of $\delta^{18}O$ values of xylem water to soil water never exactly matched at any depth, but had $\delta^{18}O$ values intermediate between two soil depths. Therefore, the fraction of soil water used by each species from differing soil depths was determined using a 2-component linear mixing model (Phillips and Greg, 2001):

$$fraction_{upper} = (\delta_{xylem} - \delta_{lower}) / (\delta_{upper} - \delta_{lower})$$

$$fraction_{lower} = 1 - fraction_{upper}$$

where "xylem" is the plant water $\delta^{18}O$ value, "upper" is the $\delta^{18}O$ value of soil water most similar to xylem water above the inferred zone of soil water uptake, and "lower" is the $\delta^{18}O$ value of the soil water below. The estimated depth of soil water uptake was then calculated as a depth-weighted average using the relative contributions of water from each depth:

$$depth\ of\ soil\ water\ uptake = ((depth_{upper})(fraction_{upper})) + ((depth_{lower})(fraction_{lower}))$$

Soil water sensors (Decagon Instruments, model EC-TM) were calibrated using soil material collected from Site B and that was dried overnight at 105°C. Approximately 2kg of

dried soil was weighed, and 4 volumetric water sensors were inserted into the soil. Repeat measurements were taken once a minute for 10 minutes. Water was added incrementally to the soil, reweighed and mixed to a uniform wetness, and the measurements were repeated from 3.4% to 32.3% volumetric water content. The resulting calibration is:

VWC = (SensorOutputRawCounts-524.84)/1166.7

Samples of soil air, atmospheric air, and QA/QC air were analyzed on a Shimadzu GC-14A gas chromatograph with a thermal conductivity detector for determination of pCO_2 concentrations.

3. Results

3.1 Climate, vegetation, and soil properties vs elevation

Average values of air temperature and precipitation for each site are shown in Table 1. Average air temperature decreased with increasing elevation at a rate of -5.1°C km^{-1}, and precipitation increased by 121mm km^{-1}. The seasonal distribution of precipitation is shown in Figs. 2A-2D. Spring season precipitation dominated the lowest and highest elevation sites (A and D), while the mid-elevations received more summer precipitation (Sites B and C). Winter precipitation $\delta^{18}O$ values ranged from -14.25‰ (VSMOW) at 1482m to -15.36‰ at 2602m, and summer precipitation $\delta^{18}O$ values were -4.51‰ (VSMOW) at 1482m and -8.08‰ at 2602m (Tables 1 and 3). The isotopic lapse rates are -0.99‰ km^{-1} and -3.19‰ km^{-1} for winter and summer respectively.

Vegetation survey data are reported in Table 1. Biomes vary with elevation with Saltbush scrubland at 1482m elevation (Site A), Blackbrush shrubland at 1745m (Site B), Sagebrush shrubland at 2140m (Site C), and Piñon-Sage woodland at 2602m (Site D). These biomes are similar to those found elsewhere in the White Mountains area (Hall, 1991) and throughout the Great Basin of North America (Grayson, 2011).

Soil properties are listed in Tables 1 and 2. All of the soils are Haplocalcids, but the highest elevation bordered on an Ustic rather than Aridic moisture regime. Dry soil colors are yellow-red (10YR), but became darker (lower value) with increasing site elevation. Site A is developed in sandy granitic and rhyolitic parent material sourced from the White Mountains to the west, as well as eolian sand and dust. This soil has an incipient natric horizon (high Na and associated clay dispersion and redistribution) from 5-20cm depth. The mid-elevation soils at Site B and C are formed on rhyolite and andesite gravels from higher in the Rock Creek watershed and nearby intrusive rocks. Soil at the highest elevation (Site D) formed in coarse alluvium and colluvium gravels sourced from the Boundary Peak quartz monzonite upslope of the site, as well as from the adjacent Mustang Mountain metasedimentary slate.

Soil texture changed from sandy at Site A, to sandy loam at the mid-elevations, to loamy sand at the highest elevation. Soil horizon development, such as clay content and soil structure, generally increased with elevation and precipitation.

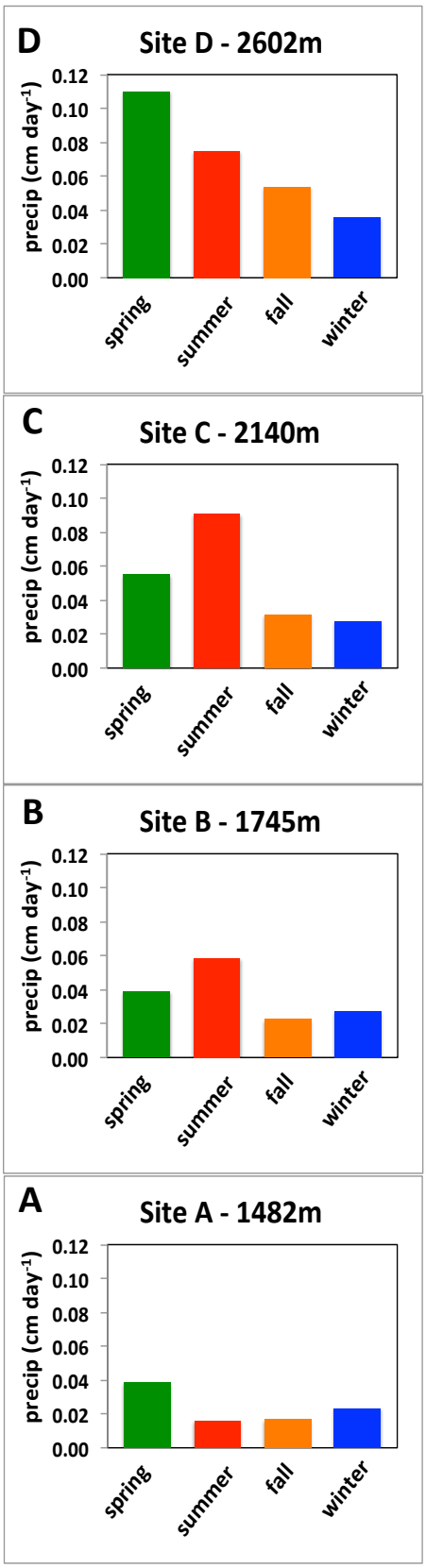

Figure 2. Seasonal precipitation rates.

Table 2. Soil properties of study sites.

Site	Horizon	Depth (cm)	Color (H V/C)	Clay (%)	Rocks (%)	Structure	Roots
A	A1	0 - 5	10 YR 7/3	2	10%	1mpl (sfc)	1vf
"Saltbush"	Btnk	5 - 20	10 YR 7/3	4	5%	1cco	1vf
	Bk1	20 - 40	10 YR 7/3	9	20%	loose	2vf, 2f
	Bk2	40 - 66	10 YR 7/4	4	30%	loose	2vf, 1f, 1m
	Bk3	66 - 100	10 YR 7/3	2	40%	loose	1vf, 1f, 1m
B	A1	0 - 4	10 YR 6/2	5	30%	1cpl	1vf, 1f, 1m
"Blackbrush"	A2	4 - 14	10 YR 5/3	5	20%	loose	1vf, 1f
	Bk1	14 - 34	10 YR 5/3	5	30%	1csbk	2vf, 1f, 1m
	Bk2	34 - 45	10 YR 6/3	5	30%	1csbk	2vf, 1f, 1m
	Bk3	45 - 100	10 YR 6/3	6	80%	1msbk	1vf - 2f
C	A1	0 - 5	10 YR 6/2	3	10%	loose	1vf
"Sage"	A2	5 - 20	10 YR 6/2	6	10%	1csbk	2vf, 1f, 1m
	Bk1	20 - 48	10 YR 6/3	6	30%	1csbk	2vf, 1f, 1m, 1c
	Bk2	48 - 74	10 YR 6/3	5	30%	1csbk	1vf, 1f, 1m
	Bk3	74 - 100	10 YR 6/3	6	60%	1csbk	2vf, 1f, 1m
D	A1	0 - 6	10 YR 6/3	8	30%	2cpl	2f
"Pinon"	A2	6 - 18	10 YR 6/4	10	40%	1msbk	2vf, 1f
	AB	18 - 28	10 YR 6/4	12	40%	1fsbk	1vf, 1f
	Bw	28 - 42	10 YR 5/3	10	60%	1fsbk	2vf, 1f, 1m
	Bk1	42 - 78	10 YR 6/3	5	80%	massive	2vf, 2f, 1m, 1c
	Bk2	78 - 100	10 YR 4/3	10	40%	massive	1f, 1m

Table 3. $\delta^{18}O$ values (VSMOW) of precipitation and surface water samples.

Sampling Date	Site A Saltbush	Site B Blackbrush	Site C Sage	Site D Pinon	Rock Creek	Camp Spring
18 May 2013	NA	NA	-10.99	-14.75	-16.08	-15.07
26 Aug 2013	-4.51	-6.63	-7.92	-8.08	-16.27	Dry
30 Nov 2013	-14.44	-15.75	-16.12	-15.23	-16.43	-15.50
19 Apr 2014	-14.60	-14.61	-15.28	-15.48	-16.35	-15.20
31 May 2014	-13.7	-15.32	-15.04	-14.95	-16.21	Dry
Ave. summer $\delta^{18}O$[1]	-4.51	-6.63	-7.92	-8.08	-	-
Ave. winter $\delta^{18}O$[2]	-14.25	-15.23	-15.48	-15.1	-	-

[1] Summer precip collected 26 August 2013

[2] Winter precip collected 30 Nov 2013, 19 April 2014, 31 May 2014

Pedogenic carbonate in the soils of Site A, B and C was disseminated in the fine soil matrix (<2mm grain size) and also occurred as coatings on soil clasts. Site D only had carbonate coatings on clasts. The carbonate coatings were thin (≤1mm thick) (Stage I of Gile et al., 1966) and were located on clast bottoms. The depth to pedogenic carbonate increased with increasing elevation and increasing MAP. The relationship between MAP and depth to carbonate (MAP (mm yr^{-1}) = 3.47(Depth in cm)+80.8 (R^2=0.87 on 4 data points)) is similar to that previously observed in arid and semi-arid soils of California and Nevada (Arkley, 1963), but more shallow, at a given MAP, than common to soils in the mid-continent (Jenny and Leonard, 1934; Royer, 1999).

3.2 Seasonal soil volumetric water dynamics

Soil volumetric water contents at each site are shown in Figs. 3A-3D. Sites A and D received more precipitation during the spring (Figs. 2A and 2B), and soil moisture there increased or was invariant from 100 to 50cm depth (Figs. 3A and 3D). These soils were drier at 25cm depth compared to 50cm throughout the year, with the exception of spring at Site A. In the winter and spring (and fall at Site D), these soils were moist at 10cm, while summer was the driest time of the year at 10cm depth. In contrast, at Sites B and C which were more strongly impacted by summer- precipitation, soil moisture was low at 50cm depth at all times of the year (Figs. 3B and 3C). Both of these soils were moister at 25cm than 50cm during, except during the summer at Site B. These soils were drier at 10cm compared to 25cm, except during the winter (Figs. 3B and 3C).

3.3 Carbonate C and O stable isotopes

Soil carbonate depth profiles of $\delta^{13}C$ and $\delta^{18}O$ values are shown in Figs. 4A and 4B, and reported in Table 5. At sites with both fine, disseminated carbonate (<2mm) and coatings on clasts, isotope values are similar and depth profiles have similar trends (Figs. 4A and 4B). The correspondence in $\delta^{13}C$ and $\delta^{18}O$ values between carbonate fines and coatings suggests that isotopic conditions have not changed significantly over the course of soil formation, since the two forms have different residence times. Additionally, it shows that all fine grained carbonate, even if originally derived from eolian inputs, has undergone isotopic exchange due to weathering. Previous work in Fish Lake Valley near Site B by Pendall et al. (1994), suggested the time required for this resetting of $\delta^{13}C$ and $\delta^{18}O$ values to be between 1 and 3.8ka. In the following discussion, we focus specifically on the carbonate on clasts as all soils contain this form of the mineral.

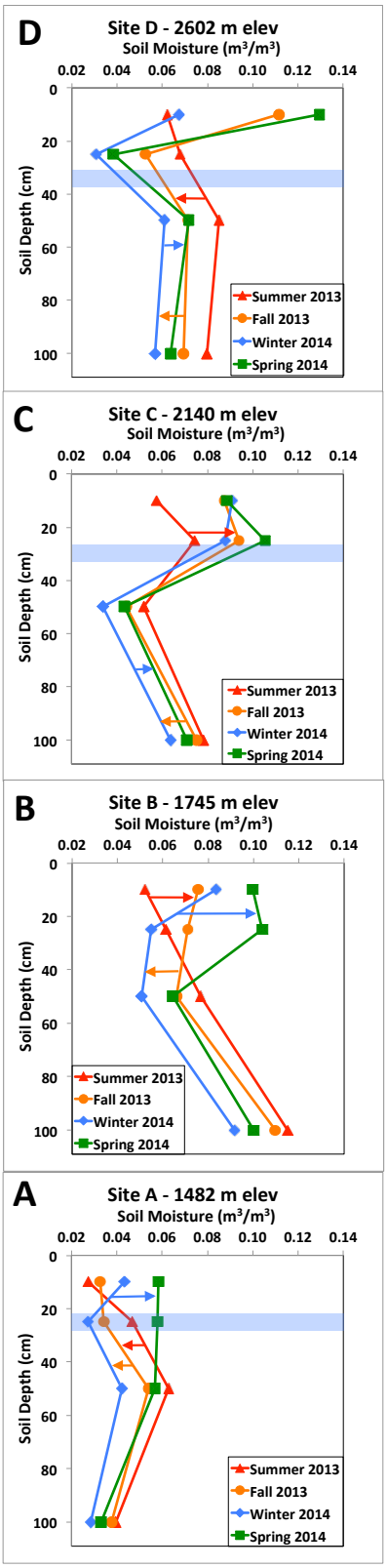

Figure 3. Seasonal soil moisture profiles, blue bands indicate average depth zones of plant water uptake determined by O isotope composition of plant xylem water (*Artemisia* only at Site D). Arrows denote seasonal evolution of depth profiles.

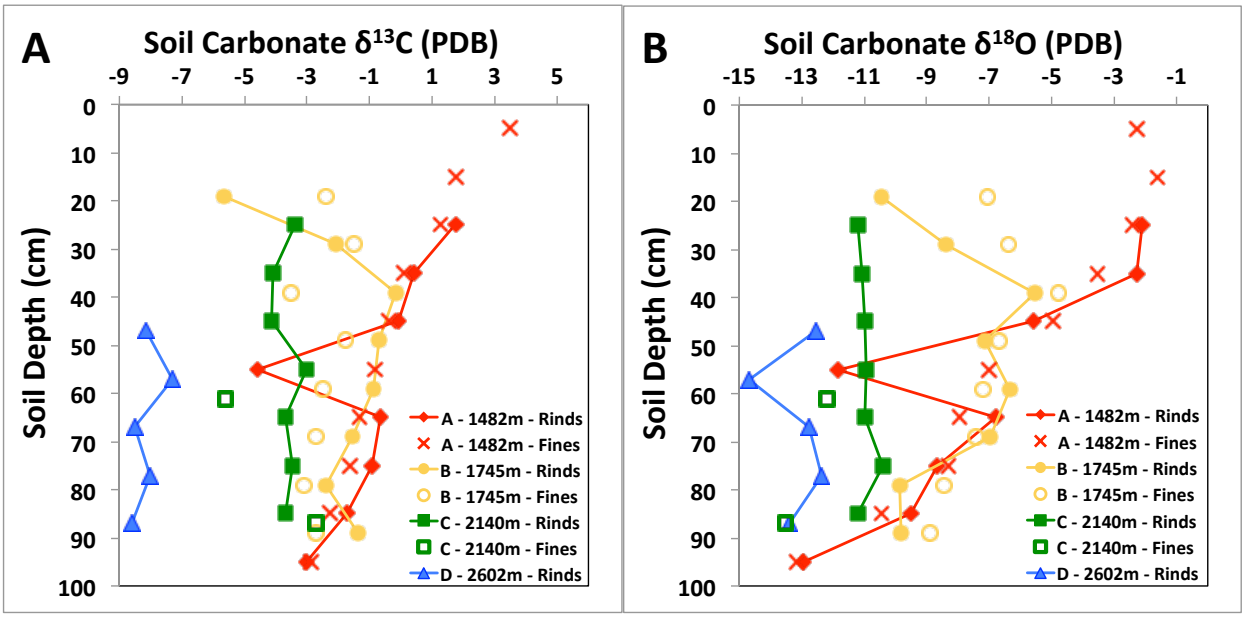

Figure 4. (A) Soil carbonate $\delta^{13}C$ depth profiles; and (B): soil carbonate $\delta^{18}O$ depth profiles.

Table 5. Carbonate $\delta^{13}C$ and $\delta^{18}O$ values for soils.

Fines (<2 mm)				Clast Rinds			
Sample	**Depth (cm)**	**$\delta^{13}C$ (‰ VPDB)**	**$\delta^{18}O$ (‰ VPDB)**	**Sample**	**Depth (cm)**	**$\delta^{13}C$ (‰ VPDB)**	**$\delta^{13}O$ (‰ VPDB)**
A-0-10-F	5	3.48	-2.29				
A-10-20-F	15	1.75	-1.61				
A-20-30-F	25	1.29	-2.41	A-20-30-R	25	1.75	-2.08
A-30-40-F	35	0.11	-3.51	A-30-40-R	35	0.41	-2.26
A-40-50-F	45	-0.37	-4.97	A-40-50-R	45	-0.09	-5.58
A-50-60-F	55	-0.83	-7.02	A-50-60-R	55	-4.57	-11.85
A-60-70-F	65	-1.34	-7.93	A-60-70-R	65	-0.64	-6.79
A-70-80-F	75	-1.62	-8.30	A-70-80-R	75	-0.91	-8.64
A-80-90-F	85	-2.24	-10.46	A-80-90-R	85	-1.74	-9.52
A-90-100-F	95	-2.90	-13.17	A-90-100-R	95	-3.01	-12.94
B-14-24-F	19	-2.41	-7.07	B-14-24-R	19	-5.67	-10.46
B-24-34-F	29	-1.52	-6.37	B-24-34-R	29	-2.09	-8.37
B-34-44-F	39	-3.49	-4.77	B-34-44-R	39	-0.17	-5.54
B-44-54-F	49	-1.74	-6.71	B-44-54-R	49	-0.68	-7.13
B-54-64-F	59	-2.47	-7.20	B-54-64-R	59	-0.86	-6.34
B-64-74-F	69	-2.69	-7.39	B-64-74-R	69	-1.53	-6.98
B-74-84-F	79	-3.10	-8.43	B-74-84-R	79	-2.40	-9.88
B-84-94-F	89	-2.72	-8.89	B-84-94-R-1	89	-1.35	-9.81
C-48-74-F	61	-5.61	-12.20	C-20-30-R	25	-3.36	-11.19
C-74-100-F	87	-2.71	-13.53	C-30-40-R	35	-4.07	-11.05
				C-40-50-R	45	-4.14	-10.98
				C-50-60-R	55	-3.00	-10.94
				C-60-70-R	65	-3.69	-10.98
				C-70-80-R	75	-3.46	-10.40
				C-80-90-R	85	-3.70	-11.22
				D-42-52-R	47	-8.13	-12.53
				D-52-62-R	57	-7.28	-14.69
				D-62-72-R	67	-8.49	-12.75
				D-72-82-R	77	-8.01	-12.36
				D-82-92-R	87	-8.61	-13.41

3.4 Soil CO_2-H_2O oxygen isotope equilibrium

The utilization of soil CO_2 $\delta^{18}O$ values as a method to repeatedly and non-destructively measure soil H_2O $\delta^{18}O$ values is based on the assumption of O isotope equilibrium between soil CO_2 and soil H_2O (Stern et al., 1999; Amundson et al, 1998; Breecker and Sharp, 2008). In order to validate this assumption and calibrate the relationship between $\delta^{18}O$ values of soil CO_2 and soil H_2O, we compare soil water $\delta^{18}O$ values measured by several methods as follows. When the soil water $\delta^{18}O$ values from vacuum distilled soil water are compared to $\delta^{18}O$ values calculated from soil CO_2 (Fig. 5A), the soil CO_2 values tend to plot about 1.5‰ above the 1:1 line, with a slope of 0.93. When the $\delta^{18}O$ values of soil water measured by direct equilibration in-vial are compared to soil water $\delta^{18}O$ values from vacuum distilled soil water (Fig. 5B), the in-vial equilibrated $\delta^{18}O$ values also plot above the 1:1 line.

However, a comparison between $\delta^{18}O$ values from in-soil direct equilibration and in-vial direct equilibration has a 1:1 correlation (Fig. 5C). This suggests that the discrepancy between in-soil or in-vial equilibration and vacuum distilled soil water $\delta^{18}O$ values may be due to something specific to the direct equilibration of CO_2 with in-situ water in the soil matrix. Work by Stern et al. (1999) suggests that the $\delta^{18}O$ value of soil CO_2 undergoing O isotope exchange with soil H_2O will be about 1‰ higher than that predicted by equilibrium between pure CO_2 and H_2O. This difference is due to the rate constant of the isotope exchange reaction being slower in soil than that of pure CO_2 and H_2O, which results in diffusional enrichment ^{18}O in the CO_2. Therefore, because the soil CO_2 derived water values produced a constant 1.47‰ offset towards heavier soil water $\delta^{18}O$ values in the observed range of -12 to 9‰ (VSMOW), we subtract a 1.5‰ correction factor from the soil water $\delta^{18}O$ values calculated from in-soil CO_2-equilibrated $\delta^{18}O$ measurements. Although vacuum distillation of soil water is prone to a variety of errors induced during the process (e.g. Araguas-Araguas et al., 1995), and the depth profiles of vacuum distilled soil water in this study does show variability at some depths that is not reflected in the other approaches, especially at Site A (Fig. 6A), the general shape of the depth profiles of all soil water measurement approaches is similar (Figs. 6A-6D).

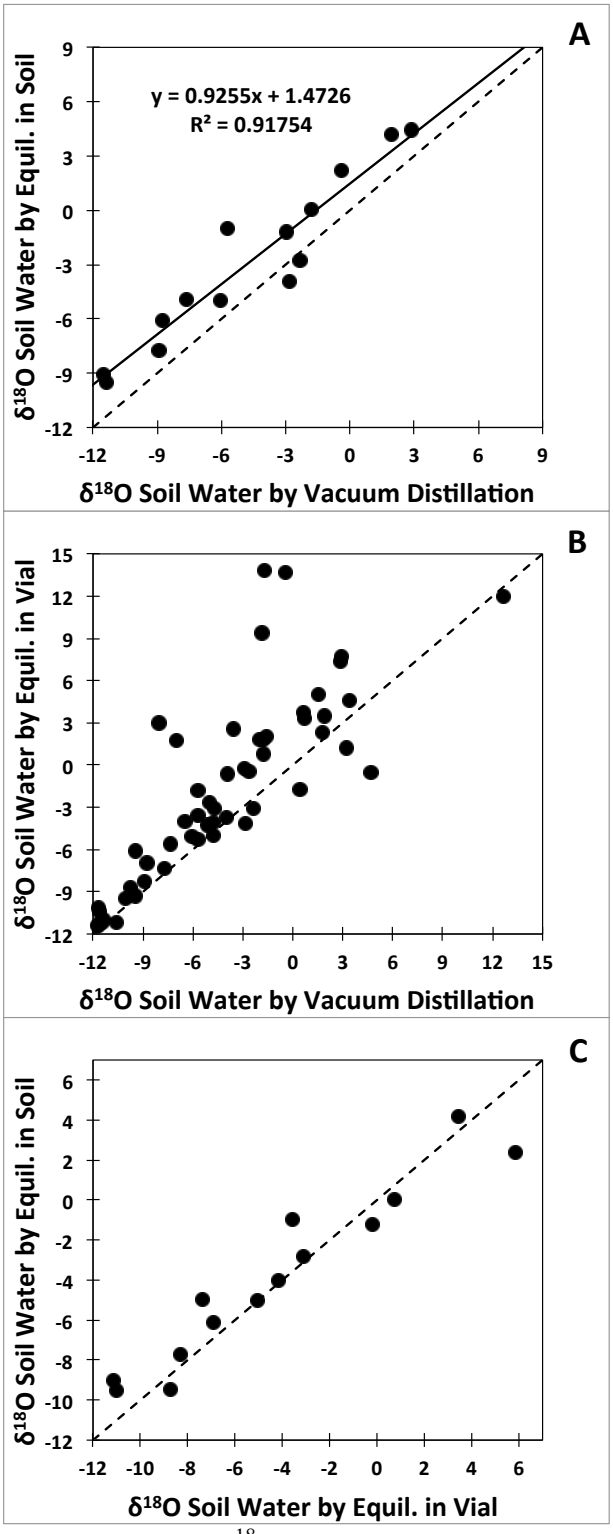

Figure 5. (A) Comparison of soil water $\delta^{18}O$ values by direct equilibration in-soil vs. $\delta^{18}O$ values of vacuum distilled soil water, (B) comparison of soil water $\delta^{18}O$ values by direct equilibration in-vial with $\delta^{18}O$ values of vacuum distilled soil water, (C) comparison of $\delta^{18}O$ values by direct equilibration in-soil with $\delta^{18}O$ values by direct equilibration in-vial. Dashed lines are 1:1 lines.

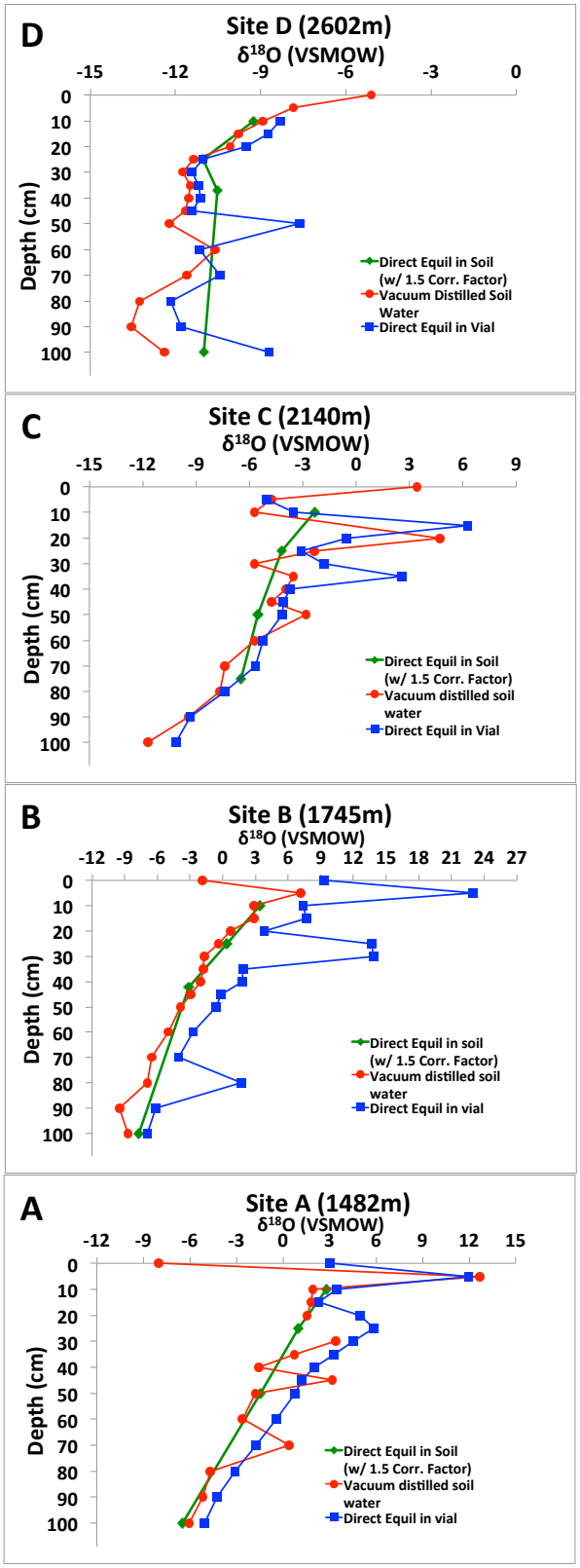

Figure 6. Comparison of $\delta^{18}O$ values of soil water by in-soil equilibration (with 1.5‰ correction applied, see text in Section 4.4) (green), vacuum distillation (red), and in-vial equilibration (uncorrected) (blue).

3.5 Seasonal soil pCO_2 dynamics

Soil pCO_2 concentrations vs depth are shown in Figs. 7A-7D, and reported in Supp. Table 1. Soil pCO_2 levels at all the study sites were lowest during the fall, reflecting dry soil and cold temperatures that inhibit soil biological activity (Figs. 3A-3D). At Site D, the prolonged cold soil temperatures and soil pCO_2 levels remained low throughout the winter. In contrast, winter soil pCO_2 levels at Sites A-C fell within the mid values of the annual range in concentrations, even though soil moisture levels were very low (Figs. 3A-3D). Spring season soil pCO_2 levels were the highest of the year at Site A. Summer season soil pCO_2 levels were the highest of the year at Sites B-D.

3.6 Soil CO_2 seasonal C isotope dynamics along the transect

Soil CO_2 $\delta^{13}C$ values become increasingly negative with increasing soil depth and elevation (Figure 8 and Supp. Table 1). At Site A, soil CO_2 $\delta^{13}C$ values were most negative during the fall through spring seasons, while summer had the most positive $\delta^{13}C$ values (Fig. 8A). In contrast, at Site B summer and winter soil CO_2 $\delta^{13}C$ values are most negative (Fig. 8B), while fall is the time of more positive soil CO_2 $\delta^{13}C$ values. This pattern of the most negative soil CO_2 $\delta^{13}C$ values during the summer and most positive during the fall is also observed at Sites C and D (Figs. 8C and 8D).

3.7 Soil H_2O seasonal O isotope dynamics

Soil water $\delta^{18}O$ values at the sites along the transect generally decrease with increasing elevation (Figure 9A and Supp Table 1). At Site A, soil H_2O $\delta^{18}O$ values are generally highest at shallow depths and decrease with increasing depth. During the fall and winter season at depths less than 50cm, soil H_2O $\delta^{18}O$ values decrease relative to the summer values. During the winter, these low $\delta^{18}O$ values are preserved at 25cm depth, while $\delta^{18}O$ values at 10cm become more positive (Fig. 9A). At Site B, soil H_2O $\delta^{18}O$ values were relatively invariant throughout the year, with a minor change in the shallow soil towards more positive values during the spring (Fig. 9B). At Site C, soil H_2O $\delta^{18}O$ values were lowest during the fall season and increased through the spring at all depths, before returning to more negative $\delta^{18}O$ values during the summer (Fig. 9C). Site D H_2O $\delta^{18}O$ values were nearly invariant from the fall through the spring, with slight increases in the upper 10cm during springtime (Fig. 9D). Summer season soil H_2O $\delta^{18}O$ values were the highest of the year at Site D in the upper 50cm of the soil, and were similar to the yearly values at 100cm depth. A feature common to all of the soils is a shift in $\delta^{18}O$ towards heavier values of 2-3‰ at shallow (10cm) depths.

3.8 Seasonal plant water uptake dynamics

The apparent depths of soil water uptake by plants at each site are shown in Fig. 3 and in Table 4. At Site A, *Atriplex spinifera* withdrew water from ca. 12-20 cm throughout the year, except during May 2014 when xylem water was most similar to soil water from 55cm. At Site B, the extracted xylem water from *Coleogyne ramosissima* was always more enriched in $\delta^{18}O$ (higher values) than the soil water at any depth. The reasons for this pattern are not apparent, but would seem to suggest that the plant water reflected enrichment by transpiration, possibly through the stem tissue. At Site C, *Grayia spinosa* withdrew water from ca. 22 to 48cm depth except for the summer, where depths of ca. 18cm were closest to plant values. At Site D, *Artemisia tridentata* withdrew water from ca. 28 to 47cm depth, while *Pinus monophylla* had more negative $\delta^{18}O$ values than any measured soil water, indicative of deep water extraction.

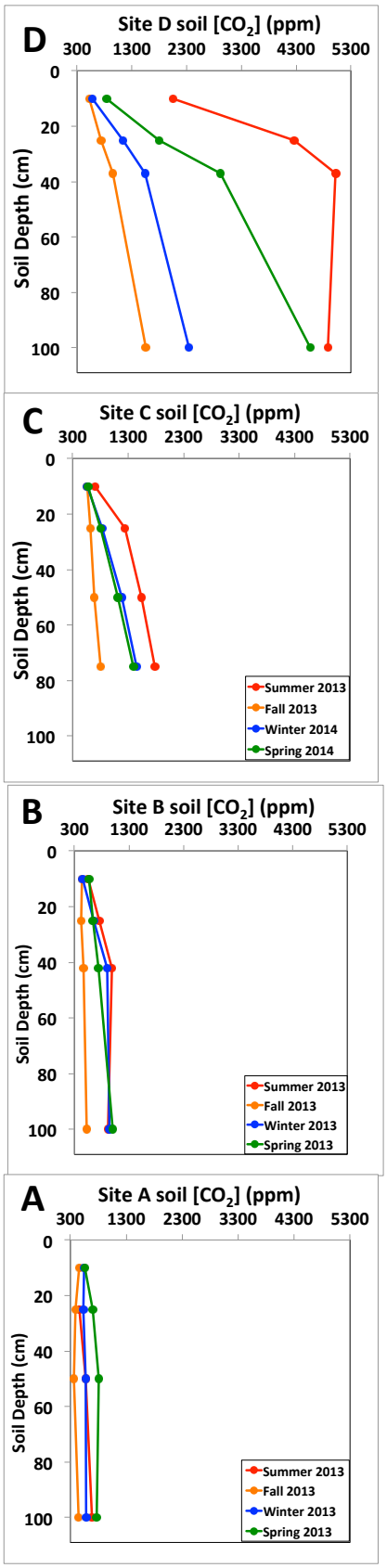

Figure 7. Soil *p*CO2 depth profiles.

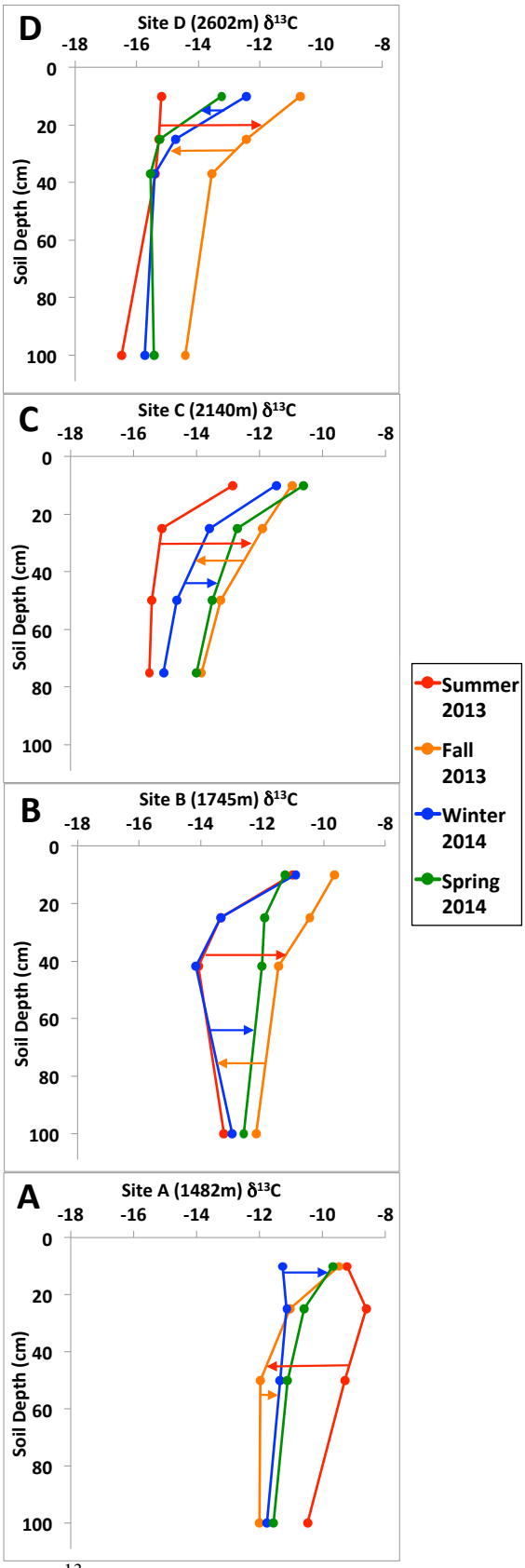

Figure 8. Measured soil CO_2 $\delta^{13}C$ values. Arrows denote seasonal evolution of profiles.

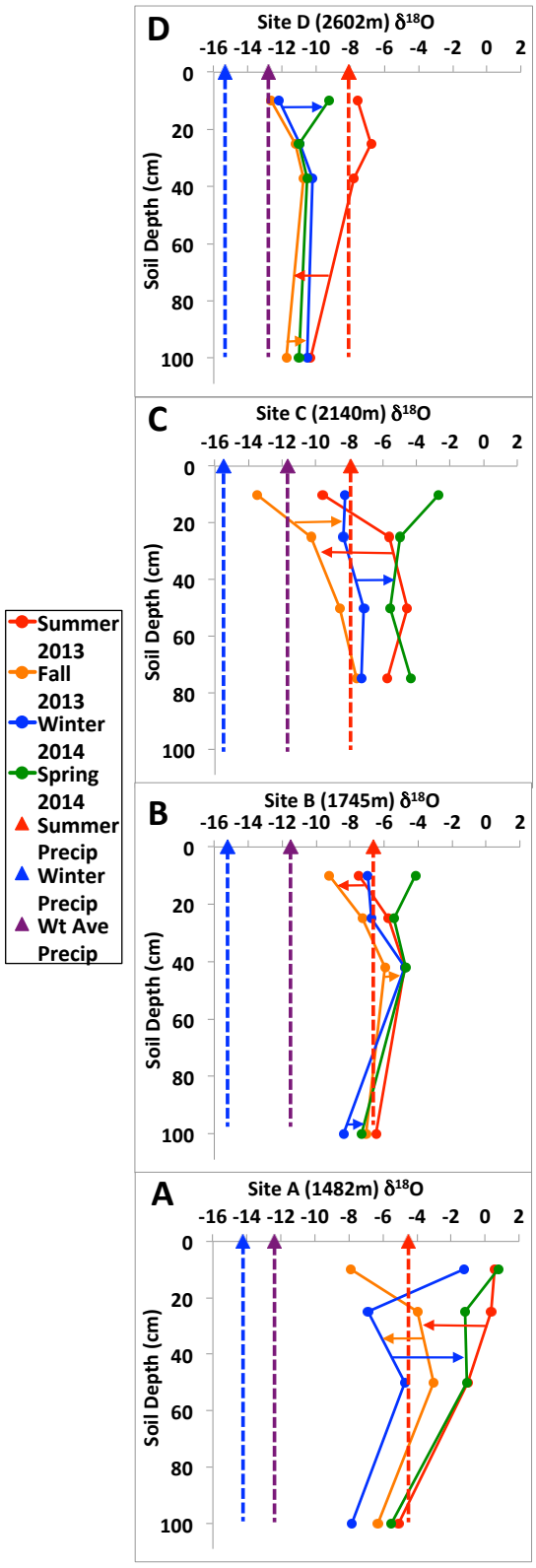

Figure 9. Soil H_2O $\delta^{18}O$ values measured by in-soil equilibration with soil CO_2, and corrected by subtracting 1.5‰ for direct equilibration effects (see text Section 4.4). Arrows denote seasonal evolution of depth profiles.

Table 4. Plant water uptake depths base on comparison of $\delta^{18}O$ values of xylem water to soil water.

Sampling Date:	18 May 2013		26 Aug 2013		30 Nov 2013		19 Apr 2014		31 May 2014			
	xylem		xylem		xylem		xylem		xylem			
site (species sampled)	H_2O $\delta^{18}O$ ‰	source depth (cm)	H_2O $\delta^{18}O$ ‰	source depth (cm)	H_2O $\delta^{18}O$ ‰	source depth (cm)	H_2O $\delta^{18}O$ ‰	source depth (cm)	H_2O $\delta^{18}O$ ‰	source depth (cm)	average depth (cm)	average depth (sd)
A *(Atriplex spinifera)*	2.53	12.4	-8.88	?	-5.09	20.8	-3.84	16.9	-1.46	54.5	26.2	19.2
B *(Coleogyne ramosissima)*	-7.75	>100	-2.81	?	0.85	?	-1.92	?	-5.48	46.3	?	?
C *(Grayia spinosa)*	-4.29	26.8	-7.60	17.5	-8.73	47.9	-5.94	?	-4.59	22.6	28.7	13.4
D *(Artemisia tridentata)*	-10.60	46.7	-7.06	28.2	-10.78	36.1	NA	NA	-8.61	28.5	34.9	8.7
D *(Pinus monophylla)*	-12.78	>100	-9.85	88.6	-10.25	?	-11.36	>100	-10.89	>100	>100	>100

4. Discussion

At Fish Lake Valley in western Nevada, the results indicate that soil H_2O, CO_2 and carbonate $\delta^{13}C$ and $\delta^{18}O$ values change systematically with elevation and climate. While there is inherent difficulty in assigning specific intervals (seasons) of carbonate formation from field measurements taken over the course of only one year, we show how the conditions observed during different seasons generally explain the C and O isotope trends of the soil carbonate. Our results also indicate that in arid environments with distinctly seasonal rainfall, soil carbonate C and O depth profiles can incorporate aspects of differing time intervals and sources, reflecting not one discreet intervals of carbonate formation, but that of multiple seasons.

4.1 Soil H_2O and plant H_2O uptake effects

Two main factors appear to control the shape of soil moisture depth profiles: the relative proportions of seasonal precipitation and the depth of plant water uptake. The zones of apparent soil dewatering by plant water uptake (as determined by the O isotope composition of their tissue water) generally corresponded to the driest intervals in the soils (Fig. 3, Table 4). At Site A, *Atriplex spinifera* appeared to utilize water from shallow soil levels (ca. 12-20cm), which is likely the reason for the minima in the soil moisture depth profiles during the fall and winter. Spring was the wettest time of the year at Site A and *Atriplex* increased its apparent depth of soil water use to ~54cm. *Atriplex confertifoli* is a co-occurring species at Site A and has been shown to attain its highest water use and metabolic rates during spring and before the onset of summer high temperatures (Summers et al., 2011). This may explain the high pCO_2 levels at Site A during the spring, in contrast to the other sites, which exhibit pCO_2 maxima during the summer (Fig. 7).

While soil water uptake analysis at Site B did not yield easily interpretable results, *Coleogyne ramosissima* may have utilized soil water from the 25-50cm depths since these were the minima in soil water content, except during the spring. Previous work has shown that *Coleogyne* is able to utilize summer rainfall efficiently, even when temperatures are the highest

of the year (Gebauer and Ehleringer, 2000; Summers et al., 2011). High xylem water $\delta^{18}O$ values may be a consequence of water utilization during high temperatures as transpiration through the stem tissue and evaporation at its surface may be increased.

At Site C, *Grayia spinosa* utilized soil water from ca. 22 to 48cm depth except for the summer, when depths of ~18cm most closely resembled plant water. *Artemisia* is also a dominant species at Site C and while its water use was not studied at Site C, *Artemisia* withdrew water from 28 to 47cm at Site D (Figs. 3A and 3C, and Table 4). Soil moisture values were at minima year round at 50cm depth, and these low soil water levels were probably related to plant water extraction. Site C had the highest plant diversity of the transect and the variety of rooting depths and metabolic characteristics may help explain the trends in pCO_2 which decline with depth almost monotonically, a pattern that is unique to Site C (Fig. 7).

Site D was unique in that its vegetation was characterized by a woody *Pinus monophylla* forest and *Artemisia tridentata* understory, two plants which appeared to exhibit contrasting water use strategies. *Artemisia* utilized water from 28 to 47cm depth, while *Pinus* appeared to use ^{18}O depleted water not represented in the soil profile we sampled, likely extracted from greater depths. The likeliest source of this water is a shallow alluvial aquifer associated with nearby Rock Creek, which had $\delta^{18}O$ values of -16‰ that were temporally invariant (Table 3). Yearly soil moisture at Site D was lowest at 25cm depth, likely reflecting extraction by *Artemsia*.

4.2 Soil CO_2 C isotopes and their relation to soil carbonate

The isotope composition of soil CO_2 varies seasonally in many environments due to variations in the proportion of biologically respired CO_2 and atmospheric CO_2 (Cerling, 1984; Amundson et al., 1998). At low soil respiration rates (due to either low soil moisture, temperatures, or sparse plant cover), the atmospheric component of soil CO_2 is increased. Thus, soil carbonate, depending on the season in which it forms, may have isotopic values that are indicative of specific seasons and associated conditions.

At any soil respiration rate, the $\delta^{13}C$ values of soil CO_2 (and pedogenic carbonate formed in C isotopic equilibrium with it) can be described with a one-dimensional production/diffusion model (Cerling, 1984). Here, the upper boundary condition in the model is constrained by atmospheric CO_2 $\delta^{13}C$ values measured approximately 5cm above the soil surface, while the lower boundary condition (source CO_2) is estimated to be -14‰ at Site A (reflecting 100% C4 vegetation) and -25‰ at Sites B-D (reflecting C3-dominated vegetation). Modeled respiration rates are fit to the depth profiles of soil CO_2 $\delta^{13}C$ values to constrain soil respiration rates (Fig. 10).

There was a positive relationship between soil moisture availability and soil respiration rates, as noted in other studies (e.g. Raich and Schlessinger, 1992). Yearly precipitation was dominated by spring season rain and snow at the low and high elevation sites (A and D) (Fig. 2), leading to high soil moisture levels and soil respiration rates (Figs. 13A and 13D). The two mid-elevation sites (B and C) were more strongly impacted by summer monsoon rains, which increased soil moisture levels and soil respiration rates (Figs. 13B and 13C). Soil moisture was lowest during the fall season at all of the sites (Fig. 3) and soil respiration rates are correspondingly lower, except at Site A, which displayed high soil respiration during the Fall 2013. It is unclear why this low elevation site maintained high respiration rates despite the apparently limited moisture.

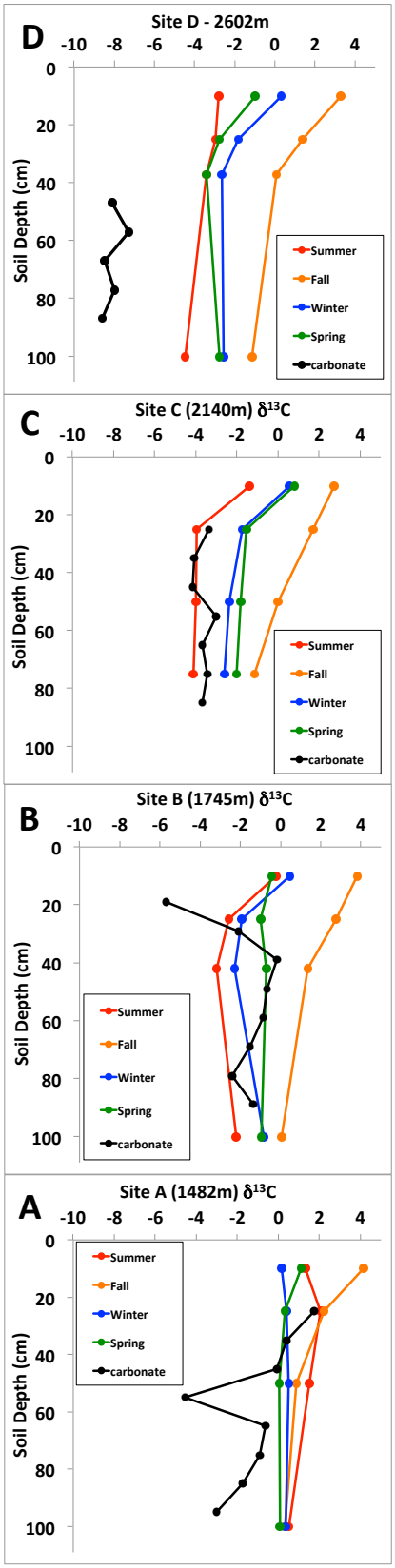

Figure 10. $\delta^{13}C$ values of carbonate in C isotopic equilibrium with soil CO_2 vs. measured carbonate $\delta^{13}C$ values.

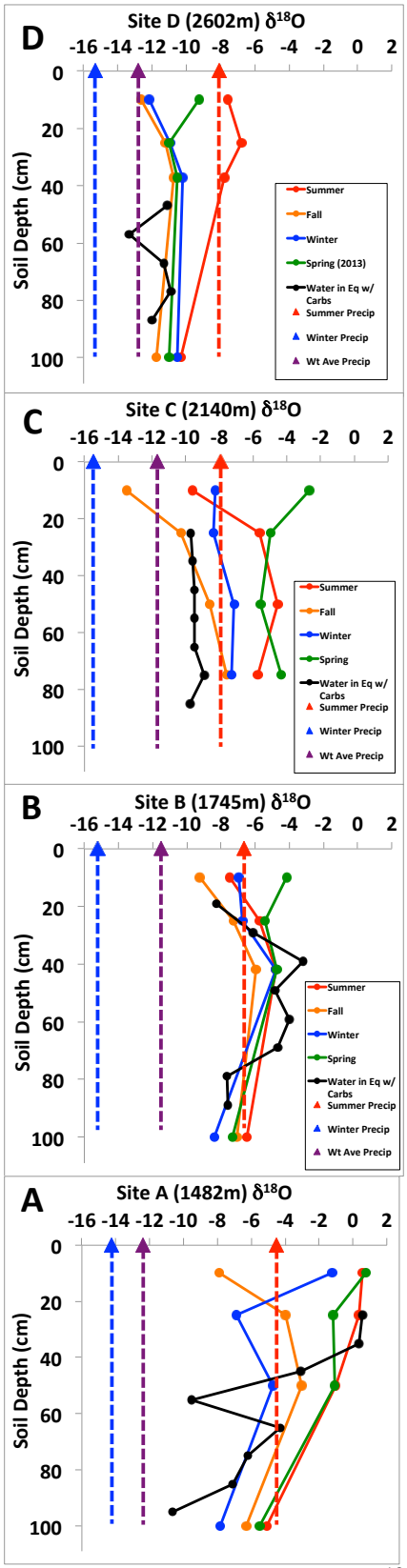

Figure 11. Soil H_2O $\delta^{18}O$ values compared to precipitation $\delta^{18}O$ values and $\delta^{18}O$ values of soil H_2O in O isotopic equilibrium with carbonate.

Soil carbonate forms in isotopic equilibrium with soil CO_2. Thus, the C isotope profiles of carbonate are indicators of the mean soil respiration rates that occurred during carbonate precipitation. Using atmospheric CO_2 $\delta^{13}C$ boundary conditions of -6.5‰ (VPDB) to reflect pre-industrial atmospheric CO_2 (e.g. Francey et al., 1999) and biological CO_2 $\delta^{13}C$ values of -14‰ at Site A and -25‰ at Sites B-D, we fit the production/diffusion model to the soil carbonate $\delta^{13}C$ values to derive mean respiration rates, and compare those to the seasonal trends in CO_2 discussed earlier.

At Site A, $\delta^{13}C$ values of soil carbonate suggest that it formed under soil respiration rates of ~0.2mmol m^{-2} hr^{-1}, similar to soil respiration rates during the spring or perhaps the fall (Fig. 13A). Site B soil carbonate $\delta^{13}C$ values correlate with soil respiration rates of ~0.07mmol m^{-2} hr^{-1}, reflecting measured summer and early spring rates (Fig. 13B). Soil carbonate at Site C reflects soil respiration rates of ~0.185mmol m^{-2} hr^{-1}, similar to measured spring rates (Fig. 13C). Site D soil carbonate formed in the highest soil respiration rates along the gradient, indicative of spring time rates of at ~0.46mmol m^{-2} hr^{-1} (Fig. 13D). Soil respiration rates calculated from soil carbonate increase with MAP (0.0018mmolC m^{-2} hr^{-1}), though at only about half the rate as that measured worldwide (0.0037 mmolC m^{-2} hr^{-1}) (Raich and Schlessinger, 1992). Conversely, soil respiration rates calculated from soil carbonate *decrease* with MAT (-0.0581mmolC m^{-2} hr^{-1}), compared to worldwide rates that increase with MAT (0.243 mmolC m^{-2} hr^{-1}) (Raich and Schlessinger, 1992), a difference that is due to precipitation that increases with decreasing MAT and increasing elevation at Fish Lake Valley, a trend that is opposite that found in the global database, a signal dominated by the warm and wet low latitudes.

A more direct means of linking seasonal CO_2 flux to the soil carbonate is through matching the isotope composition of the carbonate directly to the CO_2 at different times of the year, though this method is weakened by the short term nature of the CO_2 measurements vs. the long term signal embedded in the carbonate. Measured soil CO_2 $\delta^{13}C$ values (corrected for recent fossil fuel influence) were used to calculate $\delta^{13}C$ values of carbonate (Romanek et al.,1992) with the average soil temperatures measured during the 24hr period preceding soil gas sampling ("predicted"). The closeness of fit can be quantified with the following expression (Breecker et al., 2009):

$$\Delta^{13}C_{meas\text{-}predic}\ (‰) = \delta^{13}C_{measured} - \delta^{13}C_{predicted}$$

Figure 12 shows $\Delta^{13}C_{meas\text{-}predic}$ values for measured soil CO_2 $\delta^{13}C$ values at the depths closest to measured soil carbonate $\delta^{13}C$ values at the study sites through the year. The C isotope offsets between the measured CO_2 over the course of one year, and that of carbonate that has accumulated over millennia, is likely an approximate guide to the source and timing of carbonate precipitation. Indeed, there is not a definitive match between measured CO_2 and soil carbonate for the highest elevation site, where carbonate has more negative $\delta^{13}C$ values than any CO_2 collected during the study period, presumably reflecting less productive conditions during 2013-14 than the long-term average. The remaining sites suggest close agreement between carbonate and CO_2 in the spring to late summer, which is reasonable based on work by Breeker et al. (2009). However, these correlations at Fish Lake Valley are largely nonexclusive. The key finding, however, is that it appears that the C isotopes in the soil carbonate do broadly reflect overall C isotope conditions at the sites, with about a 2‰ difference between each elevation, equivalent to a $\delta^{13}C$ lapse rate of -7‰ km^{-1} (Fig. 8).

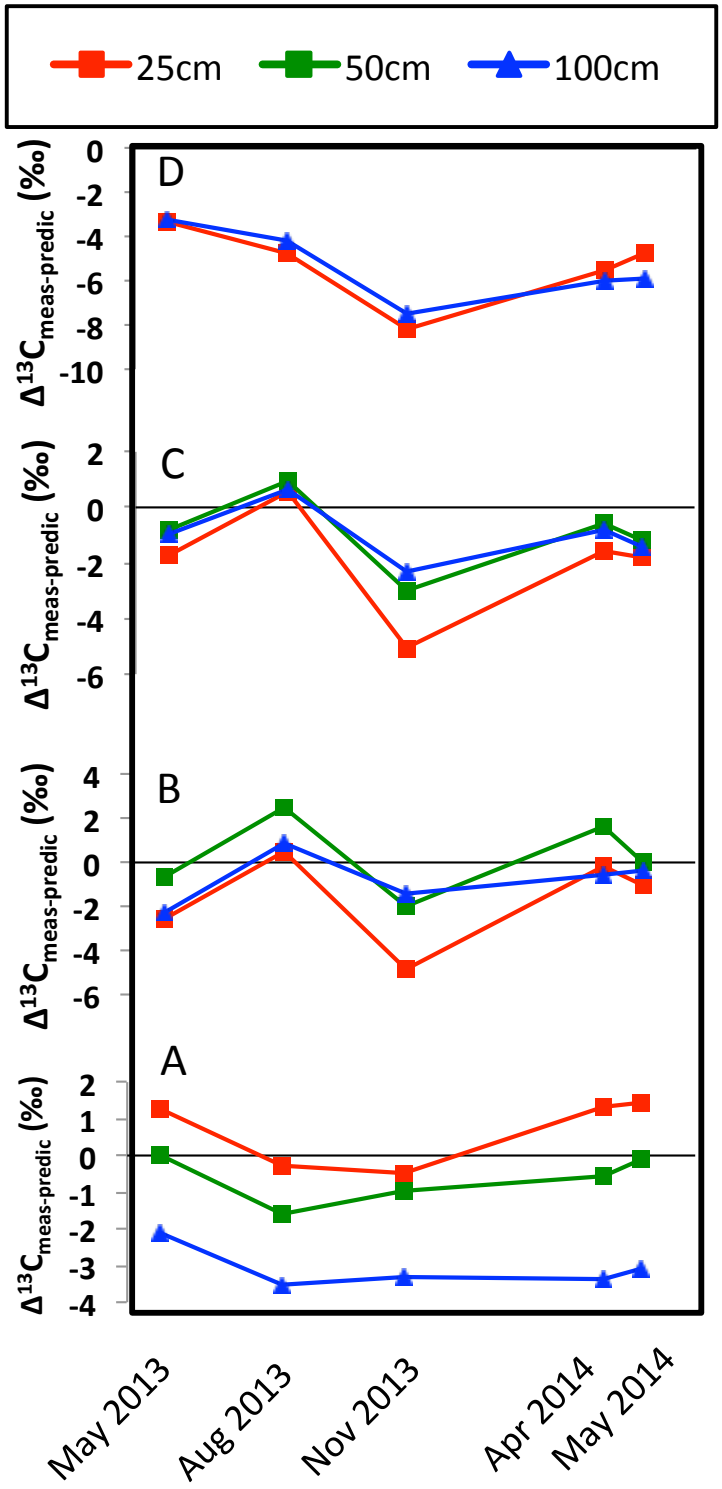

Figure 12. Comparison of measured carbonate $\delta^{13}C$ values at various soil depths compared to $\delta^{13}C$ values calculated to be in C isotope equilibrium with measured soil CO_2 ("predicted").

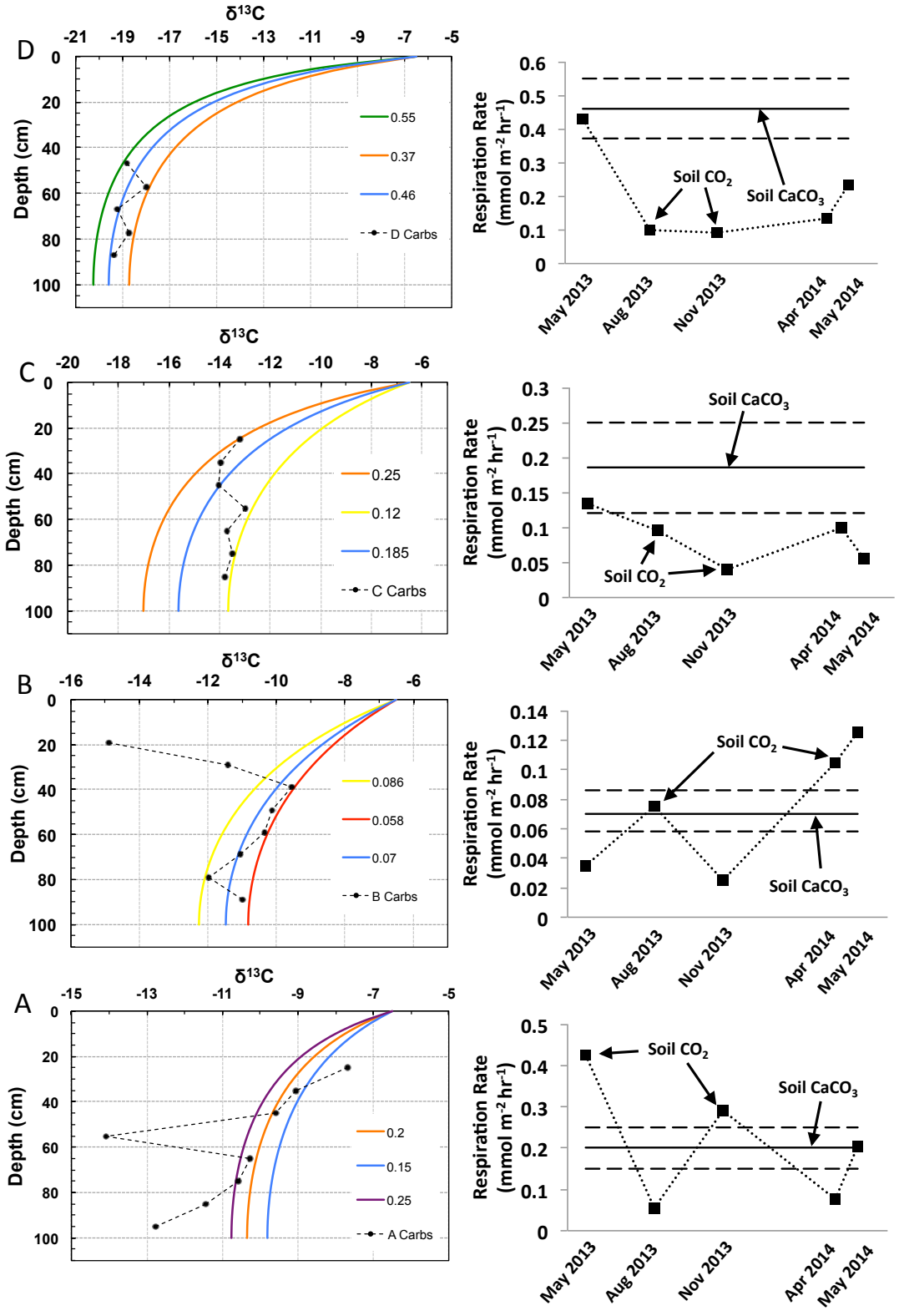

Figure 13. Left: Modeled respiration rates compared to $\delta^{13}C$ values of carbonate; Right: Respiration rates modeled to fit soil CO_2 $\delta^{13}C$ values (solid markers and dotted lines), compared to respiration rates modeled for $\delta^{13}C$ values from carbonate, as shown on left.

4.3 Soil H_2O O isotope dynamics and their relation to soil carbonate

After infiltration, soil water in arid and semi-arid soils is lost through transpiration and evaporation, the later process causing an enrichment of ^{18}O in the remaining soil water. This results in depth trends of soil water $\delta^{18}O$ values that commonly decline non-linearly (Barnes and Allison, 1983). With sufficient depth, the soil water $\delta^{18}O$ values approach that of the average rainfall (Wang et al., 1996). Superimposed on these long-term processes are rainfall events that "reset" the soil water $\delta^{18}O$ profile to reflect that of the precipitation, which were observed most notably at Sites A and C (Figs. 9A and 9B). Subsequent periods of evaporation drive $\delta^{18}O$ to more positive values in the upper soil, which happened in the spring at Sites A-C and at Site D in the summer (Fig. 9).

In general at Fish Lake Valley, the effect of evaporation on soil water, as reflected by the shape of the O isotope profile, declines with increasing elevation (Fig. 9) and increasing plant cover. Deep soil water $\delta^{18}O$ values decrease with increasing elevation along the transect at an isotopic lapse rate of -4.5‰ km^{-1} (Fig. 9). Deep soil water at the mid-elevation Sites B and C have $\delta^{18}O$ values most similar to summer precipitation, which reflects the dominance of summer rainfall at these sites (Figs 2B and 2C). Soil water $\delta^{18}O$ values at Site A appear to trend towards more negative values beyond 1m depth and possibly stabilize somewhere deeper in the soil at a values more similar to winter or yearly weighted average $\delta^{18}O$ values of precipitation (Fig. 9A). Site D deep soil water $\delta^{18}O$ values appeared to be reflect the yearly weighted average of precipitation $\delta^{18}O$ values (Fig. 9D).

Measured soil H_2O $\delta^{18}O$ values were used to calculate $\delta^{18}O$ values of carbonate (Kim and O'Neil, 1997) with the average soil temperatures measured during the 24hr period preceding soil gas sampling. These "predicted" carbonate $\delta^{18}O$ values can be used to guide interpretations of the timing of O isotope equilibrium between soil H_2O and soil carbonate using (Breecker et al., 2009):

$$\Delta^{18}O_{meas\text{-}predic}\ (‰) = \delta^{18}O_{measured} - \delta^{18}O_{predicted}$$

Figure 14 shows $\Delta^{18}O_{meas\text{-}predic}$ values for measured soil H_2O $\delta^{18}O$ values at the depths closest to measured soil carbonate $\delta^{18}O$ values at the study sites through the year. As with carbon, the predicted carbonate oxygen isotope values are based on just one year of soil water sampling (and precipitation). In general, all sites have more negative carbonate $\delta^{18}O$ values than that of the soil water in the 2013 to 2014 interval except for Site B, which attained $\Delta^{18}O_{meas\text{-}predic}$ nearly equal to zero in August of 2013 (Fig. 14B), indicating summertime carbonate formation. The shape of the soil carbonate profile at site B (Fig. 11B) clearly shows that the carbonate forms with differently sourced pools of water with increasing depth: the shallowest carbonate values are quite negative, and reflect soil water between summer and winter O isotope values. The lower depths reflect the downward penetration of some isotopically enriched water from previous seasons.

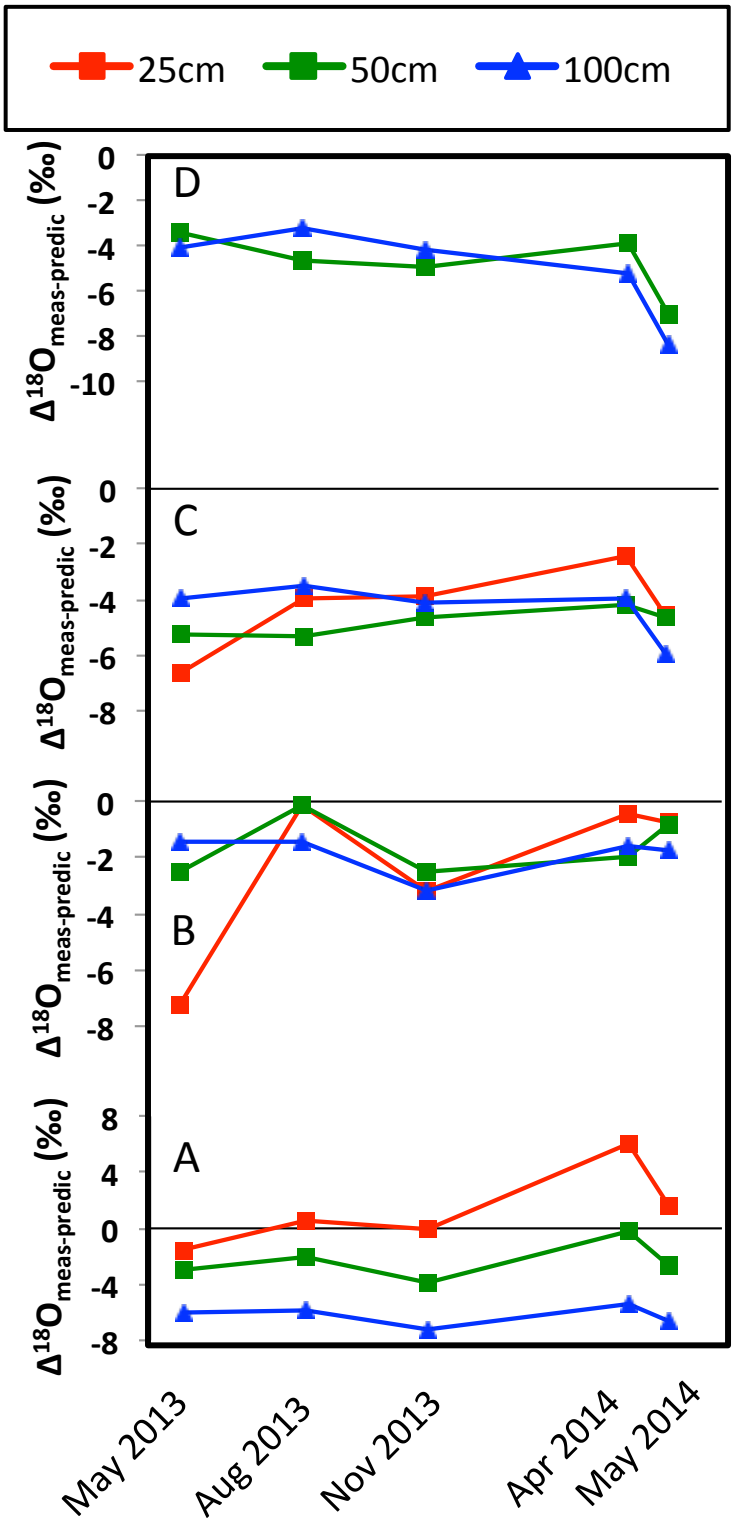

Figure 14. Comparison of carbonate $\delta^{18}O$ values compared to $\delta^{18}O$ values calculated to be in O isotope equilibrium with measured soil H_2O ("predicted").

The unsaturated hydraulic conductivity of the soils can be estimated by examination of the time series volumetric water content data, allowing an estimation of the time for a storm event's water to infiltrate to various depths. The estimated unsaturated hydraulic conductivity for the sandy soil of Site B is about 3.95m yr^{-1}, which is in the range of literature values for saturated hydraulic conductivity in sandy soil (Freeze and Cherry, 1979). This estimate indicates that the time for water to travel from the surface to 40cm depth (the upper depth of the heavier $\delta^{18}O$ values of carbonate) is 37 days, and 65 days to reach 70cm (the lower $\delta^{18}O$ values of carbonate). This suggests that the carbonate at Site B is forming during the summer, but is possibly recording the precipitation received during the late spring (Fig. 11B). While there is considerable uncertainty in this calculation , it is interesting that the timing of carbonate formation may not reflect the precipitation conditions during that same time. A key conclusion from the O isotopes is that at Fish Lake Valley, it appears that the O isotopes in the soil carbonate broadly reflect conditions during the spring and summer at the lower sites, and systematically shift towards a reflection of the year round precipitation at a $\delta^{18}O$ lapse rate of -4.5‰ km^{-1} (Fig. 11).

4.4 Climate conditions reflected in the O and C isotope composition of pedogenic carbonate

The seasonal dynamics of carbon and oxygen stable isotopes in soil CO_2 and soil carbonate reveal different seasonal timings of pedogenic carbonate and therefore a distinct seasonal signal is preserved in the carbonate at each site. At Site A, modeling of soil respiration rates based on $\delta^{13}C$ values of pedogenic carbonate compared to that based on measured soil CO_2 $\delta^{13}C$ values indicates that spring season conditions are reflected in carbonate $\delta^{13}C$ values. On the other hand, the timing of C and O isotope equilibrium between soil CO_2, soil H_2O and soil carbonate are met nearly year-round especially at soil depths of 25-50cm.

At Sites B and C, comparison of modeled soil respiration rates derived from soil carbonate and measured soil CO_2 $\delta^{13}C$ values suggest that spring and summer conditions are reflected in soil carbonate $\delta^{13}C$ values. Comparison of the timing of oxygen isotope equilibrium between soil H_2O and soil carbonate $\delta^{18}O$ values at Site B indicates that spring and summer conditions are recorded in soil carbonate $\delta^{18}O$ values, while oxygen isotope equilibrium between soil H_2O and soil carbonate at Site C is inconclusive. Carbon isotope equilibrium comparison suggests that spring and summer conditions are reflected in $\delta^{13}C$ values at both Sites B and C.

The timing of soil carbonate formation at Site D remains unclear. Comparison of modeled soil respiration rates based on soil carbonate and measured soil CO_2 $\delta^{13}C$ values suggests that spring time conditions are conducive to carbonate formation. However, carbonate $\delta^{13}C$ and $\delta^{18}O$ values were never matched by measured soil CO_2 $\delta^{13}C$ values and soil H_2O $\delta^{18}O$ values at any time during the study. The period of study during 2013-2014 was a time of decreased precipitation in the study area region with Palmer Drought Severity Ratings of ≤ -3 (NCDC-NOAA, 2015). While these below average precipitation conditions likely do not reflect average climate conditions during the 3.8ka of carbonate formation in these soils, the comparison of climate conditions between sites along the transect may still reflect relative differences and contrasts that are applicable and relevant even on low precipitation years.

5. Conclusions

This climosequence of four study sites at Fish Lake Valley in the western Great Basin indicates that the C and O stable isotope composition of soil CO_2, H_2O and carbonate change systematically with elevation and climate. At the valley floor site at 1482m elevation, soil

carbonate $\delta^{13}C$ and $\delta^{18}O$ values reflect soil isotopic conditions nearly year round, especially in the 25-50cm soil depth interval. At the mid-elevation sites of 1745m and 2140m spring through summer conditions were apparently recorded in $\delta^{13}C$ and $\delta^{18}O$ values of pedogenic carbonate. At the highest elevation site of 2602m, the C and O isotopes of carbonate never reflected measured soil CO_2 and H_2O conditions during the sampling period, though modeled soil respiration rates suggest that spring season conditions were most conducive to carbonate formation. These various estimates of the timing of pedogenic carbonate formation all occur within 20km distance of each other.

These results indicate that there is inherent difficulty or complexity in assigning a definitive timing of carbonate formation based on short-term (one or two year) field measurements of soil CO_2 and H_2O. Not withstanding these difficulties and inherent uncertainties, results from these sites indicate that in arid environments with distinctly seasonal rainfall, soil carbonate O stable isotope depth profiles can incorporate waters from differing time intervals and atmospheric circulation sources. This may result in the carbonate reflecting not one season of formation, but multiple seasons and their climatic signals. Together, these findings suggest that short-term monitoring, despite its weaknesses, helps to reveal the nature of the long term record isotopically recorded in soil carbonate.

6. References

Amundson, R., Stern, L., Baisden, T., and Wang, Y., 1998, The isotopic composition of soil and soil-respired CO2: Geoderma, v. 82, no. 1-3, p. 83-114.

Amundson, R. G., Doner, H. E., Chadwick, O. A., and Sowers, J. M., 1989, The stable isotope chemistry of pedogenic carbonates at Kyle Canyon, Nevada: Soil Science Society of America Journal, v. 53, no. 1, p. 201-210.

Araguas-Araguas, L., Rozanski, K., Gonfiantini, R., and Louvat, D., 1995, Isotope effects accompanying vacuum extraction of soil water for stable isotope analyses: Journal of Hydrology, v. 168, p. 159-171.

Arkley, R. J., 1963, Calculation of carbonate and water movement in soil from cliamtic data: Soil Science, v. 96, no. 4, p. 239-248.

Barnes, C. J., and Allison, G. B., 1983, The Distribution of Deuterium and O-18 in Dry Soils .1. Theory: Journal of Hydrology, v. 60, no. 1-4, p. 141-156.

Barnes, C. J., and Allison, G. B ., 1988, Tracing of Water-Movement in the Unsaturated Zone Using Stable Isotopes of Hydrogen and Oxygen: Journal of Hydrology, v. 100, no. 1-3, p. 143-176.

Barnes, C. J., and Turner, J. V., 1998, Isotopic Exchange in Soil Water, *in* Kendall, C., and McDonnell, J. J., eds., Isotope Tracers in Catchment Hydrology: Amsterdam, Elsevier, p. 137-163.

Breecker, D., and Sharp, Z. D., 2008, A field and laboratory method for monitoring the concentration and isotopic composition of soil CO2: Rapid Communications in Mass Spectrometry, v. 22, no. 4, p. 449-454.

Breecker, D. O., Sharp, Z. D., and McFadden, L. D., 2009, Seasonal bias in the formation and stable isotopic composition of pedogenic carbonate in modem soils from central New Mexico, USA: Geological Society of America Bulletin, v. 121, no. 3-4, p. 630-640.

Brenninkmeijer, C. A. M., Kraft, P., and Mook, W. G., 1983, Oxygen isotope fractionation between CO2 and H2O: Chemical Geology, v. 41, no. 0, p. 181-190.
Cerling, T., Solomon, D. K., Quade, J., and Bowman, J., 1991, On the isotopic composition of carbon in soil carbon dioxide: Geochimica et Cosmochimica Acta, v. 55, p. 3403-3405.
Cerling, T. E., 1984, The Stable Isotopic Composition of Modern Soil Carbonate and Its Relationship to Climate: Earth and Planetary Science Letters, v. 71, no. 2, p. 229-240.
Dansgaard, W., 1964, Stable Isotopes in Precipitation: Tellus, v. 16, no. 4, p. 436-468.
Epstein, S., and Mayeda, T., 1953, Variation of O< sup> 18</sup> content of waters from natural sources: Geochimica et cosmochimica acta, v. 4, no. 5, p. 213-224.
Ferretti, D., Pendall, E., Morgan, J., Nelson, J., Lecain, D., and Mosier, A., 2003, Partitioning evapotranspiration fluxes from a Colorado grassland using stable isotopes: seasonal variations and ecosystem implications of elevated atmospheric CO2: Plant and Soil, v. 254, no. 2, p. 291-303.
Francey, R., Allison, C., Etheridge, D., Trudinger, C., Enting, I., Leuenberger, M., Langenfelds, R., Michel, E., and Steele, L., 1999, A 1000-year high precision record of δ13C in atmospheric CO2: Tellus B, v. 51, no. 2, p. 170-193.
Gat, J. R., 1996, Oxygen and hydrogen isotopes in the hydrologic cycle: Annual Review of Earth and Planetary Sciences, v. 24, p. 225-262.
Gebauer, R. L., and Ehleringer, J. R., 2000, Water and nitrogen uptake patterns following moisture pulses in a cold desert community: Ecology, v. 81, no. 5, p. 1415-1424.
Gemery, P. A., Trolier, M., and White, J. W., 1996, Oxygen isotope exchange between carbon dioxide and water following atmospheric sampling using glass flasks: Journal of Geophysical Research: Atmospheres (1984–2012), v. 101, no. D9, p. 14415-14420.
Gile, L. H., Peterson, F. F., and Grossman, R. B., 1966, Morphological and Genetic Sequences of Carbonate Accumulation in Desert Soils: Soil Science, v. 101, no. 5, p. 347-&.
Grayson, D. K., 2011, The Great Basin: a natural prehistory, Univ of California Press.
Hall, C. A., 1991, Natural History of the White-Inyo Range, Eastern California, Univ of California Press.
Harden, J. W., Slate, J. L., Lamothe, P., Chadwick, O. A., Pendall, E., and Gillespie, A. R., 1991, Soil formation on the Trail Canyon Alluvial Fan, Fish Lake Valley, Nevada: US Department of the Interior, Geological Survey.
Hsieh, J. C. C., Savin, S. M., Kelly, E. F., and Chadwick, O. A., 1998, Measurement of soil-water delta O-18 values by direct equilibration with CO2: Geoderma, v. 82, no. 1-3, p. 255-268.
Jenny, H., 1941, Factors of soil formation: a system of quantitative pedology, New York, Courier Dover Publications, 191 p.:
Jenny, H., and Leonard, C., 1934, Functional relationships between soi lproperties and rainfall: Soil Science, v. 38, no. 5, p. 363-382.
Kim, S. T., and ONeil, J. R., 1997, Equilibrium and nonequilibrium oxygen isotope effects in synthetic carbonates: Geochimica et Cosmochimica Acta, v. 61, no. 16, p. 3461-3475.
Pendall, E. G., Harden, J. W., Trubmore, S. E., and Chadwick, O. A., 1994, Isotopic Approach to Soil Carbonate Dynamics and Implications for Paleoclimatic Interpretations: Quaternary Research, v. 42, no. 1, p. 60-71.
Peters, N. A., Huntington, K. W., and Hoke, G. D., 2013, Hot or not? Impact of seasonally variable soil carbonate formation on paleotemperature and O-isotope records from clumped isotope thermometry: Earth and Planetary Science Letters, v. 361, p. 208-218.

Phillips, D. L., and Gregg, J. W., 2001, Uncertainty in source partitioning using stable isotopes: Oecologia, v. 127, no. 2, p. 171-179.
Quade, J., Cerling, T. E., and Bowman, J. R., 1989, Systematic Variations in the Carbon and Oxygen Isotopic Composition of Pedogenic Carbonate Along Elevation Transects in the Southern Great-Basin, United-States: Geological Society of America Bulletin, v. 101, no. 4, p. 464-475.
Raich, J. W., and Schlesinger, W. H., 1992, The Global Carbon-Dioxide Flux in Soil Respiration and Its Relationship to Vegetation and Climate: Tellus Series B-Chemical and Physical Meteorology, v. 44, no. 2, p. 81-99.
Reheis, M. C., and Block, D., 2007, Surficial Geologic Map and Geochronologic Database, Fish Lake Valley, Esmeralda County, Nevada, and Mono County, California: United States Geological Survey.
Romanek, C. S., Grossman, E. L., and Morse, J. W., 1992, Carbon isotopic fractionation in synthetic aragonite and calcite: effects of temperature and precipitation rate: Geochimica et Cosmochimica Acta, v. 56, no. 1, p. 419-430.
Royer, D. L., 1999, Depth to pedogenic carbonate horizon as a paleoprecipitation indicator?: Geology, v. 27, no. 12, p. 1123-1126.
Schoeneberger, P. J., Wysocki, D. A., Benham, E. C., and Soil Survey Staff, 2012, Field book for describing and sampling soils, Version 3.0, National Soil Survey Center, Lincoln, NE., Natural Resources Conservation Service.
Soil Survey Staff, 1999, Soil taxonomy: a basic system of soil classification for making and interpreting soil surveys, Natural Resources Conservation Service, United States Department of Agriculture.
Stern, L., Baisden, W. T., and Amundson, R., 1999, Processes controlling the oxygen isotope ratio of soil CO2: Analytic and numerical modeling: Geochimica et Cosmochimica Acta, v. 63, no. 6, p. 799-814.
Summers, H., Smith, B., and Hansen, L., 2009, Comparison of respiratory and growth characteristics of two co-occurring shrubs from a cold desert, Coleogyne ramosissima (blackbrush) and Atriplex confertifolia (shadscale): Journal of arid environments, v. 73, no. 1, p. 1-6.
Wang, Y., McDonald, E., Amundson, R., McFadden, L., and Chadwick, O., 1996, An isotopic study of soils in chronological sequences of alluvial deposits, Providence Mountains, California: Geological Society of America Bulletin, v. 108, no. 4, p. 379-391.

Chapter 2:
Climate variability in mid-continent North America during the last 120,000 years revealed by oxygen, carbon and uranium isotopes in pedogenic carbonate

1. Introduction

Well dated, high resolution, records of paleoclimate in continental interiors with millennial resolution and continuity extending over tens of kiloyears are relatively rare and are commonly limited to cave deposits and lake sediment records. The rarity of these carbonates is in striking contrast to soil carbonate that is nearly ubiquitous in arid and semi-arid continental climates (e.g. Machette 1985). Here we show how these soil carbonates can form in such a way so as to preserve a quasi-continuous record of soil environmental conditions, and present a continuous millennial-scale paleoclimate reconstruction based on the O, C and U isotope composition of pedogenic carbonate accumulated over the last 120ka in the Wind River Basin of northwestern Wyoming. The Pleistocene climatic history of this region is important because of its proximity and sensitivity to the Laurentide and Cordilleran ice sheets, and presently there are only partial paleoclimate records for the latest Pleistocene (Amundson et al., 1996). In particular, the mid-continental location allows us to assess variation in hydroclimate response during the glacial-interglacial cycles of the late Pleistocene in comparison to other regional paleoclimate records and atmospheric circulation simulations (Winograd et al., 1992; Winograd et al., 2006; Dorale et al., 1998; Serefiddin et al., 2004; Maher et al., 2014; Oster et al., 2015).

The Wind River Basin of Wyoming contains a suite of Pleistocene fluvial terraces capped by soils that have persisted through multiple glacial-interglacial climates (Chadwick et al., 1997; Amundson et al., 1996). The soils contain clasts coated on the undersides with dense carbonate coatings that, on some cobbles, form sequences of submillimeter-thick, conformable laminations. Stable O isotopes in carbonate ($\delta^{18}O_c$) may reflect the O isotope composition of rainfall ($\delta^{18}O_p$), and laminations, that once formed, are geochemically closed systems retaining isotope compositions (Amundson et al., 1996; Sharp et al., 2003). While there is commonly an apparent relationship between mean annual temperature (MAT) and $\delta^{18}O_p$ values (Dansgaard, 1964; Gat, 1996) in mid-latitudes, storm source and trajectory also play a strong role in determining rainfall values, particularly in mid-continent North America (Amundson et al, 1996; Kendall and Coplen, 2001). The C stable isotope composition of pedogenic carbonate ($\delta^{13}C_c$) is controlled by the proportion of C3 to C4 type vegetation and the soil respiration rate, both affected by MAT and mean annual precipitation amount (MAP) (Cerling et al., 1984; Raich and Schlessinger, 1992).

When secondary carbonate forms in soil, ppm levels of U are incorporated and U-series disequilibrium dating of pedogenic carbonate is now an established geochronologic method (i.e. Ludwig and Paces, 2002; Sharp et al., 2003). During decay of ^{238}U to its daughter nuclide, ^{234}Th, an α particle (^{4}He) is ejected from the ^{238}U nucleus and the resulting ^{234}Th atom recoils some distance in the mineral matrix. If this recoil distance crosses a mineral grain boundary, the ^{234}Th atom will be ejected into the surrounding soil pore water where it decays to ^{234}U and is vulnerable to removal by soil water movement. As a result, the $^{234}U/^{238}U$ ratio during mineral precipitation ($^{234}U/^{238}U_i$, which may be back-calculated from the measured $^{234}U/^{238}U$ ratio and the associated U-Th age) is inversely related to the rate of soil water infiltration and is thus linked to changes in paleoprecipitation amount (Oster et al., 2012; Maher et al., 2014).

In this study we develop time series of O, C, and $^{234}U/^{238}U_i$ isotope ratios along profiles through dense, laminated pedogenic carbonate coatings. To do so, we have: (1) constructed age models constrained by closely spaced U-Th dates determined via laser ablation ICP-MS, and (2) determined O and C stable isotope ratios along the same profiles via SIMS. We compare these data with those of available paleoclimate records in the region to assess the potential of pedogenic carbonate to provide a record of long-term climate signals, and to refine our understanding of regional variations in climate and atmospheric circulation over the last 120ka.

2. Methods

2.1 Study location and samples

Clasts with attached carbonate rinds (Supp. Fig. 1) were collected from trenches in the surface of Terrace 4 of Chadwick et al., 1997 (43.198°, -108.769°; Fig. 1). Here, two samples from the depth of 46cm (samples A-2-07A, A-2-05B), and one from 111cm (A-4-01), were used for the research. The age of stabilization of Terrace 4 is estimated to be 167 ka (+/- 6.4) based on $^{230}Th/U$ dating of the innermost pedogenic carbonate coatings on clasts (Sharp et al., 2003). Each sample was halved by rock saw perpendicular to carbonate rind orientation, polished and inspected to locate regions of dense, translucent primary carbonate. The ~3mm thick rinds were then sub-sampled for U-series analysis by laser ablation inductively coupled plasma mass spectrometry (LA-ICP-MS) with 93µm diameter spots (Fig. 2, Supp. Figs 2-5), and for C and O isotope measurements by ion probe secondary ion mass spectrometry (SIMS) with ~10µm diameter sampling spots (Supp. Figs. 6-9, see methods below). Two radial age and isotope transects separated by ~2cm lateral distance on sample A-2-07A were analyzed to determine intra-sample variability. Intra-sample variability was determined by sampling along a several individual carbonate laminations (Table S3).

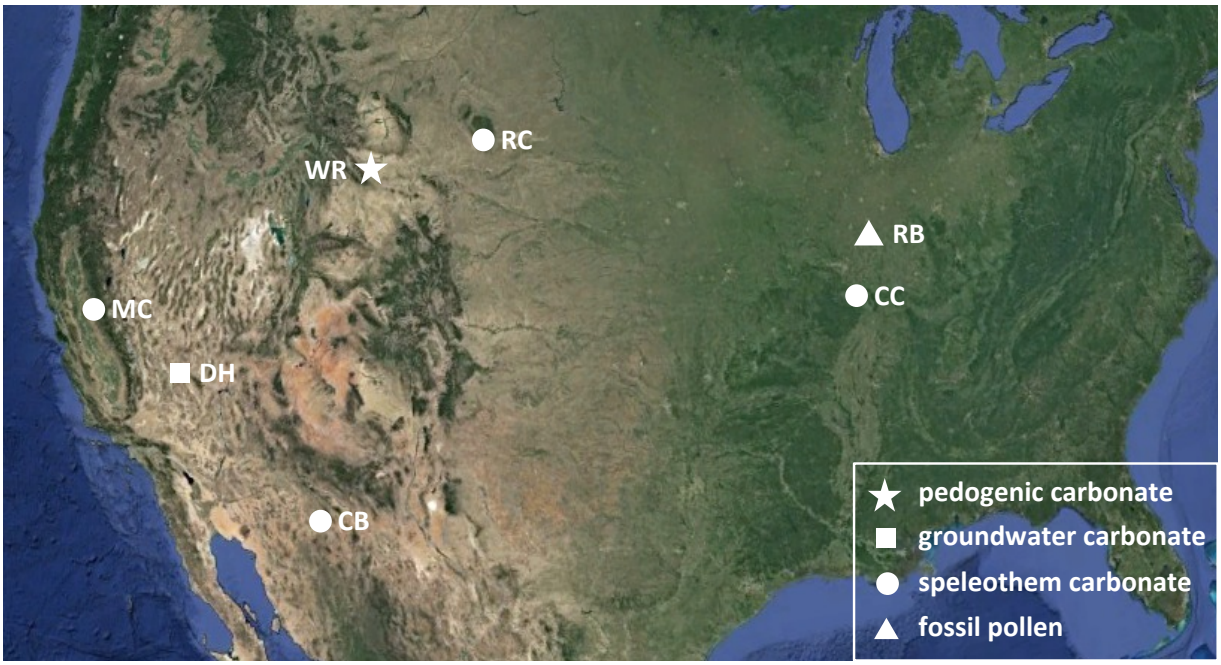

Figure 1. Map of mid-latitude North America with locations discussed in text; WR: Wind River Basin, Wyoming; RC: Reed's Cave, South Dakota; CC: Crevice Cave, Missouri; DH: Devil's Hole, Nevada; MC: Mclean's Cave, California; CB: Cave of the Bells, Arizona; RB: Raymond Basin, Illinois.

We also compared coeval carbonate samples A-2-07A and A-2-05B from the same depth but different locations in the soil. We propose that if comparison of results on coeval samples from the same depth, but different locations in the soil are replicable, it suggests that the isotopic processes occurring in the soil are not dominated by clast-scale processes, but are reflective of conditions throughout the soil. The three transects on two samples from the same soil depth have similar $\delta^{13}C_c$, $\delta^{18}O_c$ and $^{234}U/^{238}U_i$ trends (Supp. Figs 6-9), and thus a composite dataset was created by merging these data and smoothing variations with a 3-pt moving average (Figs. 3 and 4, Supp Figs 6-9). The composite dataset is referred to as WR A-2.

2.2 ^{230}Th/U dating

Laser ablation U-Th analyses were made at the University of Melbourne using a Nu Plasma ICP-MS with 193nm HelEx laser ablation system. All U and Th isotopes were measured simultaneously using known ion counter gains, the $^{238}U/^{235}U$ ratio to evaluate mass bias, and on-peak baselines. To correct for U-Th fractionation during laser ablation, carbonate samples were milled with 0.3 mm carbide dental burrs along the laser traverses and measured in solution mode at the Berkeley Geochronology Center using a Thermo-Fisher Neptune Plus ICP-MS. $\delta^{13}C_c$ and $\delta^{18}O_c$ analysis spot ages with uncertainties were modeled along the age axis with the StalAge program (Scholz and Hoffmann, 2011).

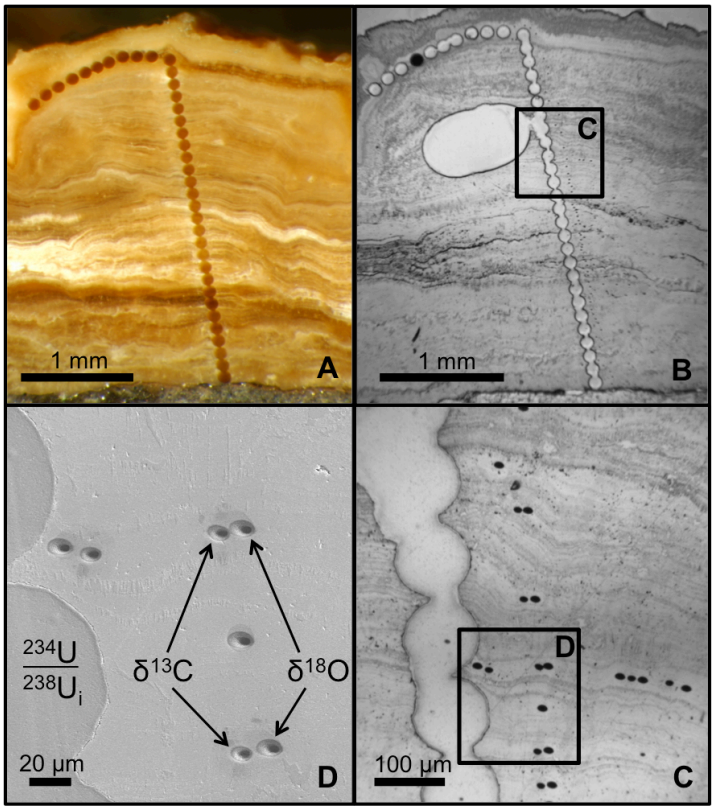

Figure 2. Reflected light photomicrographs of sample A-2-07A Traverse B. (A) LA-ICPMS time transgressive analysis transect across pedogenic carbonate laminations; (B) ^{230}Th/U powder calibration sample taken from white oval; (C) Magnified area of box in (B) showing arrangement of paired C and O analysis spots, vertically transects are along age axis, horizontal are synchronous along carbonate lamination; (D) Magnified area of box in (C) showing spatial arrangement of C, O and U analysis spots.

2.3 $\delta^{18}O_c$ and $\delta^{13}C_c$ analysis by SIMS

$\delta^{18}O_c$ and $\delta^{13}C_c$ values were measured with ion beam sampling and secondary ion mass spectrometery (SIMS) at the WiscSIMS Laboratory, University of Wisconsin - Madison. Samples of the full-thickness carbonate rinds along with small portions of the attached clasts of approx. 4mm thickness and 5mm width were cut from the larger samples, cast into ~25mm round epoxy (Buehler Epo-Thin) mounts with several grains of UWC-3 calcite standard ($\delta^{18}O_c$ = -17.88‰ VPDB; $\delta^{13}C_c$ = -0.91‰ VPDB; (Kozdon et al., 2009). These mounts were polished by hand on rotary disc laps with 9 μm and then 3 μm size alumina-water slurry. Additional rotary machine polishing was done with 3 μm and 0.25 μm diamond paste in oil, followed by a final hand polish by rotary lap with colloidal silica solution (0.05 μm), providing a nearly perfectly-flat polished surface. The polished samples were then sputter coated with Au to a thickness of ~60 nm. Samples were inspected with a Hitachi S3400N scanning electron microscope at approx. 1000x magnification in secondary electron (SE) and back scattered electron (BSE) modes to identify the most suitable SIMS sampling domains according to the criteria of: the most visibly pure carbonate with no inclusions or discernable laminations with no other phases present, and no cracks or voids in the sample surface. In the CAMECA IMS 1280 large radius ion microprobe multicollector instrument, a ~1.7 nA 133Cs+ ion beam is focused into a spot size ~10 um in diameter and applied to the sample surface creating sampling pits ~1um deep by ablating ~2ng of carbonate. Precision on these samples for $\delta^{18}O_c$ values are ≤ ±0.30‰ (2SD) and $\delta^{13}C_c$ values are ≤ ±1.47‰ (but more typically ca. ±0.70‰) (2SD), as determined by multiple analysis spots on UWC-3 standard calcite before and after sample analyses using standard-sample-standard bracketing with 4 standard analyses before and after 10-15 sample measurements (Kita et al., 2009). Post-SIMS analysis, samples were again imaged by SEM to evaluate SIMS pits for appropriate location, absence of cracks or inclusions revealed inside the pit and for symmetric pit shape.

2.4 Assessment of $\delta^{18}O_c$ and $\delta^{13}C_c$ variability along carbonate laminations

An important aspect in determining whether or not $\delta^{13}C_c$ and $\delta^{18}O_c$ values can be interpreted in terms of climatic influence is the extent to which equilibrium fractionation can be assumed, or if other processes yielding kinetic fractionation are present. We performed paired C and O isotope analyses along carbonate laminations on three laminations from sample A-2-07A to examine the variability within carbonate of similar age (Supp. Table 3). These three individual carbonate laminations of differing ages do not show variability in $\delta^{13}C_c$ values within 2SD uncertainty limits of individual analysis spots, and while $\delta^{18}O_c$ values show more variability along lamination, the average of $\delta^{18}O_c$ shows similar variability as individual spots. We interpret these along lamination transects to confirm that carbonate of similar ages is relatively isotopically homogeneous at the spatial scale of individual SIMS analysis spots (~10um).

3. Modern climate in the Wind River Basin

We now focus on interpreting the record in terms of climate change. The modern MAT and MAP at Terrace 4 in Wyoming interpolated from 117 years of data is 6.3°C (± 0.8°C) and 231mm (± 70mm) (PRISM Group, 2015). Non-summer (months excluding JJAS) precipitation is dominated by zonal storm flow from the west originating in the north Pacific, with average $\delta^{18}O_p$ values of -15.0‰ (61% of MAP), while summer (JJAS) meridional flow arrives from the Gulf of Mexico (GOM) to the south with average $\delta^{18}O_p$ values of -10.85‰ (39% of MAP) (Bryson and Hare, 1974; Liu et al., 2010; IsoMAP, 2015). Weighted average annual $\delta^{18}O_p$

values are -13.4‰ (VSMOW), and at isotopic equilibrium would form $\delta^{18}O_c$ with values of -11.3‰ (VPDB) at modern MAT. These values are similar to the early Holocene $\delta^{18}O_c$ value observed in the WR A-2 record (Figs. 2B and 3B, Supp. Fig. 6-9). Carbonate sampled from Holocene terraces in the Wind River Basin has average $\delta^{13}C_c$ values of -3.6‰ (±0.6‰) (VPDB) (Amundson et al., 1996), which is similar to the youngest $\delta^{13}C_c$ values from the WR A-2 record (Figs. 3F, 4C). In total, the similarities of the youngest laminations to modern conditions support the interpretation that laminations reflect general soil conditions and suggest that modern isotopic conditions have varied little since the mid-Holocene.

4. Paleoclimate in Wind River Basin during the last 120ka

4.1 Paleoclimate after the penultimate glaciation

The WR $\delta^{18}O_c$ record begins ca. 120ka, though some of our data are older with lower precision (Supp. Table 2), and records low amplitude changes in $\delta^{18}O_c$ values of ca. 1‰ (Fig. 3B) that are sometimes in phase with solar insolation trends (Fig. 3A) of Marine Isotope Stage (MIS) 5 (Lisiecki and Raymo, 2005). The WR A-2 $\delta^{18}O_c$ values at ca. 100ka and 80ka are similar to $\delta^{18}O_c$ values recorded in the Devils Hole (DH) phreatic carbonate $\delta^{18}O_c$ record from the Mojave Desert (Fig. 1, Figs. 3B and 3E) (Winograd et al., 1992; Winograd et al., 2006).

$\delta^{13}C_c$ values in WR A-2 between 120 to 100ka decrease (Fig 3F) and are interpreted to reflect warming and increased soil and plant respiration rates during the warming during glacial Termination II (Broecker and Henderson, 1998). From 100 to 80ka, $\delta^{13}C_c$ values increase (Fig 3F), likely resulting from a corresponding decrease in respiration rates, from both drier and/or colder conditions that inhibit biological activity. Dry conditions are also supported by higher $^{234}U/^{238}U_i$ values during this time (Fig. 3H). A shift in vegetation C3/C4 ratios could also explain changes in $\delta^{13}C_c$ values, but there is no evidence of this in the Wind River Basin region (Baker, 1983). This time period in central North America is proposed to have formed the Sangamon geosol, a weathered and oxidized paleosol that is interpreted to have formed in warm temperatures with varying degrees of humidity (Curry and Baker, 2000). More detailed resolution of the climate in this interval is limited by the slow rates of carbonate formation (ca. 10μm ka^{-1}) from 120 to 90ka (Fig. 3G).

From 75 to 55ka, which largely overlaps MIS 4, $\delta^{18}O_c$ values sharply increase (Fig. 3B). The increase in WR A-2 $\delta^{18}O_c$ values between 75 and 55ka, at a time when the DH carbonate decreased, is an important pattern. At Devil's Hole, colder sea surface temperatures led to a decrease in precipitation $\delta^{18}O_p$ values reflecting globally cooler conditions during MIS 4. However, an increase in mid-continent $\delta^{18}O_p$ has been observed in speleothems from Reed's Cave, South Dakota (Serefiddin et al., 2004) (Figs. 1 and 3C), and Crevice Cave, Missouri (Dorale et al., 1998) (Figs. 1 and 3D). The ~4‰ increase in $\delta^{18}O_c$ values at Wind River is similar to Reed's Cave. Fractionation due to temperature is fairly small (0.25% $°C^{-1}$) relative to the range of change in $\delta^{18}O_c$ values, and should also have affected DH in a related manner. Lower summer solar insolation during MIS 4 (Fig. 3A), and globally cooler temperatures (Sachs and Lehman, 1999) are inconsistent with soil water isotopic enrichment from excessive evaporation. Thus, the regional increase in $\delta^{18}O_c$ values during this time interval is most suggestive of a shift in the source or seasonal balance of precipitation in Central North America (CNA).

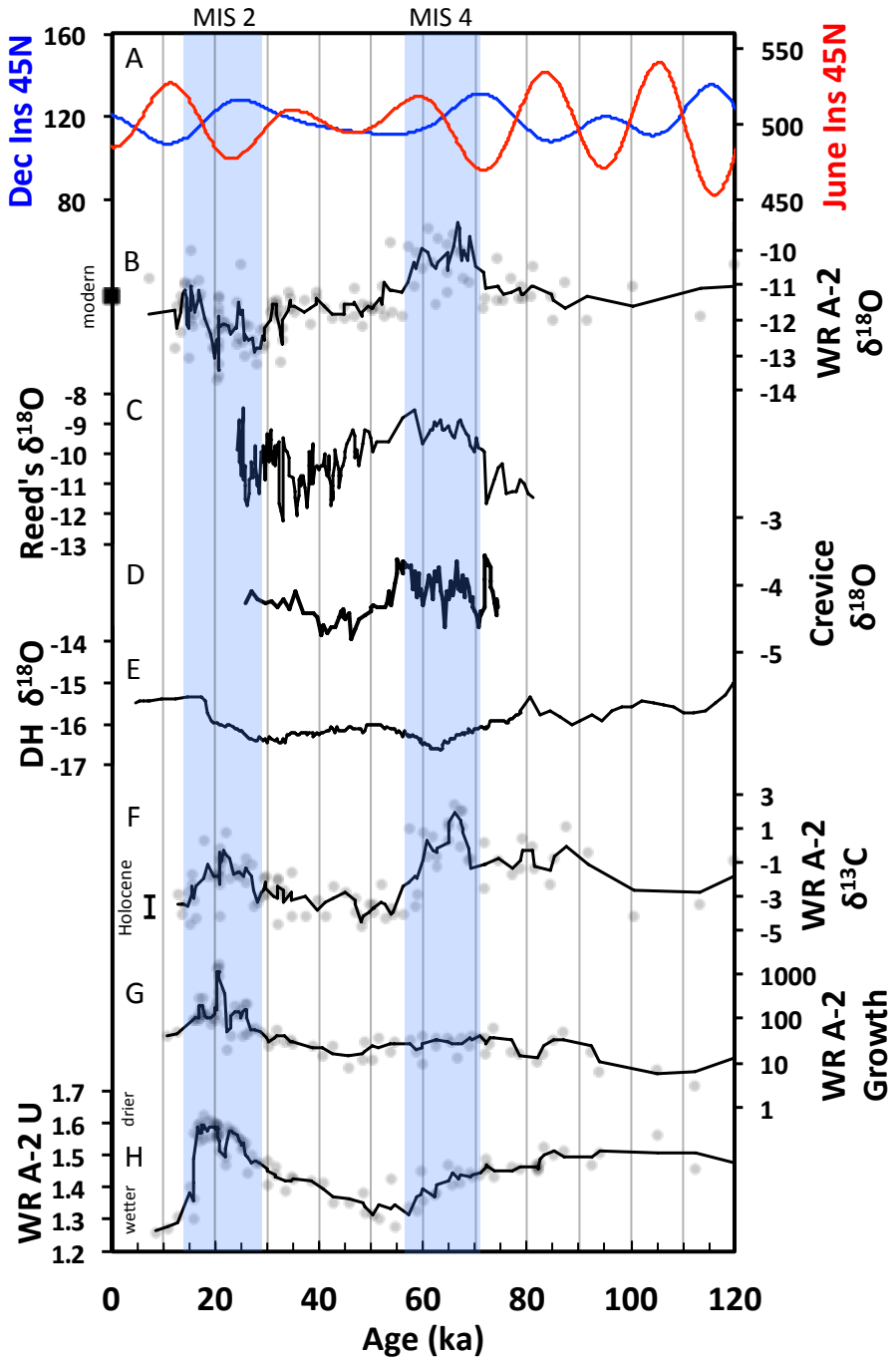

Figure 3. Comparison of solar insolation and regional paleoclimate records for the last 120 ka. WR A-2 records are 3 pt. moving averages (heavy line) through grey data, comparison record heavy lines are point to point (not 3pt). (A) Solar insolation trends (watts m^{-2}) at 45°N latitude for June (red) and December (blue) (Laskar et al., 2004); (B) Wind River composite A-2 $\delta^{18}O_c$ record, modern $\delta^{18}O_c$ calculated from weighted annual average $\delta^{18}O_p$ and MAT; (C) Reed's Cave $\delta^{18}O_c$ record; (D) Crevice Cave $\delta^{18}O_c$ record; (E) Devil's Hole $\delta^{18}O_c$ record; (F) Wind River composite A-2 $\delta^{13}C_c$ record, Holocene $\delta^{13}C_c$ values; (G) Wind River composite A-2 carbonate growth rate (μm ka^{-1}); (H) Wind River composite A-2 $^{234}U/^{238}U_i$ record; all δ values referenced to VPDB standard. Blue shaded bars denote MIS 2 and 4.

Today the Wind River Basin receives 61% of its MAP by non-summer (months excluding JJAS) moisture from the north Pacific by zonal westerly flow. Summer (JJAS) rain from the Gulf of Mexico is delivered via meridional flow (39% of MAP) (Bryson and Hare, 1974; Liu et al., 2010; IsoMAP, 2015). The relative proportion of each of these two moisture sources is controlled by the North Atlantic Subtropical High (NASH) end of the North Atlantic Oscillation dipole: wetter summers are associated with a strong and west-based NASH (the Bermuda High, BH) (Chang and Smith, 2001). Pedogenic carbonate forms when soil is drying (Breecker et al., 2009), reflecting summer temperature and soil moisture.

The proportion of summer to winter precipitation required to produce pedogenic carbonate with $\delta^{18}O_c$ values similar to those in the A-2 record during MIS 4 (–9.87‰, the average of 10 measurements of $\delta^{18}O_c$ from the Terrace 4 locality during the period 65-70 ka (Fig. 2A)) can be estimated by using modern values of seasonal $\delta^{18}O_p$. With $\alpha_{H2O\text{-}CaCO3}$ corresponding to modern MAT, wetter summers with 72% of modern MAP produce $\delta^{18}O_c$ values of –9.86‰. Using $\alpha_{H2O\text{-}CaCO3}$ corresponding to MAT during MIS 4 estimated to be 2°C cooler (the summertime and warmer end of yearly average changes of 2-5°C; (Sachs and Lehman, 1999), with modern $\delta^{18}O_p$ values, summers with 59% of MAP are required to produce the high $\delta^{18}O_c$ values observed in the WR A-2 record during MIS 4. Based on this analysis, MIS 4 summers contributed 20-33% more relative precipitation balance than today. Model-based simulations of paleoatmospheric circulation in CNA indicate differences in seasonality during MIS 4 as compared to the LGM, with 2°C warmer summers, while winters were 1°C warmer, than during the LGM (Löfverström et al., 2014).

WR A-2 $\delta^{13}C_c$ values during MIS 4 peak at ca. 65ka (Fig. 3F). Assuming no change in C3/C4 ratios (Baker, 1983), this indicates a decline in soil respiration rates, which may be due to much colder average temperatures. MAT in Wyoming during late Pleistocene glacials may have been 10 to 16°C colder than the present based on prevalent ice wedges and frost polygons (Visser et al., 1996). Alternatively, these times may have favored an increase in C4 grasses, which tolerate higher water stress. The CNA appears to have become more prairie-like, with pronounced contrast between wet and dry seasons, based on the speleothems in South Dakota and Missouri which also record high $\delta^{13}C_c$ values during between 70 to 53ka (Dorale et al., 1998; Serefiddin et al., 2004). Pollen in the Raymond Basin in Illinois (Fig. 1), indicates the period was marked by warm summers and flowing surface water (Curry and Baker, 2000). There are sharp declines of up to 5‰ in $\delta^{18}O_c$ and $\delta^{13}C_c$ values between 65ka and 55ka (Fig. 3B and 3F). The lower $\delta^{13}C_c$ values indicate wetter conditions, a situation supported by decreases in $^{234}U/^{238}U_i$ values (Fig. 3H) due to greater soil water infiltration. Speleothems in South Dakota and Missouri also have decreases in $\delta^{18}O_c$, though they lag WR A-2 by ~5ka (Figs. 3C and 3D).

The WR A-2 $\delta^{18}O_c$ record responds in phase, but inversely, to the Devil's Hole $\delta^{18}O_c$ record between 75 to 50ka (Fig. 3B and 3E). Devil's Hole reflects winter-dominated conditions because its aquifer recharge area is dominated by winter-spring zonal precipitation, and is thought to reflect variations in sea surface temperatures off of California (Coplen, 2007; Winograde et al., 2006). A speleothem from McLean's Cave in the Sierra Nevada of California also has reduced $\delta^{18}O_c$ and $\delta^{13}C_c$ values at 60ka, a period synchronous with the minima in $\delta^{18}O_c$ values in the DH record (Fig. 3E) (Oster et al., 2014). DH and McLean's Cave both seem to reflect temperature along the western margin of North America during MIS 4 and the MIS 3/4 warming transition that had colder sea surface temperatures. However, the WR soil carbonate and mid-continent cave records suggest a decoupling of winter and summer season atmospheric circulation over North America during this interval.

MIS 4 was a time of high global ice volume, based on $\delta^{18}O$ values in Greenland ice cores (NGRIP members, 2004), likely due to the size of the Laurentide Ice Sheet, which reached 80-90% of its LGM mass (Stokes et al., 2012), but did not achieve the same southerly extent (Klemen et al., 2010). The continental ice during MIS 4 was variable worldwide, with Asian and southern hemisphere alpine glaciers reaching a maximum not attained since, while in Europe and North America glacial conditions where less than that of the LGM (Hughes et al., 2013). The unique regional climate that appears to have evolved in CNA during this time may result from the lack of southern ice sheet growth, which allowed unique atmospheric circulation patterns to develop.

4.2 Paleoclimate during MIS 3

Between 50 to 35ka, the WR A-2 $\delta^{18}O_c$ record has low amplitude variability of ca. 1‰ between -11‰ and -12‰ (VPDB), values similar to today (Fig. 3B). Decreasing WR A-2 $\delta^{18}O_c$ values at 33ka seems correspond to the abrupt cooling of Dansgaard-Oeschger (DO) cycles 5 and 6 (Fig. 4A and 4B), a change reflected in Reed's Cave $\delta^{18}O_c$ (Fig. 3C). The WR A-2 $\delta^{13}C_c$ record increases through time from a minimum of -5‰ at 50ka (VPDB), the lowest $\delta^{13}C_c$ values of the last 120ka (Fig. 3F). From 50 to 30ka, the increasing values indicate a shift toward lower respiration, while the increasing $^{234}U/^{238}U_i$ ratios suggest decreasing soil leaching (Fig. 3H). This trend towards aridity in Wyoming is not evident in records from Devils Hole (Fig. 3E), or in a speleothem from Cave of the Bells in Arizona (not shown) (Wagner et al., 2010). These differences from south to north in western North America during MIS 3 may be due to the increasing influence of the Laurentide Ice Sheet as it is expanded and its leading edge moved southward, especially during the MIS 2/3 transition (Kutzbach et al., 1998; Maher et al., 2014; Oster et al., 2015).

4.3 Paleoclimate during the last glaciation

WR A-2 $\delta^{18}O_c$ values decrease synchronously with summer solar insolation between 31 and 28ka (Fig. 3A and 3B). A $\delta^{18}O_c$ minimum at 27.5ka corresponds to cooling during Dansgaard-Oeschger (DO) cycles 3 and 4 (Figs. 4A and 4B). Increasing $\delta^{18}O_c$ values from 27 to 24ka also occur in Reed's Cave and to a lesser degree in Crevice Cave (Fig. 3B and 3C). A synchronous increase in $\delta^{13}C_c$ values continues before reaching a maximum at 21ka (Fig. 3F and 4C), indicating increasing aridity also reflected by increasing $^{234}U/^{238}U_i$ ratios (Figs. 3H and 4E). The periglacial aridity during the LGM at Wind River appears to be caused by a steering of the jet stream to the south by the combined effects of the persistent anticyclone developed above the LIS, a strong North Pacific high pressure system, and a southward-displaced Aleutian Low (Oster et al., 2015).

WR A-2 $\delta^{18}O_c$ values abruptly decline at 24ka, synchronous with the Heinrich Event 2, a disgorging of glacial ice into the northern oceans (Hemming, 2004). The surge in LIS growth may have increased the steering effect of the ice on the jet stream and storm track, strengthening the aridity observed in the $^{234}U/^{238}U_i$ record (Fig. 4E). From 22 to 20.5ka there are profound perturbations in the O, C and U isotope records, a time that reflects the Last Glacial Maximum (LGM) before deglaciation began in North America (Clark et al., 2009). After 20ka, $\delta^{18}O_c$ values increase by 2‰ reflecting warming conditions until 17ka, when they decrease by about 1‰ in concert with the onset of Heinrich Stadial 1 (Fig. 4B), during which the southwestern margin of the LIS reached its maximum extent (Lowell et al., 1999). The persistent continental –scale aridity dipole is recorded in the WR A-2 record by high $^{234}U/^{238}U_i$ values though the LGM up to

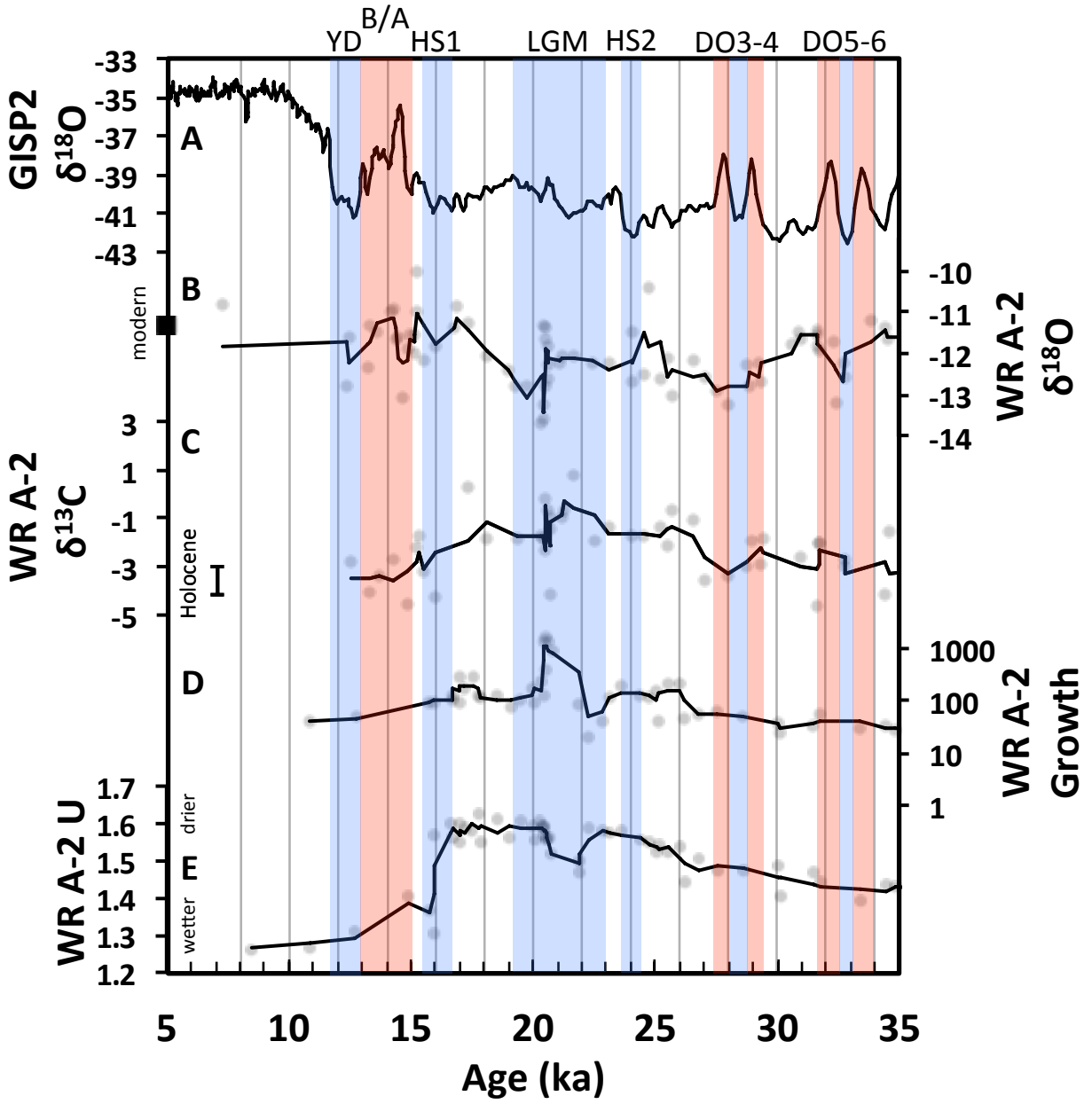

Figure 4. Comparison of the Wind River A-2 composite dataset to Greenland ice core records and global climatic events during 35 to 5 ka (3 pt. moving averages (heavy lines) through grey data); (A) GISP2 $\delta^{18}O$ (VSMOW) ice core record from Greenland (Grootes and Stuiver, 1997); (B) Wind River composite A-2 $\delta^{18}O_c$ (VPDB) record, modern $\delta^{18}O_c$ calculated from weighted annual average $\delta^{18}O_p$ and MAT; (C) Wind River composite A-2 $\delta^{13}C_c$ (VPDB) record, Holocene $\delta^{13}C_c$ values; (D) Wind River composite A-2 carbonate growth rate (μm ka^{-1}); (E) Wind River composite A-2 $^{234}U/^{238}U_i$ record. B/A: Bolling-Allerod, DO: Dansgaard-Oeschger cycles, HS: Heinrich Stadials (centered on Heinrich Events (*36*)), LGM: Last Glacial Maximum, YD: Younger-Dryas. Red bars indicate warm periods, blue bars indicate cold periods.

just after 17ka, followed by an abrupt change to wetter conditions (lower $^{234}U/^{238}U_i$ values) by 16ka (Fig. 4E).

The Bolling-Allerod warming period is reflected in increasing $\delta^{18}O_c$ values from 14 to 13ka (Fig. 4B), and by smaller increases in $^{234}U/^{238}U_i$ values. During the most recent deglaciation, the WR A-2 $\delta^{18}O_c$ pattern is generally similar to oscillations at Devils Hole (Figs. 3B and 3E), though the WR A-2 record shows more detail. This suggests that even though there was a dipole contrast in precipitation amounts over western North America from southwest to northeast, the entire region was dominated by the same zonal winter westerly flow, indicating the absence of a strong Bermuda High in the Atlantic during this glacial maximum, in contrast to MIS 4.

5. Conclusions

We demonstrate here the largely untapped potential of laminated pedogenic carbonates to provide high-resolution paleoclimate records. These records are observable using micron-scale sampling methods for both U-series dating and stable isotope analyses. In soils, the U isotope data provide an additional and powerful proxy of precipitation and soil water flux, which provides complementary information to C and O isotope data. The temporal resolution of soil carbonates appears to vary with climatic changes, and in Wyoming, high temporal resolution of up to 100 years is available during interesting latest Pleistocene climate intervals. These carbonates also have the advantage of recording the terrestrial paleoclimate at that precise soil location, rather than integrating the climate signal over a watershed or regional aquifer like speleothem or groundwater carbonates may do.

In general, the soil carbonate isotope record from Wyoming provides a record that largely conforms to the Devil's Hole groundwater carbonate record, and to the Greenland ice core O isotope record. However, the data from Wyoming and two regional caves show that there was a regional shift in precipitation sources during MIS 4, one where summer precipitation from the Gulf of Mexico became a major source of soil and vadose zone water.

There appear to be a wealth of carbonate rich soils around the world where this approach may have potential, ultimately making a temporally and spatially rich climate records possible for numerous continents. Additionally, the sedimentary record likely retains gravelly fossil soils with preserved carbonate laminations, potential records that when coupled to appropriate geochronologic methods, will allow environmental reconstructions of the more distant past.

6. References

Amundson, R., Chadwick, O., Kendall, C., Wang, Y., and DeNiro, M., 1996, Isotopic evidence for shifts in atmospheric circulation patterns during the late Quaternary in mid-North America: Geology, v. 24, no. 1, p. 23-26.

Baker, R. G., 1983, Holocene vegetation history of the western United States, *in* Wright, H. E. J., ed., Late Quaternary Envrionments of the United States. Volume 2. The Holocene: Minneapolis, University of Minnesota Press, p. 109-127.

Breecker, D. O., Sharp, Z. D., and McFadden, L. D., 2009, Seasonal bias in the formation and stable isotopic composition of pedogenic carbonate in modem soils from central New Mexico, USA: Geological Society of America Bulletin, v. 121, no. 3-4, p. 630-640.

Bryson, R. A., and Hare, R. K., 1974, The climate of North America, *in* Bryson, R. A., and Hare, R. K., eds., Climates of North America (World Survey of climatology, volume 11): New York, Elsevier, p. 1-47.

Cerling, T. E., 1984, The Stable Isotopic Composition of Modern Soil Carbonate and Its Relationship to Climate: Earth and Planetary Science Letters, v. 71, no. 2, p. 229-240.
Chadwick, O. A., Hall, R. D., and Phillips, F. M., 1997, Chronology of Pleistocene glacial advances in the central Rocky Mountains: Geological Society of America Bulletin, v. 109, no. 11, p. 1443-1452.
Chang, F.-C., and Smith, E. A., 2001, Hydrological and dynamical characteristics of summertime droughts over US Great Plains: Journal of climate, v. 14, no. 10, p. 2296-2316.
Coplen, T. B., 2007, Calibration of the calcite–water oxygen-isotope geothermometer at Devils Hole, Nevada, a natural laboratory: Geochimica et Cosmochimica Acta, v. 71, no. 16, p. 3948-3957.
Curry, B. B., and Baker, R. G., 2000, Palaeohydrology, vegetation, and climate since the late Illinois Episode (~ 130 ka) in south-central Illinois: Palaeogeography, Palaeoclimatology, Palaeoecology, v. 155, no. 1, p. 59-81.
Dansgaard, W., 1964, Stable Isotopes in Precipitation: Tellus, v. 16, no. 4, p. 436-468.
Dorale, J. A., Edwards, R. L., Ito, E., and González, L. A., 1998, Climate and vegetation history of the midcontinent from 75 to 25 ka: a speleothem record from Crevice Cave, Missouri, USA: Science, v. 282, no. 5395, p. 1871-1874.
Gat, J. R., 1996, Oxygen and hydrogen isotopes in the hydrologic cycle: Annual Review of Earth and Planetary Sciences, v. 24, p. 225-262.
Hughes, P. D., Gibbard, P. L., and Ehlers, J., 2013, Timing of glaciation during the last glacial cycle: evaluating the concept of a global 'Last Glacial Maximum'(LGM): Earth-Science Reviews, v. 125, p. 171-198.
IsoMAP, 2015, IsoMAP: Isoscapes Modeling, Analysis and Prediction (version 1.0), http://isomap.rcac.purdue.edu:8080/gridsphere/gridsphere.
Kendall, C., and Coplen, T. B., 2001, Distribution of oxygen-18 and deuterium in river waters across the United States: Hydrological Processes, v. 15, no. 7, p. 1363-1393.
Kita, N. T., Ushikubo, T., Fu, B., and Valley, J. W., 2009, High precision SIMS oxygen isotope analysis and the effect of sample topography: Chemical Geology, v. 264, no. 1-4, p. 43-57.
Kleman, J., Jansson, K., De Angelis, H., Stroeven, A. P., Hättestrand, C., Alm, G., and Glasser, N., 2010, North American Ice Sheet build-up during the last glacial cycle, 115–21kyr: Quaternary Science Reviews, v. 29, no. 17, p. 2036-2051.
Kozdon, R., Ushikubo, T., Kita, N., Spicuzza, M., and Valley, J. W., 2009, Intratest oxygen isotope variability in the planktonic foraminifer N. pachyderma: real vs. apparent vital effects by ion microprobe: Chemical Geology, v. 258, p. 327-337.
Liu, Z. F., Bowen, G. J., and Welker, J. M., 2010, Atmospheric circulation is reflected in precipitation isotope gradients over the conterminous United States: Journal of Geophysical Research-Atmospheres, v. 115, p. D22120.
Löfverström, M., Caballero, R., Nilsson, J., and Kleman, J., 2014, Evolution of the large-scale atmospheric circulation in response to changing ice sheets over the last glacial cycle: Climate of the Past Discussions, v. 10, no. 2, p. 1381-1420.
Lowell, T. V., Hayward, R. K., and Denton, G. H., 1999, Role of climate oscillations in determining ice-margin position: hypothesis, examples, and implications: Special Papers-Geological Society of America, p. 193-203.

Ludwig, K. R., and Paces, J. B., 2002, Uranium-series dating of pedogenic silica and carbonate, Crater Flat, Nevada: Geochimica et Cosmochimica Acta, v. 66, no. 3, p. 487-506.
Machette, M. N., 1985, Calcic soils of the southwestern United States, *in* Weide, D. L., and Faber, M. L., eds., Soils and quaternary geology of the Southwestern United States, Volume 203: Boulder, CO, Geological Society of America, p. 1-21.
Maher, K., Ibarra, D. E., Oster, J. L., Miller, D. M., Redwine, J. L., Reheis, M. C., and Harden, J. W., 2014, Uranium isotopes in soils as a proxy for past infiltration and precipitation across the western United States: American Journal of Science, v. 314, no. 4, p. 821-857.
NGRIP Members, 2004, High-resolution record of Northern Hemisphere climate extending into the last interglacial period: Nature, v. 431, no. 7005, p. 147-151.
Oster, J. L., Ibarra, D. E., Harris, C., and Maher, K., 2012, Influence of eolian deposition and rainfall amounts on the U-isotopic composition of soil water and soil minerals: Geochimica et Cosmochimica Acta, v. 88, p. 146-166.
Oster, J. L., Ibarra, D. E., Winnick, M. J., and Maher, K., 2015, Steering of westerly storms over western North America at the Last Glacial Maximum: Nature Geoscience, no. 23 February 2015, p. 1-5.
PRISM Climate Group, 2015, Gridded climate data for the contiguous USA, http://prism.oregonstate.edu.
Raich, J. W., and Schlesinger, W. H., 1992, The Global Carbon-Dioxide Flux in Soil Respiration and Its Relationship to Vegetation and Climate: Tellus Series B-Chemical and Physical Meteorology, v. 44, no. 2, p. 81-99.
Sachs, J. P., and Lehman, S. J., 1999, Subtropical North Atlantic temperatures 60,000 to 30,000 years ago: Science, v. 286, no. 5440, p. 756-759.
Scholz, D., and Hoffmann, D. L., 2011, StalAge–an algorithm designed for construction of speleothem age models: Quaternary Geochronology, v. 6, no. 3, p. 369-382.
Serefiddin, F., Schwarcz, H. P., Ford, D. C., and Baldwin, S., 2004, Late Pleistocene paleoclimate in the Black Hills of South Dakota from isotope records in speleothems: Palaeogeography, Palaeoclimatology, Palaeoecology, v. 203, no. 1, p. 1-17.
Sharp, W. D., Ludwig, K. R., Chadwick, O. A., Amundson, R., and Glaser, L. L., 2003, Dating fluvial terraces by 230Th/U on pedogenic carbonate, Wind River Basin, Wyoming: Quaternary Research, v. 59, no. 2, p. 139-150.
Stokes, C. R., Tarasov, L., and Dyke, A. S., 2012, Dynamics of the North American Ice Sheet Complex during its inception and build-up to the Last Glacial Maximum: Quaternary Science Reviews, v. 50, p. 86-104.
Visser, N., Heasler, H. P., and Mears, B., 1996, Late Pleistocene air temperatures in the Bighorn Basin, Wyoming: inferences from periglacial ice-wedge casts and the numerical modeling of near-surface ground temperatures, Resources of the Bighorn Basin; 47th Annual Field Conference Guidebook, Wyoming Geological Association, p. 329-337.
Winograd, I. J., Coplen, T. B., Landwehr, J. M., Riggs, A. C., Ludwig, K. R., Szabo, B. J., Kolesar, P. T., and Revesz, K. M., 1992, Continuous 500,000-Year Climate Record from Vein Calcite in Devils-Hole, Nevada: Science, v. 258, no. 5080, p. 255-260.
Winograd, I. J., Landwehr, J. M., Coplen, T. B., Sharp, W. D., Riggs, A. C., Ludwig, K. R., and Kolesar, P. T., 2006, Devils Hole, Nevada, [delta]18O record extended to the mid-Holocene: Quaternary Research, v. 66, no. 2, p. 202-212.

Chapter 3:
Oligocene to Early Miocene Climatic Oscillations in the Atacama Desert of Northern Chile

1. Introduction

The detailed climate history of the present hyper-arid Atacama Desert of northern Chile is poorly known, but outlines of the history can be constructed from a variety of methods. In the Mesozoic, arid conditions are interpreted to have existed based on the presence of evaporite deposits of late Triassic (Clarke, 2006) to late Jurassic (Hartley et al., 2005) age. In the earlier segments of the Cenozoic, terrestrial cosmogenic nuclide studies of old geomorphic surfaces suggest the preservation of landforms from the Oligocene/Miocene boundary, which argues for relatively arid conditions since then , with interspersed pluvial episodes occurring ca. 20 Ma, ca. 14 Ma, and ca. 9 Ma (Dunai et al., 2005).

In particular, the climate of the later part of the Cenozoic is of interest in that the climate of the Desert is likely linked, in some manner, to the uplift history of the Andes. There is solid paleosol evidence of hyperarid conditions as early as 13 Ma (Rech et al., 2006). Basin sediments in the northern Desert have been interpreted as suggesting a Pliocene onset of hyperaridity (Hartely and Chong, 2002), while a suite of geomorphic evidence indicates a profound aridification in the southern Atacama Desert in the late Pliocene or early Pleistocene (Amundson et al., 2012).

A challenge for this understanding this region is identifying a long and continuous archive. Here we present data from a buried soil sequence exposed in an open-pit copper mine in fluvial sediments near Calama, in northern Chile. The sediments appear to have been deposited in an unconfined basin, and lateral migration of deposition led to local hiatuses that allowed soil formation. While the geochronology is not precisely constrained, the paleosols likely formed in Oligocene to early Miocene times. Our observations and analyses illuminate the Oligocene-Miocene paleoclimate of the Atacama Desert, and suggest it consisted of periodic oscillations between humid and semi-arid end members, possibly spanning millions of years.

2. Study Location

The study was located in the El Tesoro copper mine (2290 masl), ~60km SSW of the town of Calama (22° 57' S, 69° 5' W; Figure 1) and located along the western flank of the Cordillera de Domeyko. At this exotic-type copper deposit, gravel sediments strike N-S and dip NW at 10-25° (Mora et al., 2004; Tapia et al., 2011). The region experienced considerable uplift/tilting and faulting since Oligocene times. The heads of many Miocene fans are abruptly truncated at ~4000m by the deep escarpment that descends into the present Salar de Atacama; while paleosol and geomorphic considerations indicate that the eastern end of the fans may have been uplifted ~900m since the late Miocene (Rech et al., 2006), with a rotation of 1.3° to the west along the N-S monoclinal axis (Jordan et al., 2010). As a result, the present geographical setting differs substantially from that during the alluvial deposition and soil formation recorded by the paleosols.

The MAP of nearby Calama is ~35mm and MAT is 12^{o} C. Except for stream margins, the region is plant-free. Soils are rich in gypsum/anhydrite in the upper ~1m, and have accumulations of chloride and nitrates at greater depths (Ewing et al., 2006). Presently, carbonate forming environments begin at ~3200 masl (Quade et al., 2007). The surficial geology consists of expansive dissected alluvial fans of Miocene age that have inset Plio-Pleistocene

surfaces. As with much of the Atacama, Quaternary landforms are largely constrained to modern channels and washes, and the landscape surface is dominated by Tertiary deposits.

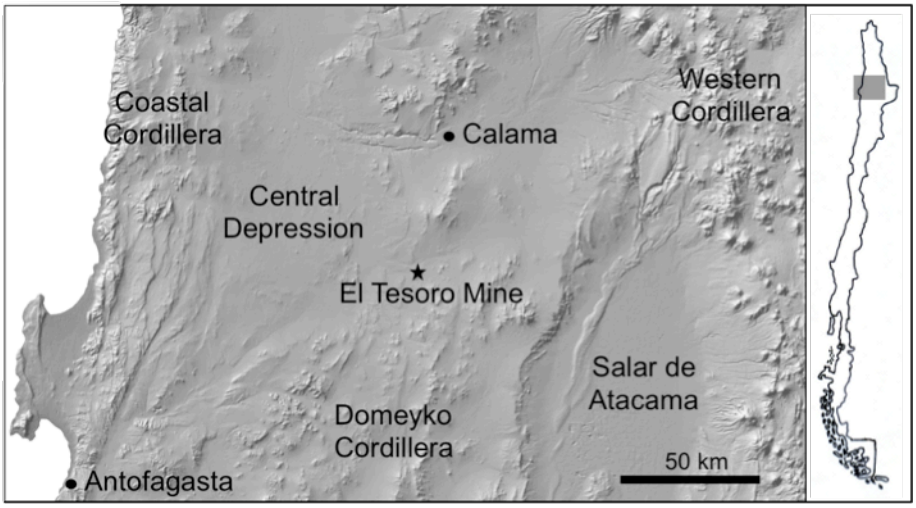

Figure 1. Map of northern Chile with the El Tesoro mine and study location.

3. Methods

3.1 Paleosols

We focused our study in the southern of two open pits at El Tesoro. The entry road into the mine pit was oriented in a sub-perpendicular direction to the sedimentary dip, enabling us to observe several hundred meters of section (uncorrected for dip and measured along the road). The section contained numerous paleosols, each of which is 1 to 3 meters thick, separated by many tens of meters of non-pedogenic gravelly sediments. The paleosols were easily identified by reddening, disruption of sedimentary structure, biological features, and/or distinctive secondary carbonate – all typical of modern soils. The degree of profile development ranged from slightly oxidized zones (representing short durations of exposure), to soil profiles containing well defined horizonation. For the goals of this study – a reconnaissance provided by the mining corporation, only the 22 major soils observed along the exposure were measured, described and logged (several minor weathered zones were noted but not sampled). Of these 22 soils, we sampled in detail a subset of 14 soils. The paleosols were indurated, requiring a hammer and chisel for sample collection. The soils that were selected for sampling were those that had undergone enough vertical development to begin to provide evidence of the existing environmental conditions. Specifically, thickness and clarity of horizons were of particular interest.. Non-pedogenic alluvium overlying each soil was also sampled for comparison to the underlying paleosols. The sampled paleosols were well distributed along the transect and we consider them to be representative of the pedogenic variability along the entire section.

3.2 Laboratory Methods

Bulk samples were disaggregated (some via crushing) before being passed through a 2mm sieve. Munsell soil colors were determined on the dry <2mm fraction and measured for total geochemistry by ALS-Chemex Laboratories in Reno, NV. Geochemical gain and loss analyses of paleosols can augment the interpretation of morphological features. A limitation of this technique in fluvial settings is the large heterogeneity of the lithological/mineralogical

composition of the sediment with space and time. Cerium, neodymium and thorium are relatively abundant in minerals of the continental crust, and show coherent behavior in most sedimentary processes and may thus be less subject to variations in source or physical sorting (Gromet and Silver, 1983). Pairs of elements that are both homogeneously distributed and immobile will show constant ratios throughout a soil profile (Kurtz et al., 2000). In the El Tesoro paleosols, Ce concentrations are well correlated with Nd or Th. While Ce is found in certain environments to respond to redox reactions, the generally mild weathering conditions suggested by the soils, its coherence with Nd and Th, and its relatively high abundance appear to make it suitable as an index element. Thus we used Ce as the index element to examine pedogenesis and the extent of weathering within each paleosol (see discussion below).

Carbonate-bearing fines (<2mm), as well as carbonate coatings on gravels and clasts (sampled by scraping) were analyzed on a GV Isoprime mass spectrometer at Berkeley for carbonate content, as well as $\delta^{13}C$ and $\delta^{18}O$ values after a distilled water rinse through filter paper to remove salts. $\delta^{13}C$ and $\delta^{18}O$ data are reported in delta notation relative to the V-PDB standard for C and O in carbonate, and V-SMOW for waters.

3.3 Geochronology

The age of the sediments broadly constrain the time interval represented by the paleosols. While no directly dateable materials were found in the paleosol sequence, the minimum age of the paleosols is established by a previously reported overlying 10 Ma ignimbrite (^{40}Ar-^{39}Ar on biotite) (Tapia, et al., 2011), as well as a 9.15 (± 0.11) Ma ash (^{40}Ar-^{39}Ar ages by single-crystal, laser-fusion analyses of approximately ten sanidine crystals, analyzed at the Berkeley Geochronology Center) embedded in regional surficial alluvial deposits near the mine (-22° 53' 34.659", -69° 1' 12.896") which was identified and sampled during this study. The maximum age of the sediments and paleosols is constrained by the andesite to dacite intrusive rocks in the basal Eocene sandstone Quebrada Formation, at 37 Ma (Mora et al., 2004). K-Ar ages of supergene cryptomelane mineralization from nearby gravels in the mine are 21.9 Ma (Sernageomin, 2011). Additional supergene mineralization ages have been determined to be 19.2–22.9 Ma in the nearby ore deposits of Telegrafo and Polo Sur by ^{40}Ar-^{39}Ar dating on alunite (Tapia et al., 2011). Thus, the bulk of the samples are younger than 37 Ma, and likely slightly older than 22 Ma, spanning the Oligocene to early Miocene.

The time interval that each paleosol experienced before burial is not essential to detect the signal of climate, but can assist in understanding the rate of sedimentation. It is common in arid settings, if carbonate deposition rates are broadly known, to use the inventory of total carbonate (usually derived from atmospheric deposition) as a guide to duration of exposure. The source of calcium, particularly in semi-arid to arid settings where in situ weathering is minimal, is eolian deposition of calcium bearing dust. In the modern Atacama Desert, depostion has been measured to be 3 ± 2 mmol Ca m^{-2} yr^{-1}, an average of six measurements made at three sites approximately 150 to 500 km south of El Tesoro with a MAP gradient across sites of 2 to 20 mm yr^{-1} (Ewing et al, 2006). These deposition rates, while seemingly appropriate for the Quaternary, may not fully represent early Cenozoic conditions, but fall within that found in arid settings (<1 – 120 mmol Ca m^{-2} yr^{-1}, Reheis et al., 1995).

4. Results and Discussion

The parent material for the paleosols at El Tesoro is comprised of mixed igneous and limestone clasts with typical diameters of 1-7 cm, occasionally up to 35 cm or larger. The mode

of deposition is interpreted to be high-energy stream and sheet flood events, based on the clast-supported matrix, presence of trough cross lamination sedimentary structures and sub-rounded gravel lithomorphology with gravel provenance from the east and east-southeast (Tapia et al., 2011). The paleosols (Figure 2) likely developed as laterally contiguous soils across fan surfaces or low terraces. Each is stratigraphically separated by several meters of non-pedogenic gravels accumulated during regional aggradation. Some of the paleosols were clearly truncated by subsequent stream migration/burial and appear to be missing at least portions of their A (surface) horizons. Only one soil had clear evidence of biological processes: a small animal or root burrow – which in itself is unique in this presently lifeless region. The pedogenic features of the paleosols are well preserved due to minimal overburden pressures and little aqueous diagenesis (discussed more below).

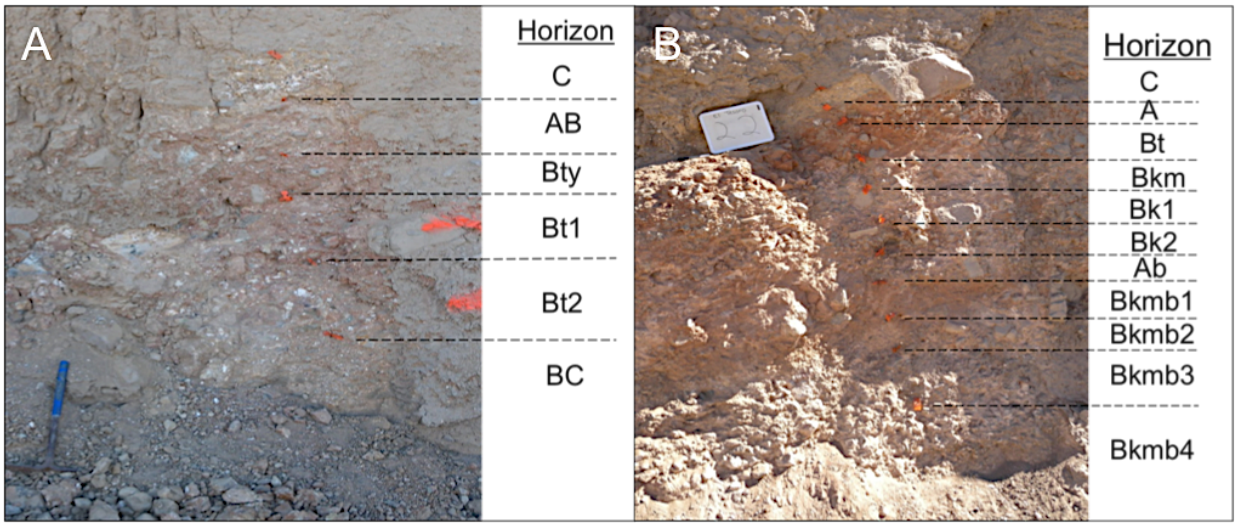

Figure 2. A) Photograph of paleosol #21 (humid-type), note cobbles in clay-rich matrix. B) Photograph of paleosol #22 (arid-type), this is a compound paleosol with the boundary between the two paleosols at the Bk2-Ab interface.

The paleosols can be grouped into several modern soil analogs (Figure 3). Six paleosols (#2, 3a, 10, 14, 20 and 22) are analogous to modern Calciargids (Aridisol soil order; Argillic Calcisols in the Mack et al (1993) paleosol classification). These paleosols had sandy surface horizons that were partly truncated, with weakly developed Bt horizons underneath. The Bt horizons showed evidence of downward translocation of clays with argillans present on gravels and the associated development of soil structural units (blocks). Bk horizons were always present and contained accumulations of pedogenic carbonate varying from rinds on gravel clasts, to moderate cementation of the fine matrix, to massive accumulations >1 m thick. In general, Calciargids are usually soils that have undergone a climate change from a clay-forming environment (subhumid) to a subsequent carbonate-forming environment (arid).

Two Calcids were identified (Calcisols in the Mack system) (#5 and 18), which lack clay-bearing horizons but have relatively strong calcareous horizon development. Such soils are representative of soil formation during a continuous arid period, one lacking enough water to produce secondary clay minerals. Paleosol #17 was analogous to a modern Calcicambid with an

incipient Bt/Bw horizon overlying a series of calcareous Bk horizons. This soil likely has a complex climate history, like the Calciarigids discussed above. Two weakly developed soils (Fluvents) were examined: #7a (sampled) and #4. Pedogenesis in these units was very weak, but yet showed carbonate accumulation that is indicative of arid climate conditions.

These Aridic paleosols clearly formed in a carbonate-accumulating environment. Modern climates that produce Aridisols are found where ET>PT, typically in regions with <60 cm MAP (Schaetzel and Anderson, 2005). However, hyper-arid climates with <20 mm/yr MAP and an absence of biological CO_2 inhibit the formation of soil carbonate (Ewing et al., 2006; Quade et al., 2007). Fine matrix carbonate was found in the B horizons of all of the aridic soils. Carbonate coatings on gravel clasts were also common on the bottoms of clasts, a pedogenic feature reliably found in soils in modern semiarid to arid regions, where carbonate is moved downward with migrating waters, accumulating were evapotranspiration drives calcite supersaturation (Gile et al., 1966; Amundson et al, 1997). The older calcareous paleosols (#2, 3a, 5, 7a) had much higher carbonate contents, and some petrocalcic (carbonate cemented) horizons were present. A critical feature that is critical to our interpretation of these soils is the depth distribution of carbonate. We found that the carbonate bearing paleosols are devoid of carbonate in their upper horizons, but are immediately overlain by carbonate containing sediment. This pattern shows that (1) the profiles were leached of carbonate in their upper horizons before burial, a feature common in deserts like parts of the Mojave (Quade et al., 1989; Wang et al., 1996), and (2) there was no vertical overprinting from calcareous overlying sediments.

Estimates of soil exposure duration times can be calculated from carbonate contents summed over each calcareous paleosol and divided by the eolian Ca dust flux rate of 3 ± 2 mmol Ca m^{-2} yr^{-1} measured in the modern Atacama (Ewing et al, 2006) and are shown in Figure 3. While this simple calculation is open to considerable uncertainties, we use these exposure time estimates only to illustrate that the soil-forming environments may have spanned more than 10 Ma in total. Later in the Miocene, sedimentation nearby seems to have ceased, and thick hyperarid paleosols developed. Rech et al. (2006) estimated that a 6m thick series of calcic and argillic paleosols found in the upper reaches of the Calama Basin approximately 100km to the northeast of El Tesoro formed between 13 and 8 Ma, over the course of 2-5 million years.

$\delta^{13}C$ values from the 12 carbonate-bearing paleosols range from -5.71‰ to 2.70‰ (VPDB) (Figure 3, Table 1). While the C isotope composition of the atmosphere at this time is not precisely known, carbonate values ranging from 4‰ to 5‰ (or 8‰ to 9‰ if diffusional effects are added) would reflect entirely abiotic C. It is clear that the carbonate reflects considerable plant-derived CO_2. None of the paleosols show the typical increase in C isotope values with decreasing depth (c.f. Cerling, 1984). The depth of carbonate-bearing Bk horizons varied from 25cm to more than 100cm (and the absolute loss of overlying A horizons is not well constrained). Thus, it is plausible that all reflect relatively deep soil conditions and depth-invariant paleo-soil CO_2 values. The range in $\delta^{13}C$ values up section of paleosol #9 suggest soil CO_2 $\delta^{13}C$ values of ca. -17‰ to -19‰ indicating modest rates of soil CO_2 production (Cerling, 1984) even in the carbonate forming environment. $\delta^{13}C$ values of carbonate in the lower calcareous paleosols (#7a, 3a, 2) have higher values and variability, suggestive of periods of lower soil respiration and greater aridity than for soils found higher in the stratigraphic section.

The $\delta^{18}O$ values of carbonate ranged from -8.26‰ to -3.16‰ (VPDB) (Figure 3, Table 1). None of the profiles illustrated distinctive depth trends, indicating that the ratio of transpiration/evaporation in terms of soil water loss was relatively high – or that the depth of carbonate formation was below zones of significant evaporative enrichment (e.g. Barnes and

Allison, 1983; 1988). $\delta^{18}O$ values of carbonate in the lower calcareous paleosols (#7a, 3a, 2) have intra-paleosol variability in their $\delta^{18}O$ values that mirrors the C isotope patterns. $\delta^{18}O$ values in the upper part of the section (#14, 17, 20, 22) all shift towards heavier values, trending from an average of -6.28‰ in paleosol #14 to an average of -3.78‰ in #22. This trend in $\delta^{18}O$ values is not reflected in the $\delta^{13}C$ values.

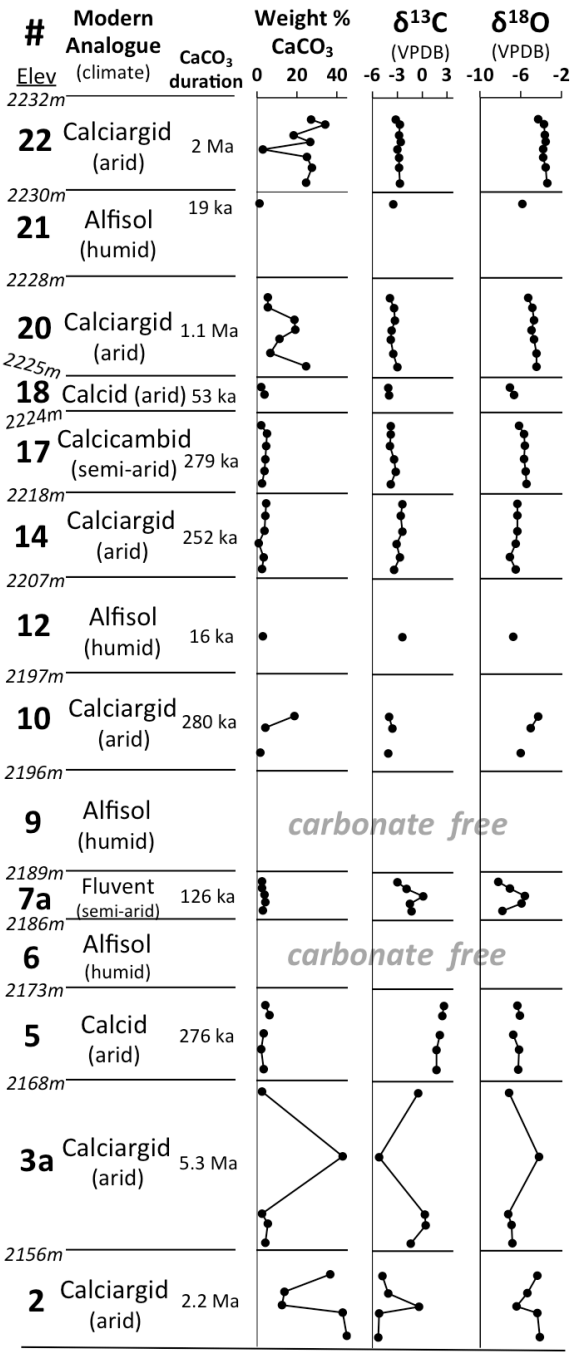

Figure 3. Stratigraphic arrangement of paleosols with carbonate abundance and accumulation

Table 1. Carbonate content, $\delta^{13}C$ and $\delta^{18}O$ values for El Tesoro paleosols

Paleosol	Horizon	Depth (cm)	<2mm Fine Material			Coatings on Clasts	
			% CaCO3	$\delta^{13}C$ (VPDB)	$\delta^{18}O$ (VPDB)	$\delta^{13}C$ (VPDB)	$\delta^{18}O$ (VPDB)
	A	0 - 8	-	-	-	-	-
	Bt	8 - 29	-	-	-	-	-
22a	Bkm	29 - 44	27.1	-3.14	-4.31	-2.32	-3.54
	Bk1	44 - 62	33.9	-2.67	-3.72	-2.08	-3.24
	Bk2	62 - 78	18.1	-2.80	-3.65	-2.53	-3.16
	Ab	78 - 90	26.7	-2.54	-3.60	-2.51	-3.78
	Bkmb1	90 - 108	3.0	-3.03	-3.82	-2.98	-3.77
22b	Bkmb2	108 - 124	24.7	-2.80	-3.80	-2.75	-3.60
	Bkmb3	124 - 152	27.5	-2.75	-3.56	-2.48	-3.70
	Bkmb4	152 - 190	24.3	-2.68	-3.46	-2.71	-3.76
	AB	0 - 32	1.1	-3.49	-5.83	-	-
	Bty	32 - 56	-	-	-	-	-
21	Bt1	56 - 95	-	-	-	-	-
	Bt2	95 - 135	-	-	-	-	-
	BC or C	135 - 180	-	-	-	-	-
	A	0 - 28	-	-	-	-	-
	Bt1	28 - 47	5.4	-3.89	-5.30	-3.84	-4.97
	Bt2	47 - 70	5.5	-3.38	-4.90	-3.04	-4.15
20	Btk	70 - 99	18.8	-3.29	-4.71	-3.50	-4.67
	Bk1	99 - 114	19.1	-3.64	-4.98	-3.60	-5.03
	Bk2	114 - 137	11.2	-3.74	-4.73	-3.38	-4.67
	Bk3	137 - 174	6.4	-3.52	-4.51	-3.45	-4.72
	Bk4	174 - 194	24.4	-2.97	-4.47	-2.79	-4.29
	Bk1	0 - 8	1.9	-4.11	-7.06	-5.71	-13.81
18	Bkm	8 - 31	3.7	-4.03	-6.69	-3.53	-5.16
	Bk'	31 - 47	-	-	-	-4.84	-8.79
	A	0 - 7	-	-	-	-	-
	Bt/Bw	7 - 20	1.9	-3.81	-6.19	-3.56	-5.48
	Bk1	20 - 43	5.1	-3.76	-5.68	-3.50	-5.44
17	Bk2	43 - 71	4.5	-3.84	-5.66	-3.36	-5.33
	Bk3	71 - 99	3.9	-3.43	-5.68	-3.12	-5.23
	Bk4	99 - 122	3.6	-3.21	-5.55	-2.93	-5.50
	Bk5	122 - 151	2.3	-3.83	-5.44	-3.71	-4.90
	A	0 - 14	4.3	-2.34	-6.32	-2.82	-6.40
	Bk1	14 - 51	4.2	-2.56	-6.40	-2.66	-6.57
14	Bk2	51 - 78	3.7	-2.38	-6.34	-	-
	Bk3	78 - 104	0.6	-3.08	-6.51	-2.92	-6.13
	Bk4	104 - 137	3.2	-2.70	-7.05	-2.65	-6.54
	Bk5	137 - 155	2.2	-3.35	-6.52	-3.55	-6.46
	A	0 - 23	-	-	-	-	-
	Bt1	23 - 65	-	-	-	-	-
12	BC	65 - 110	-	-	-	-	-
	C1	110 - 121	2.8	-2.39	-6.73	-2.41	-6.35
	C2	121 - 152	-	-	-	-	-
	C3	152 - 182	-	-	-	-	-

Table 1 (cont'd). Carbonate content, $\delta^{13}C$ and $\delta^{18}O$ values for El Tesoro paleosols

			<2mm Fine Material			Coatings on Clasts	
Paleosol	Horizon	Depth (cm)	% CaCO3	$\delta^{13}C$ (VPDB)	$\delta^{18}O$ (VPDB)	$\delta^{13}C$ (VPDB)	$\delta^{18}O$ (VPDB)
	A	0 - 12	-	-	-	-	-
	Bt	12 - 61	-	-	-	-3.50	-5.36
	Btk	61 - 80	18.7	-3.95	-4.35	-4.08	-4.42
10	Bk1	80 - 110	4.2	-3.54	-5.03	-2.28	-5.05
	Bk2	110 - 136	-	-	-	-	-
	Bk3	136 - 161	1.8	-4.12	-6.01	-1.99	-5.41
	Bk4	161 - 174	-	-	-	-	-
	Bt1	0 - 29	-	-	-	-	-
	Bt2	29 - 83	-	-	-	-	-
9	Btb1	83 - 138	-	-	-	-	-
	Btb2	138 - 173	-	-	-	-	-
	Btb3	173 - 201	-	-	-	-	-
	A	0 - 10	2.4	-3.01	-8.26	-2.34	-7.65
	Bk1	10 - 28	2.6	-1.91	-7.06	-1.42	-6.84
7a	Bk2	28 - 40	3.8	0.14	-5.61	0.19	-5.16
	Bk3	40 - 60	4.2	-1.51	-5.96	-3.03	-4.55
	Bk4	60 - 73	2.9	-1.28	-7.86	0.93	-5.38
	Bt1	0 - 8	-	-	-	-	-
	Bt2	8 - 36	-	-	-	-	-
6	BC	36 - 49	-	-	-	-	-
	C1	49 - 92	-	-	-	-	-
	C2	92 - 122	-	-	-	-	-
	A	0 - 15	-	-	-	-	-
5a	Bk1	15 - 37	4.2	2.62	-6.34	2.55	-6.13
	Bk2	37 - 58	6.0	2.46	-6.14	2.47	-6.23
	Ab	58 - 73	-	-	-	-	-
5b	Bk1	73 - 98	3.4	2.16	-6.73	2.21	-6.67
	Bk2	98 - 141	1.9	1.72	-6.19	2.10	-6.04
	Bk3	141 - 183	3.4	1.78	-6.27	2.70	-6.42
	Bw1	0 - 13	-	-	-	-	-
	Bw2	13 - 40	-	-	-	-	-
	Bw3	40 - 93	2.5	-0.52	-7.17	-0.07	-7.31
3a	Bkm	93 - 313	42.8	-5.20	-4.21	-5.47	-4.13
	Bk1	313 - 336	2.4	0.37	-7.29	0.57	-7.01
	Bk2	336 - 356	5.2	0.42	-6.89	0.39	-7.25
	Bk3	356 - 416	4.2	-1.34	-6.88	0.10	-7.02
	A	0 - 15	-	-	-	-	-
	Bt1	15 - 40	-	-	-	-	-
	2Bkm1	40 - 55	36.5	-4.74	-4.38	-5.38	-4.52
2	2Bkm2	55 - 95	13.8	-4.11	-5.35	-4.61	-4.22
	Bk	95 - 110	12.6	-0.34	-6.46	-0.10	-7.08
	Bkm1'	110 - 125	42.7	-5.19	-4.39	-4.40	-4.83
	Bkm2'	125 - 175	45.0	-5.31	-4.17	-5.40	-4.49

The $\delta^{18}O$ value of pedogenic carbonate is controlled by both the $\delta^{18}O$ value of soil water from which the carbonate formed and the temperature during carbonate formation (Cerling, 1984). Here, we assume a temperature of 25^{o} C and no evaporative enrichment of soil water, based on the lack of depth dependent O isotope profiles in any of the paleosols. Using the relations of Kim and ONeil (1997), the $\delta^{18}O$ values of the soil water that the carbonates formed from ranges from -0.45‰ to -12.03‰, with a mean of -2.92‰ (VSMOW). The $\delta^{18}O$ value of present rainwater in the area and at similar elevations to modern El Tesoro is approximately -5‰ (Aravena, et al., 1999; Rech et al., 2010).

Paleosols #6, 9, 12 and 21 were similar to modern Alfisols (Argillisols in the Mack system), which often display argillic horizons and form in soils of temperate and humid to subhumid climates, such as the Mediterranean region of California. These paleosols have sandy horizons that overlie distinctive Bt horizons consisting of a clay-rich matrix that in some soils formed distinctive blocky structure, and in others surrounded and clay-coated gravel clasts. These accumulations of clay suggest at least modest weathering in a humid/sub-humid environment and subsequent illuviation of weathering products in the soil profile by downward moving water. Additionally, the absence of carbonate in paleosols #6 and 9 indicates rainfall conditions exceeding that of modern carbonate forming environments; a precipitation threshold of approximately 1000 mm/yr precipitation (Jenny, 1941; Retallack, 2005).

Geochemical mass balance analyses reveals two features. First, (as expected) aridic soils have large gains of Ca relative to those interpreted to be more humid (Figure 4). Second, analysis of major element trends (Si, Fe, Na, etc.) reveals no distinctive total or depth differences between the carbonate and non-carbonate soils, indicating that the extent of chemical alteration that the soils experienced was at best modest, and was not large enough to overprint the inherent chemical variability in the sediment (Supplementary Figure1 and Table 1). Additionally, many of the elements mobilized by weathering may have been retained in secondary phyllosilicates and oxides. This observation is likely reflective of both the duration of weathering, and the environmental conditions that impacted the rates of the soil forming conditions at that time.

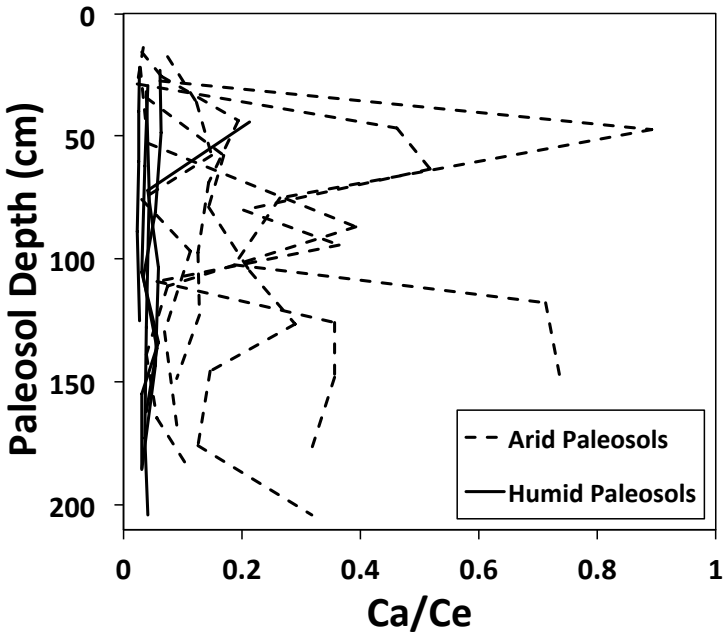

Figure 4. Plot of calcium to cerium ratios for the El Tesoro paleosols

5. Paleoclimate Interpretations and Discussion

The most unambiguous indicator of the climatic conditions when the Tesoro sediments were accumulation is the paleosol morphology: the presence or absence of secondary carbonate. This definitively shows that this region of the Atacama Desert was not hyperarid during the Oligocene and early Miocene. Rech and coworkers (2006) reported argillic and calcic paleosols of early Miocene age (ca. 20 Ma) approximately 100 km to the northeast of El Tesoro in the Calama Basin. These paleosols have montmorillonite and illite clay minerals comprising their argillic horizons, which are indicative of soil forming environments of up to approximately 500 to 1000 mm/yr precipitation (Schaetzel and Anderson, 2005), conditions which are also suggested by the argillic El Tesoro paleosols (#6, 9, 12 and 21). The El Tesoro paleosols, along with these similar Calama Basin paleosols, indicate that conditions wetter than today's prevailed in the Oligocene to early Miocene across a widespread area on the present western flank of the Andes. The El Tesoro paleosols show that the regional climate, at least in the vicinity of Calama, has greatly aridified since the more humid periods of the Oligocene/early Miocene. The zone of climate conditions favorable to pedogenic carbonate accumulation is now found at ~3200 masl (Quade et al, 2007). Estimates of regional uplift during the early and middle Miocene and likely since the sediments were deposited are 2000 m (± 500m) (Farias et al., 2005; Victor et al., 2004; summarized in Jordan et al., 2010) indicate that pluvial conditions existed at elevations as low as 1200 masl.

Globally, the Oligocene and early Miocene were dynamic times climatically as the Earth system cooled from the warm conditions of the early Eocene climatic optimum (Zachos et al., 2001). The Antarctic ice sheet is thought to have started to form during the Oligocene, and by the early Miocene it may have been well developed and extensive (Zachos and Kump, 2005). From a tectonic perspective, the South American continent was fairly close to its present position (Hartley et al., 2005). The Humboldt Current along the western margin of South America was active in this time period after being established in the early Cenozoic (Keller et al., 1997). Various geodynamic scenarios for the Andean Orogeny have been proposed and can be generally framed into two end members: a slow and steady rise beginning as early as the Eocene that results in central Andean elevations of ~2 km during the Miocene (Barnes and Ehlers, 2009), and a rapid rise model that purports a major uplift during the late Miocene resulting in the attainment of current Andean elevations (Garzione et al., 2008).

Oxygen isotopes in paleosol carbonates are widely used in montane environments as a proxy for paleo-elevation and temperature. It is assumed in these studies that the $\delta^{18}O$ value of rainfall follows a simple relationship with elevation: as elevation increases, temperatures cool, and precipitation $\delta^{18}O$ values decline (cf. Blisniuk and Stern, 2005). This strategy has been used in several studies of paleosols and freshwater carbonates on both the eastern and western margins of the Andes in northern Chile and Bolivia (Rech et al., 2010; Garzione et al., 2008; Quade et al., 2007; Garzione et al., 2006). Here, we compile this previous work, and include the El Tesoro carbonates for comparison.

In the Oligocene, it appears that the both the east and western margins of the present Andean plateau had similar $\delta^{18}O$ values, with the west (both El Tesoro and Rech et al., 2010) being slightly more positive (Figure 5). The data also show a sharp divergence of O isotope values over time, with the east becoming more negative, and the western slope (around El Tesoro and Calama) becoming more positive. The trends shown in Fig. 4 for the eastern Andes have been used to support the interpretation of significant late Miocene uplift of the Bolivian Altiplano (Carzione et al., 2006; 2008). The trend of increasing $\delta^{18}O$ values with decreasing age

for the Calama region conflicts with a simple elevation/ $\delta^{18}O$ relationship, especially in light of independent observations of uplift (Jordan et al., 2010; Rech et al., 2006). Rech et al. (2010) interpreted this O isotope data to reflect meteoric water that both decreased due to elevation increases, and suffered subsequent evaporative enrichment that overprinted this decrease. However, Poulsen et al. (2010) have shown, using regional climate model simulations with variable topographic scenarios, that uplift of the Andes may produce complex changes in regional circulation and precipitation $\delta^{18}O$ values during the rise of the Andean plateau, and in the area around Calama precipitation may have moved to *more positive* $\delta^{18}O$ *values* at stages of mid-uplift with the onset of convective storms, and then towards *more negative values* as the present height of the Andes was achieved. Thus, the existing O isotope record may be alternatively interpreted as faithfully recording the O isotope composition of regional precipitation as this section of South America underwent both topographic and climatic reorganization over time. Regardless of the mechanism, there is a clear meteoric water disconnection between the eastern and western Andes over the late Cenozoic, one that likely has its origin in complex circulation changes associated with this topographic change.

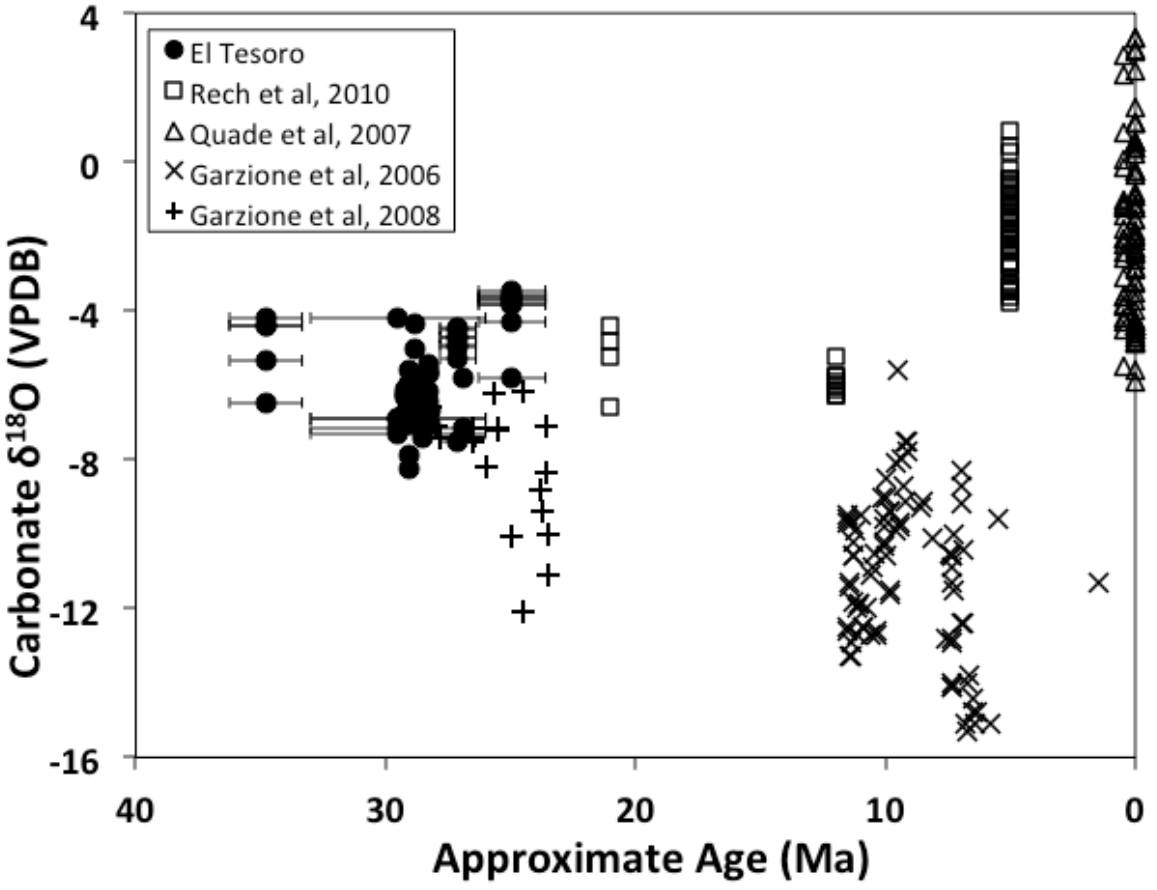

Figure 5. Comparison of El Tesoro carbonate $\delta^{18}O$ values with regional published O isotope data for modern soils, paleosols, and lacustrine and palustrine carbonates on the western side of the Andes near Calama (Rech et al., 2010; Quade et al., 2007) and on the eastern side on the Bolivian altiplano (Garzione et al., 2006; 2008). El Tesoro ages are estimated from carbonate accumulation ages with uncertainties derived from modern carbonate dust flux rates (see text).

6. Conclusions

The El Tesoro paleosols represent a remarkable mid Cenozoic period of oscillations between relatively moist to semi-arid and arid climates, in what is now the driest part of the world. The paleosols, combined with other published studies, indicates that this region underwent significant aridification in the Miocene. The O isotope data from these paleosols, when combined with published data from the region, reveal a significant divergence of the O isotope composition of precipitation in the east and western margins of the Andean plateau since the Oligocene, and suggest that simple assumptions of declines in $\delta^{18}O$ values of carbonate with increasing elevation may not apply where topographic change may induce regional circulation changes. However, this also suggests that there may be a richer record of climate embedded in pedogenic carbonate isotopes, one that will further our understanding of the rise of the Andes.

7. References Cited

Amundson, R., Graham, R.C., Franco-Vizcaino, E., 1997, Orientation of carbonate laminations in gravely saoils along a winetr/summer precipitation gradient in Baja California, Mexico: Soil Science, v. 162, no. 12, p. 940-952.

Amundson, R., Dietrich, W., Bellugi, D., Ewing, S., Nishiizumi, K., Chong, G., Owen, J., Finkel, R., Heimsath, A., Stewart, B., and Caffee, M., 2012, Geomorphologic evidence for the late Pliocene onset of hyperaridity in the Atacama Desert: Geological Society of America Bulletin, v. 124, no. 7-8, p. 1048-1070.

Aravena, R., Suzuki, O., Pena, H., Pollastri, A., Fuenzalida, H., Grilli, A., 1999, Isotopic composition and origin of the precipitation in Northern Chile: Applied Geochemistry, v. 14, no. 4, p. 411-422.

Barnes, C. J., Allison, G. B., 1983, The distribution of deuterium and ^{18}O in dry soils: 1. Theory: Journal of Hydrology, v. 60, no. 1, p. 141-156.

Barnes, C. J., Allison, G. B., 1988, Tracing of water movement in the unsaturated zone using stable isotopes of hydrogen and oxygen: Journal of Hydrology, v. 100, no. 1, p. 143-176.

Barnes, J. B., and Ehlers, T. A., 2009, End member models for Andean Plateau uplift: Earth Science Reviews, v. 97, p. 117-144.

Blisniuk, P. M., and Stern, L. A., 2005, Stable isotope paleoaltimetry: A critical review: American Journal of Science, v. 305, no. 10, p. 1033-1074.

Cerling, T. E., 1984, The stable isotopic composition of modern soil carbonate and its relationship to climate: Earth and Planetary Science Letters, v. 71, no. 2, p. 229-240.

Clarke, J. D. A., 2006, Antiquity of aridity in the Chilean Atacama Desert: Geomorphology, v. 73, p. 101-114.

Dunai, T. J., González López, G. A., and Juez-Larré, J., 2005, Oligocene–Miocene age of aridity in the Atacama Desert revealed by exposure dating of erosion-sensitive landforms: Geology, v. 33, no. 4, p. 321.

Ewing, S., Sutter, B., Owen, J., Nishiizumi, K., Sharp, W., Cliff, S., Perry, K., Dietrich, W., McKay, C., and Amundson, R., 2006, A threshold in soil formation at Earth's arid–hyperarid transition: Geochimica et Cosmochimica Acta, v. 70, no. 21, p. 5293-5322.

Farías, M., Charrier, R., Comte, D., Martinod, J., Hérail, G., 2005, Late Cenozoic deformation and uplift of the western flank of the Altiplano: Evidence from the depositional, tectonic, and geomorphologic evolution and shallow seismic activity (northern Chile at 19 30′ S): Tectonics, v. 24, no.4.

Garzione, C. N., Hoke, G. D., Libarkin, J. C., Withers, S., MacFadden, B., Eiler, J., Ghosh, P., and Mulch, A., 2008, Rise of the Andes: Science, v. 320, no. 5881, p. 1304-1307.
Garzione, C. N., Molnar, P., Libarkin, J. C., and MacFadden, B. J., 2006, Rapid late Miocene rise of the Bolivian Altiplano: Evidence for removal of mantle lithosphere: Earth and Planetary Science Letters, v. 241, no. 3–4, p. 543-556.
Gile, L. H., Peterson, F. F., Grossman, R. B., 1966, Morphological and genetic sequences of carbonate accumulation in desert soils: Soil Science, v. 101, no.5, p.347-360.
Gromet, L. P., and Silver, L. T., 1983, Rare earth element distributions among minerals in a granodiorite and their petrogenetic implications: Geochimica et Cosmochimica Acta, v. 47, p. 925-939.
Hartley, A. J., and Chong, G., 2002, Late Pliocene age for the Atacama Desert: Implications for the desertification of western South America: Geology, v. 30, no. 1, p. 43.
Hartley, A. J., Chong, G., Houston, J., and Mather, A. E., 2005, 150 million years of climatic stability: evidence from the Atacama Desert, northern Chile: Journal of the Geological Society, v. 162, no. 3, p. 421-424.
Jenny, H., 1941, Factors of Soil Formation: McGraw-Hill, New York.
Jordan, T. E., Nester, P. L., Blanco, N., Hoke, G. D., Dávila, F., and Tomlinson, A. J., 2010, Uplift of the Altiplano-Puna plateau: A view from the west: Tectonics, v. 29, no. 5, p. TC5007.
Keller, G., Adatte, T., Hollis, C., Ordonez, M., Zambrabo, I., Jimenez, N., Stinnesbeck, W., Aleman, A., and Hale-Erlich, W., 1997, The Cretaceous/Tertiary boundary event in Ecuador: Reduced biotic effects due to eastern boundary current setting: Marine Micropaleontology, v. 31, p. 97-133.
Kim, S. T., and O'Neil, J. R., 1997, Equilibrium and nonequilibrium oxygen isotope effects in synthetic carbonates: Geochimica et Cosmochimica Acta, v. 61, no. 16, p. 3461-3475.
Kurtz, A. C., Derry, L. A., Chadwick, O. A., and Alfano, M. J., 2000, Refractory element mobility in volcanic soils: Geology, v. 28, no. 8, p. 683-686.
Mack, G. H., James, W. C., and Monger, H. C., 1993, Classification of paleosols: Geological Society of America Bulletin, v. 105, no. 2, p. 129-136.
Mora, R., Artal, J., Brockway, H., Martinez, E., and Muhr, R., 2004, El Tesoro Exotic Copper Deposit, Antofagasta Region, Northern Chile: Society of Economic Geologists, no. Special Publication 11, p. 187-197.
Poulsen, C. J., Ehlers, T. A., and Insel, N., 2010, Onset of convective rainfall during gradual late Miocene rise of the Central Andes: Science, v. 328, p. 490-493.
Quade, J., Cerling, T. E., Bowman, J. R., 1989, Systematic variations in the carbon and oxygen isotopic composition of pedogenic carbonate along elevation transects in the southern Great Basin, United States: Geological Society of America Bulletin, v. 101, no. 4, p. 464-475.
Quade, J., Rech, J. A., C., L., Betancourt, J. L., Gleeson, E., and Kalin, M. T. K., 2007, Soils at the hyperarid margin: The isotopic composition of soil carbonate from the Atacama Desert, Northern Chile: Geochimica et Cosmochimica Acta, v. 71, p. 3772-3795.
Rech, J. A., Currie, B. S., Michalski, G., and Cowan, A. M., 2006, Neogene climate change and uplift in the Atacama Desert, Chile: Geology, v. 34, no. 9, p. 761-764.
Rech, J. A., Currie, B. S., Shullenberger, E. D., Dunagan, S. P., Jordan, T. E., Blanco, N., Tomlinson, A. J., Rowe, H. D., and Houston, J., 2010, Evidence for the development of

the Andean rain shadow from a Neogene isotopic record in the Atacama Desert, Chile Earth and Planetary Science Letters, v. 292, p. 371-382.
Reheis, M. C., Goodmacher, J. C., Harden, J. W., McFadden, L. D., Rockwell, T. K., Shroba, R. R., Taylor, E. M., 1995, Quaternary soils and dust deposition in southern Nevada and California: Geological Society of America Bulletin, v. 107, no. 9, p. 1003-1022.
Retallack, G. J., 2005, Pedogenic carbonate proxies for amount and seasonality of precipitation in paleosols: Geology, v. 33, no. 4, p. 333-336.
Schaetzel, R. and Anderson, S., 2005, Soils: genesis and geomorphology: Cambridge University Press, New York, 817 p.
Sernageomin, 2011, Informe de datacion radiometrica K-Ar Numero 32/2011, Servicio Nacional de Geologia y Minera, Subdireccion Nacionalde Geologia, Departmento de Laboratorios, Chile.
Tapia, M., Riquelme, R., Campos, E., Marquardt, C., Mpodozis, C., Mora, R., and Munchmeyer, C., 2011, Cenozoic exotic Cu mineralization in the Centinela District (Atacama Desert, Northern Chile), Society for Geology Applied to Mineral Deposits, 11th Biennial Meeting: Antofagasta. Chile.
Victor, P., Oncken, O., Glodny, J., 2004, Uplift of the western Altiplano plateau: Evidence from the Precordillera between 20 and 21 S (northern Chile): Tectonics, v. 23, no. 4.
Wang, Y., McDonald, E., Amundson, R., McFadden, L., Chadwick, O., 1996, An isotopic study of soils in chronological sequences of alluvial deposits, Providence Mountains, California: Geological Society of America Bulletin, v. 108, no.4, p. 379-391.
Zachos, J., Pagani, M., Sloan, L., Thomas, E., and Billups, K., 2001, Trends, rhythms, and aberrations in global climate 65 Ma to present: Science, v. 292, no. 5517, p. 686-693.
Zachos, J. C., and Kump, L., 2005, Carbon cycle feedbacks and the initiation of Antarctic glaciation during the earliest Oligocene: Global and Planetary Change, v. 47, p. 51-66.

Chapter 4:
Oxygen Isotope Fractionation Effects in Soil Water via Interaction with Cations (Mg, Ca, K, Na) Adsorbed to Phyllosilicate Clay Minerals

1. Introduction

In isotope-based approaches to hydrology, soil and sediment have been implicitly considered to be an inert matrix through which water passes. Yet, this assumption is inconsistent with the fact that soils contain a wide range of solutes and highly variable concentrations of chemically reactive clay particles (Sposito, 2008), all of which may react with bulk water to create regions of water molecules with different coordination environments and varying isotope compositions.

Previous researchers have postulated the existence of various "pools" of water with differing oxygen isotope compositions in soils (Ingraham and Shadel, 1992; Araguas-Araguas, et al., 1995, Hsieh, et al., 1998), but it has only been recently that a growing body of evidence has emerged supporting this hypothesis (c.f. Brooks et al., 2010; Soderberg et al., 2012). The mechanisms for the formation and retention, as well as the locations, of these pools remains largely unexplored, particularly in light of both macro- and molecular-scale considerations of soil mineralogy and physical chemistry.

Soil solutions commonly have high solid to fluid ratios in a matrix of minerals with diverse structures and electrical charges. Based on molecular scale modeling of the organization of water molecules at and near electronegatively charged particle surfaces (Bourg and Sposito, 2011), we anticipate that isotope effects should be produced and be experimentally observable, especially at lower water contents where the ratio between the isotopically "perturbed" water is high relative to free water. The magnitude of these effects should be most evident in soils with high cation exchange capacity (CEC) combined with specific cations adsorbed to the clay particles. Here we conduct laboratory experiments to explore the potential existence of such isotope effects as a first step in a more detailed consideration of the role of stable isotopes in mineral-water interactions.

2. Background

2.1 Ionic Solutions

Water that passes through soils physically interacts with an array of solutes, as well as with solids (here, we consider colloidal suspensions as part of the water-solid interaction). The effects of solutes on oxygen isotopes have a long history of study in stable isotope geochemistry (Feder and Taube 1952; Taube 1954; Sofer and Gat 1972, 1975). In general, oxygen isotope fractionation in aqueous saline solutions varies with dissolved cation concentration, and the sign and magnitude of the effect is cation-specific, largely correlating with the "ionic potential" (charge/ionic radius) of the ion in solution and its corresponding polar coordination with water molecules resulting in the formation of hydration spheres around each cation (O'Neil and Truesdell, 1991). The isotopes of oxygen in the water molecules associated with hydration spheres around dissolved ions can be either enriched or depleted in the heavy oxygen isotopes of water, with a corresponding effect on the bulk water. This is the so-called salinity effect.

The most favorable theory explaining the fractionation of water oxygen isotopes by cations in solution is based on the notion of cations with a high ionic potential (e.g. Mg^{2+}, Ca^{2+} herein) creating a more structured organization of water molecules around each cation, as compared to the bulk water. Conversely, cations with lower ionic potential (e.g. K^{+}) disrupt the water structure around them. Frank and Wen (1957) first observed these macroscopic effects and discussed the structure-making and structure-breaking effects of electrolytes in aqueous solution. More recent studies have both confirmed the effects of cations on the structure of water (Marcus, 2010) and cast doubt on its molecular-scale underpinnings (Turton et al., 2011). This uncertainty does not preclude the use of the structure making and breaking concept to describe the macroscale behavior of water oxygen isotopes in saline solutions. We adopt the operational definition of O'Neil and Truesdell (1991), who articulated that from an oxygen isotope perspective, structure makers have the effect of depleting the bulk water in ^{18}O, while structure breakers yield bulk water with an enriched ^{18}O composition. They justify this definition with the observation of positive isotopic fractionation between ice (highly structured) and liquid water (O'Neil, 1968), and negative isotopic fractionation between vapor (no structure) and liquid water (Majoube, 1971). These simple cases are analogous to water in hydration spheres around cations because these water isotopologues are sequestered away from the bulk water in a similar sense to how they would be in ice crystals.

While the specific molecular-scale mechanism(s) for the reorganization of oxygen isotopes around cations in solution remain uncertain, the prevailing theory (i.e. O'Neil and Truesdell, 1991) is that structure making cations (Mg^{2+}, Ca^{2+}) create organized water by forming two hydration regions around the cation. In the inner sphere, water molecules are strongly bound by the cation's ionic charge and are structured with their dipoles oriented radially to the cation by an intense electrostatic attraction. The more diffuse outer region is where water molecules are hydrogen bonded to each other and more weakly bound to the cation. The inner, strongly bonded region preferentially incorporates $H_2{}^{18}O$ with its shorter intramolecular bonds, while the outer, hydrogen bonded region concentrates $H_2{}^{16}O$. It is the net balance of the effects of these hydration regions that determines the characteristic cation-specific fractionation effect, with the inner sphere dominating the net effect of the divalent Mg^{2+} and Ca^{2+} ions. In contrast, water structure breaking ions with lower ionic potential (K^{+}) create a single hydration region of water molecules that are organized by hydrogen bonding. This region of hydrogen-bonded water appears to preferentially incorporate $H_2{}^{16}O$ molecules, thereby enriching the bulk water outside of the hydration region in $H_2{}^{18}O$.

In the special case of Na^{+}, which does not exhibit net oxygen-fractionating effects, there seem to be two potential mechanisms for the lack of fractionation: if Na^{+} creates two hydration spheres around itself, they appear to have largely mutually cancelling effects (Phillips and Bentley, 1987), or that Na^{+} creates a region of very mild hydrogen bonded water that does not exert a strong enough influence on the bulk water surrounding it to be observable (Nag et al, 2008). In either mechanistic case, a macroscopic oxygen isotope effect is not seen for Na^{+} in aqueous solution.

2.2 Clay Mineral Interactions with Water

Soil is largely a heterogeneous mixture of silicate minerals. The sand (0.05 to 2 mm) and silt (0.002 to 0.05 mm) fractions tend to be dominated by primary silicates of low

surface area to mass ratios and have a negligible electrostatic charge. In contrast, the clay fraction (<0.002 mm) is commonly dominated by secondary phyllosilicates with high surface area to mass ratios and a considerable permanent negative charge. This negative charge gives rise to a mineral's cation exchange capacity (CEC), a measure of how many cations (typically Ca^{2+}, Mg^{2+}, K^{+}, Na^{+}) from the surrounding soil solution adsorb to the mineral surface to balance its negative structural charge (Schoonheydt and Johnson, 2013). The most common reactive mineral group within the phyllosilicates (clays) is the smectites, and montmorillonite is a common smectite. These cations adsorbed to clay particles attract water in the form of hydrations spheres, and infrared spectroscopic studies of Mg- and Ca-montmorillonite reveal that the properties of the surrounding water are distinct from the bulk water and strongly influenced by the identify of the adsorbed cation (Burgess, 1978; Johnston et al., 1992; Xu et al., 2000).

A comprehensive body of research exists on the effects of clays on water isotope fractionation at higher temperatures and pore water pressures than are found in soils. This work that is intended to emulate underground settings such as confined aquifers and geothermal reservoirs and has concluded that diffusive gradients concentrate the heavy isotopic species behind clay membranes, irrespective of cation identity and ionic potential (e.g. Coplen and Hanshaw, 1973; Phillips and Bentley, 1987; Hu and Clayton, 2003). These results differ markedly from observations of oxygen isotope fraction at ambient pressures which are the conditions found in soils and we therefore interpret these high temperature and pressure oxygen isotope effects to be due to mechanisms and processes not present in soils.

Given the large and predictable ionic-water isotope interactions described above, it follows that a more in depth investigation of oxygen isotope fractionation from water-solid interactions is warranted. These water-solid interaction processes likely manifest themselves in nature, particularly in soils with high salt contents, or more generally in any soil with a significant proportion of charged clay minerals (e.g. Vertisols, soils with at least 40% expandable clay and associated high CEC).

In this paper, we examine the effect of monominerallic homoionic smectite-water mixtures on the oxygen isotope composition of soil water measureable by CO_2 exchange. This research tests the assumption that soil is essentially an inert matrix for infiltrating water. Our hypothesis is that cations adsorbed to the clay surface form isotopically organized hydration spheres of water around them and thereby sequester these water molecules away from the bulk water. In turn, this has possible implications for interpretations of the O isotope composition of plant waters and pedogenic carbonates, and their relationship to meteoric water.

3. Methods

To study the effects of soil on oxygen isotope fractionation of water, we used Arizona montmorillonite sourced from near Cameron, Arizona (API clay #49-5107) with a CEC of 60.75 $cmol_c/kg$ and Texas montmorillonite sourced from near Gonzalez, Texas (Source Clay STX1-b) with a CEC of 69.5 $cmol_c/kg$ (both measured by Ba-replacement at the University of California, Davis Analytical Laboratory).

Two stocks of Arizona montmorillonite mineral powder were combined with monoionic cation-chloride aqueous solutions of $MgCl_2$, $CaCl_2$, and KCl at either 0.05M or 1M concentrations, mixed by hand and allowed to equilibrate and gravitationally settle

overnight, after which the supernatant saline solutions were manually decanted. Three saline washes at either 0.05M or 1M were followed in a similar manner with three deionized water rinses at circumneutral pH. The mineral-water slurries were dried at 70°C, yielding dry homoionic montmorillonite powders with all available surface adsorption sites occupied by Mg^{2+}, Ca^{2+} or K^{+} cations. Iota® quartz sand was similarly prepared as a control. While quartz does have a very small (but measurable) CEC due to unsatisfied hydroxyl bonds at mineral cleavage surfaces, it should have almost no ability to adsorb cations and therefore any observable isotope effect should be minimal, if present at all. These samples are referred to herein as "stir and settle" homoionic and were designed to determine if an adsorbed cation isotope effect was present and detectable. Additionally, these experiments test if the effect is still present when smectite clays are exposed to even weakly saline solutions, and therefore simulate saltwater inundated soils in coastal and estuarine settings.

To more precisely constrain and quantify the adsorbed cation isotope effect, a third stock of clay was prepared using the "acidic washing" method. Texas montmorillonite (Source Clay STx1-b) was employed when our supply of Arizona montmorillonite was exhausted and was prepared by washing the mineral powder with acidic (adjusted to pH 3 with HCl) monoionic cation-chloride aqueous solutions ($MgCl_2$, $CaCl_2$, NaCl, KCl) at 1M concentration multiple times (each separated by centrifugation to allow the supernatant to be completely decanted), followed by multiple rinses with acidified 0.01M saline solution, ethanol rinses to remove chloride anions and residual H^{+} cations, and oven drying at 70°C. By preparing this smectite material with acidic electrolyte washes in this way, any weathering products that may have been present on the clay surfaces composed mainly of amorphous Al oxyhydroxide materials (proto-boehmite and gibbsite) that are found ubiquitously in soils are dissolved away from the mineral surfaces and removed (Sposito, 2008).

From each of these homoionic smectite materials, sets of mineral-water mixtures were created in autosampler-specific sample vials with butyl rubber septum caps from homoionic dry mineral powder and deionized water of known isotopic composition at 5% to 32% gravimetric water content (Tables 1 and 2), the same range of soil water proportions that are commonly observed in nature (n = 1 replicate per material for "stir and settle" preparation, 3-4 replicates per material for "acidic washing"). Each mineral-water mixture was prepared with the mineral mass scaled to 0.05g (50µL) water, thereby reducing size effects in IRMS analyses. The choice of this small amount of water is necessitated by the relatively large volume of clay powder required to make gravimetric mixtures at 5% water - 95% clay: 0.95 g clay with ~2mL clay volume in a 12mL vial is the largest amount of clay that allows for the autosampler needle to be reliably separated from contact with the clay-water mixture. Water volumes of 50µL still have three orders of magnitude more moles of H_2O for oxygen isotopic equilibration with CO_2 headspace (2.78×10^{-3} mol H_2O : 7.98×10^{-6} mol CO_2 for driest samples), though do require longer equilibration times. Measured $\delta^{18}O$ values on 50µL pure water samples maintain accuracy and precision similar to samples with larger water volume regularly analyzed on this instrument. Quartz-water mixtures also yield reliable $\delta^{18}O$ values with 50µL water volumes (discussed below).

Sample vial headspace was purged with 0.2% CO_2 in He and allowed to equilibrate in the vial at room temperature for ca. 5 days (Epstein and Mayeda 1953) and analysis was subsequently conducted for $\delta^{18}O$ values on a Thermo Delta V mass spectrometer with Thermo Gas Bench II interface (Center for Stable Isotope Biogeochemistry, UC Berkeley). Analyses were started with three injections of tank reference CO_2 to evaluate instrument stability and calculate $\delta^{18}O$ values. Sample gas is injected five times and $\delta^{18}O$ values are calculated on the average of the last four peak heights. Analytical runs include three lab standard reference waters with well constrained $\delta^{18}O$ (VSMOW) values every 6th sample allowing calibration to the VSMOW scale. Long-term external precision on this instrument is ±0.12‰ for $\delta^{18}O$ of water.

Oxygen isotope $\delta^{18}O$ values are defined and presented in standard notation:

$$\delta = \left(\frac{R_{sample}}{R_{standard}} - 1\right) \times 1000 \quad (1)$$

where R_{sample} and $R_{standard}$ are the $^{18}O/^{16}O$ ratios for the sample and standard, respectively. All $\delta^{18}O$ data are reported in per mil (‰) relative to VSMOW. The difference between the measured $\delta^{18}O$ values of the homoionic mineral-water mixtures (δ_m) and that of the deionized water used to make the mixtures (δ_0) is calculated as in Sofer and Gat (1972):

$$\Delta\delta^{18}O = \frac{(\delta_0 - \delta_m)}{(1000 + \delta_m)} \times 1000 \quad (2)$$

$\Delta\delta^{18}O$ values are somewhat counter intuitive because they are opposite the sign of the observed isotope effect. $\Delta\delta^{18}O$ values are correction factors and are added to the measured $\delta^{18}O$ values to correct for the isotope effect. Positive $\Delta\delta^{18}O$ values mean that the measured $\delta^{18}O$ values are depleted in ^{18}O relative to the input water, and negative $\Delta\delta^{18}O$ values mean that the measured $\delta^{18}O$ values are enriched in ^{18}O relative to the input water.

4. Experimental Results

With respect to the Arizona montmorillonite prepared with the "stir and settle" homionic washes (n = 1), Mg-montmorillonite shows the largest isotope effect with $\Delta\delta^{18}O$ values of 3.36‰ at 8% water to 0.90‰ at 32% water when prepared with 1.0M $MgCl_2$ washing solution, and 3.14‰ at 8% water to 0.54‰ at 32% water when prepared with 0.05M $MgCl_2$ washing solution (Table 1 and Figure 1A). Ca-montmorillonite shows $\Delta\delta^{18}O$ values of 2.40‰ at 8% water to 0.84‰ at 32% water when prepared with 1.0M $CaCl_2$ washing solution, and 3.37‰ at 8% water to 0.81‰ at 32% water when prepared with 0.05M $CaCl_2$ washing solution.

Quartz shows a negligible isotope effect with very small $\Delta\delta^{18}O$ values that are likely due to limits in analytical precision for the continuous flow IRMS instrument, as well as subtle evaporative effects due to the high surface area to volume ratio of the water in the thin capillary film of water surrounding each quartz grain. This is as expected, given the near complete absence of a structural charge on which to adsorb cations.

Experiments with the "stir and settle" homoionic preparation method show a larger isotope effect than the homoionic samples prepared with acidic washing and

centrifugation, and therefore may be complicated by the incomplete removal of residual salts from the electrolyte cation-loading solutions. Even with this additional complication, these samples demonstrate the efficacy of cation loading solution concentrations equivalent to those found in nature (seawater [Mg] = 0.05M) and these soil analogs are similar to soil or sediment samples found in the field, i.e. clay-rich soils in semiarid climates or within coastline or estuarine settings that have been inundated by saline or brackish waters.

Table 1. Data for mineral-water mixtures prepared with neutral pH "stir and settle" homoionic preparation. The values for the last three columns were determined as discussed in the text. The pure water used to prepare these mixtures had $\delta^{18}O$ of -12.33‰ (VSMOW).

Cation Electrolyte	Mineral	Mineral mass (g)	% H_2O (g/g)	$\delta^{18}O$ (VSMOW)	$\Delta\delta^{18}O$	Repartitioned cation molarity in added H_2O	$\Delta\delta^{18}O$ due to repartitioned cations in added H_2O	% $\Delta\delta^{18}O$ due to repartitioned cations in added H_2O
$MgCl_2$ [1.0 M]	montmorillonite	0.580	7.9	-15.63	3.36	0.104	0.116	3.5
		0.265	15.9	-14.00	1.70	0.048	0.053	3.1
		0.108	31.7	-13.21	0.90	0.019	0.022	2.4
$MgCl_2$ [0.05 M]	montmorillonite	0.575	8.0	-15.42	3.14	0.103	0.115	3.7
		0.265	15.9	-13.71	1.40	0.048	0.053	3.8
		0.106	32.0	-12.86	0.54	0.019	0.021	3.9
$CaCl_2$ [1.0 M]	montmorillonite	0.576	8.0	-14.70	2.40	0.143	0.067	2.8
		0.265	15.9	-13.72	1.41	0.066	0.031	2.2
		0.106	32.2	-13.16	0.84	0.026	0.012	1.5
$CaCl_2$ [0.05 M]	montmorillonite	0.578	8.0	-15.64	3.37	0.143	0.067	2.0
		0.264	15.9	-14.34	2.04	0.065	0.031	1.5
		0.111	31.1	-13.13	0.81	0.028	0.013	1.6
$MgCl_2$ [1.0 M]	quartz	0.577	8.0	-12.38	0.05	–	–	–
		0.264	15.9	-12.24	-0.09	–	–	–
		0.107	31.8	-12.31	-0.02	–	–	–
$MgCl_2$ [0.05 M]	quartz	0.579	7.9	-12.09	-0.24	–	–	–
		0.264	15.9	-12.23	-0.10	–	–	–
		0.109	31.5	-12.13	-0.20	–	–	–
$CaCl_2$ [1.0 M]	quartz	0.574	8.0	-12.06	-0.27	–	–	–
		0.262	16.0	-12.18	-0.16	–	–	–
		0.105	32.2	-12.08	-0.25	–	–	–
$CaCl_2$ [0.05 M]	quartz	0.576	8.0	-12.23	-0.10	–	–	–
		0.262	16.0	-12.07	-0.26	–	–	–
		0.106	32.1	-11.94	-0.39	–	–	–

$\Delta\delta^{18}O$ values for mineral-water mixtures composed of Texas montmorillonite prepared with the acidic homoionic washing are shown in Table 2 and Figure 1B. Mg-montmorillonite shows the largest isotope effect with $\Delta\delta^{18}O$ values from 0.96‰ to 1.55‰ (Ave = 1.20‰, S.D. = 0.31, n = 3) at 5% water content to $\Delta\delta^{18}O$ values of 0.49‰ to 0.70‰ (Ave = 0.60‰, S.D. = 0.11, n = 3) at 30% water. Ca-montmorillonite had an isotope effect nearly as large as Mg, with $\Delta\delta^{18}O$ values from 0.74‰ to 1.01‰ (Ave = 0.92‰, S.D. = 0.15, n = 3) at 5% water content to $\Delta\delta^{18}O$ values from 0.33‰ to 0.39‰ (Ave = 0.35‰, S.D. = 0.03, n = 3) at 30% water. K-montmorillonite shows $\Delta\delta^{18}O$ values from -0.51‰ to -0.86‰ (Ave = -0.69‰, S.D. = 0.17, n = 3) at 5% water content to $\Delta\delta^{18}O$ values of -0.11‰

to -0.27‰ (Ave = -0.21‰, S.D. = 0.08, n = 3) at 30% water. Na-montmorillonite shows $\Delta\delta^{18}O$ values from 0.01‰ to -0.24‰ (Ave = -0.09‰, S.D. = 0.12, n = 4) at 5% water content to -0.03‰ to -0.16‰ (Ave = -0.10‰, S.D. = 0.06, n = 3) at 30% water.

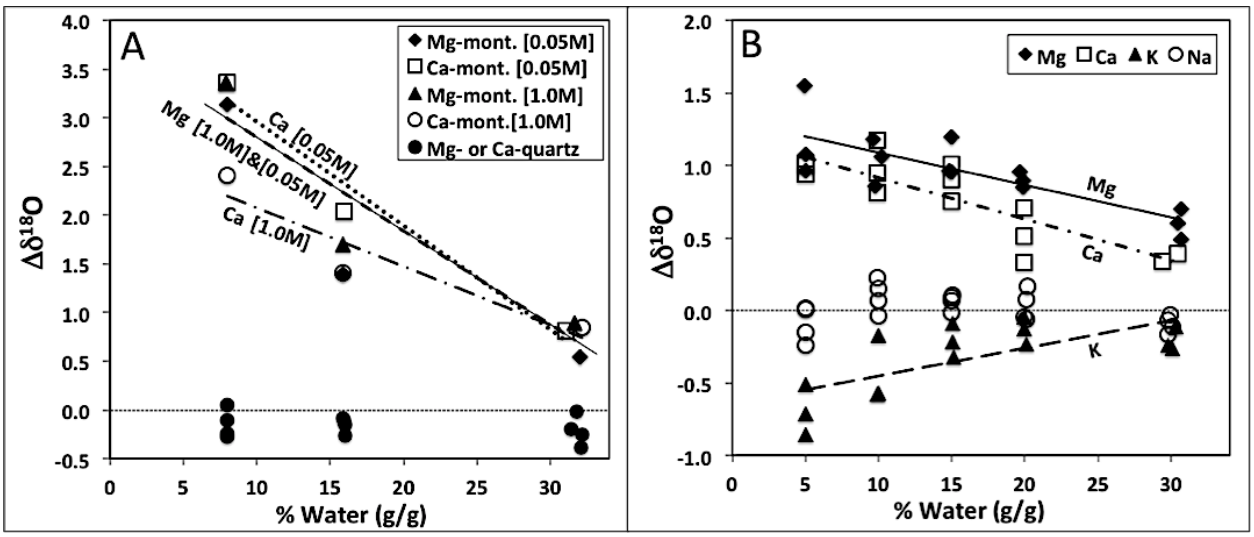

Figure 1. The relationship of $\Delta\delta^{18}O$ to gravimetric water content for **A**: Mg- and Ca-montmorillonite-water mixtures prepared with the "stir and settle" washing method with varying cation concentration, and **B**: Mg-, Ca-, K-, Na-montmorillonite-water mixtures prepared with the acidic washing method.

5. Discussion

These experiments affirm the fact that smectite minerals are not an isotopically inert medium for water. Pure water that is exposed to homoionic smectite will undergo reactions with the solid phase that ultimately changes the stable isotope composition of the more energetically free water that remains. The reactions are clearly impacted by the concentration and valence of the adsorbed cation phases, and also likely reflect additional, but poorly understood, effects of water-mineral interactions.

When pure water is added to the homoionic smectite, two processes occur simultaneously. First, a portion of the exchangeable cations on the clay surfaces hydrate and reconfigure into the inner- and outer-sphere complexes of the electrical double layer as well as some portion of cations that become fully solvated and in go into solution where they exert the isotope effects previously discussed as the 'salinity effect'. Second, those cations that remain in the inner- and outer-sphere complexes in close proximity to clay surfaces and are not fully solvated, form hydration spheres around them and exert a different fractionation effect on the bulk water, see Figure 2 for a conceptual depiction of this process. The $\Delta\delta^{18}O$ values measured on mineral-water mixtures are a combination of these two effects and their respective contributions to the net observed effect. Separating out the magnitude of each component's contribution to the net isotope effect can yield information on the nature of the adsorbed cation effect.

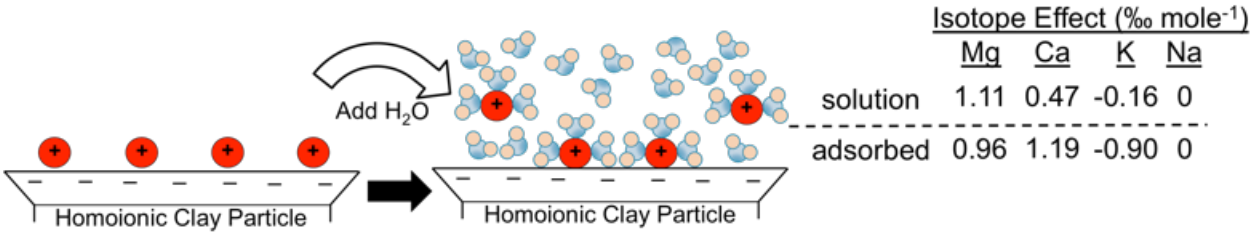

Figure 2. Conceptual depiction of cation repartitioning when homoionic clay is exposed to liquid water and the corresponding isotope effect attributable to each component. Solution data from Sofer and Gat (1972), adsorbed data this study.

Following equilibration with pure water, the concentration of cations desorbed from the clay and now in solution is calculated by multiplying the initial quantity of cations adsorbed on the clay by the partition coefficient (K_D): $K_D = A/C$, where A is the amount of cations adsorbed on the clay and C is the amount of cations in solution. K_D values available in the literature for base cations in clay soils are shown in Table 3 (Baes and Sharp, 1983). K_D values for Na are unavailable and so an estimated value of 9 mL/g is used, based on the value for K and its relative similarity in ionic properties to Na. To express K_D values as a dimensionless ratio (K_D^*), K_D (mL/g) is multiplied by the density of montmorillonite (2.5 g/cm^3) (Appelo and Postma, 1999). The molarity of the equilibrated water in each mineral-water mixture after cation repartitioning is shown in Tables 1 and 2, and calculated as follows.

The concentration of adsorbed cations per unit mass of dry homoionic montmorillonite can be determined by reasoning that every available charge site to adsorb a cation is occupied after the homoionic clay preparation. For monovalent cations this amount is simply the measured CEC of the mineral (Arizona Montmorillonite: 60.8 cmol$_c$/kg; Texas montmorillonite: 69.5 cmol$_c$/kg), and for divalent cations it is half this number, as each divalent cation balances two structural charge sites. The total amount of cation adsorbed to clay particles in a gravimetric sample is then easily determined by multiplying the CEC by the mass of mineral.

The portion of the observed $\Delta\delta^{18}O$ values that are attributable to the isotope salinity effect, which is due to the fractionation of water molecules into hydration spheres around fully solvated cations compared to the pure water used to make the solutions, can be determined by multiplying the equilibrated solution molarity by the salinity effect per molality unit as characterized by Sofer and Gat (1972): 1.11‰ for Mg^{2+}, 0.47‰ for Ca^{2+}, 0‰ for Na^+, -0.16‰ for K^+. The component of $\Delta\delta^{18}O$ values for each mineral-water mixture that is directly attributable to the salinity effect of repartitioned cations into the aqueous phase is shown in Tables 1 and 2.

The magnitude of the isotope effect due to adsorbed cations can be determined by subtracting the salinity effect component from the observed $\Delta\delta^{18}O$ value. In general, the salinity effect exerted by cations in solution are on the order of 7% to 22% of the total observed for the driest mineral-water mixtures (5% water), and are less than 10% of the observed $\Delta\delta^{18}O$ values for wetter samples with 8% or more water. The balance of the isotope effect and observed $\Delta\delta^{18}O$ values is therefore attributable either solely to that

Table 2. Data for Texas montmorillonite mineral-water mixtures prepared with acidic homoionic preparation. The values for the last three columns were determined as discussed in the text. The pure water used to prepare these mixtures had $\delta^{18}O$ of -11.74‰ (VSMOW).

Cation	Mineral mass (g)	% H_2O (g/g)	$\delta^{18}O$ measured (VSMOW)	$\Delta\delta^{18}O$	Repartitioned cation molarity into added H_2O	$\Delta\delta^{18}O$ due to repartitioned cations into added H_2O	% $\Delta\delta^{18}O$ due to repartitioned cations into added H_2O
	0.960	5.0	-13.27	1.55	0.198	0.219	14.1
	0.940	5.1	-12.69	0.96	0.194	0.215	22.3
	0.950	5.0	-12.80	1.08	0.196	0.217	20.2
	0.470	9.6	-12.90	1.18	0.097	0.107	12.5
	0.440	10.2	-12.78	1.06	0.091	0.101	9.1
	0.460	9.8	-12.59	0.86	0.095	0.105	9.2
	0.283	15.0	-12.92	1.19	0.058	0.065	4.6
Mg^{2+}	0.287	14.8	-12.69	0.97	0.059	0.066	4.6
	0.284	15.0	-12.68	0.96	0.058	0.065	3.8
	0.204	19.7	-12.68	0.95	0.042	0.047	3.4
	0.201	19.9	-12.58	0.85	0.041	0.046	3.0
	0.201	19.9	-12.62	0.89	0.041	0.046	2.7
	0.113	30.7	-12.22	0.49	0.023	0.026	2.6
	0.113	30.7	-12.43	0.70	0.023	0.026	3.8
	0.114	30.5	-12.34	0.60	0.023	0.026	2.7
	0.953	5.0	-12.47	0.74	0.196	0.092	17.2
	0.951	5.0	-12.74	1.01	0.196	0.092	12.5
	0.952	5.0	-12.73	1.00	0.196	0.092	12.7
	0.452	10.0	-12.67	0.94	0.093	0.044	6.4
	0.454	9.9	-12.68	0.95	0.093	0.044	6.4
	0.455	9.9	-12.90	1.17	0.094	0.044	5.2
	0.284	15.0	-12.54	0.81	0.058	0.027	4.7
Ca2+	0.283	15.0	-12.63	0.90	0.058	0.027	4.2
	0.283	15.0	-12.73	1.00	0.058	0.027	3.8
	0.200	20.0	-12.48	0.75	0.041	0.019	3.5
	0.200	20.0	-12.24	0.51	0.041	0.019	5.2
	0.200	20.0	-12.44	0.71	0.041	0.019	3.8
	0.120	29.4	-12.07	0.33	0.025	0.012	4.8
	0.114	30.5	-12.07	0.34	0.023	0.011	4.5
	0.117	29.9	-12.12	0.39	0.024	0.011	4.0

Table 2. (cont'd) Data for Texas montmorillonite mineral-water mixtures prepared with acidic homoionic preparation. The values for the last three columns were determined as discussed in the text. The pure water used to prepare these mixtures had $\delta^{18}O$ of -11.74‰ (VSMOW).

Cation	Mineral mass (g)	% H_2O (g/g)	$\delta^{18}O$ measured (VSMOW)	$\Delta\delta^{18}O$	Repartitioned cation molarity into added H_2O	$\Delta\delta^{18}O$ due to repartitioned cations into added H_2O	% $\Delta\delta^{18}O$ due to repartitioned cations into added H_2O
K+	0.949	5.0	-10.89	-0.86	0.391	-0.063	7.3
	0.947	5.0	-11.03	-0.71	0.390	-0.062	8.8
	0.947	5.0	-11.23	-0.51	0.390	-0.062	12.1
	0.453	9.9	-11.17	-0.58	0.187	-0.030	5.2
	0.449	10.0	-11.57	-0.17	0.185	-0.030	17.1
	0.449	10.0	-11.18	-0.57	0.185	-0.030	5.2
	0.281	15.1	-11.42	-0.32	0.116	-0.019	5.8
	0.282	15.1	-11.65	-0.09	0.116	-0.019	20.7
	0.282	15.1	-11.52	-0.22	0.116	-0.019	8.4
	0.199	20.1	-11.51	-0.23	0.082	-0.013	5.7
	0.200	20.0	-11.70	-0.04	0.082	-0.013	31.8
	0.200	20.0	-11.62	-0.13	0.082	-0.013	10.5
	0.118	29.8	-11.51	-0.24	0.049	-0.008	3.3
	0.116	30.1	-11.48	-0.27	0.048	-0.008	2.9
	0.115	30.3	-11.63	-0.11	0.047	-0.008	6.7
Na+	0.951	5.0	-11.60	-0.15	0.392	0	0
	0.950	5.0	-11.50	-0.24	0.391	0	0
	0.950	5.0	-11.75	0.01	0.391	0	0
	0.950	5.0	-11.74	0.01	0.391	0	0
	0.452	10.0	-11.96	0.23	0.186	0	0
	0.451	10.0	-11.70	-0.04	0.186	0	0
	0.450	10.0	-11.89	0.15	0.185	0	0
	0.451	10.0	-11.80	0.06	0.186	0	0
	0.283	15.0	-11.81	0.07	0.117	0	0
	0.282	15.1	-11.84	0.10	0.116	0	0
	0.284	15.0	-11.83	0.09	0.117	0	0
	0.284	15.0	-11.73	-0.01	0.117	0	0
	0.198	20.2	-11.90	0.16	0.082	0	0
	0.199	20.1	-11.82	0.08	0.082	0	0
	0.199	20.1	-11.68	-0.06	0.082	0	0
	0.200	20.0	-11.70	-0.04	0.082	0	0
	0.118	29.8	-11.67	-0.07	0.049	0	0
	0.118	29.8	-11.58	-0.16	0.049	0	0
	0.117	29.9	-11.71	-0.03	0.048	0	0
	0.116	30.1	-11.63	-0.12	0.048	0	0

exerted by adsorbed cations on the bulk water or by a combination of the adsorbed cations and some other factor(s), such as reactions with the mineral surface itself.

Considering the mass balance of water added to the mineral-water mixtures can help elucidate the observed trend of increasing adsorbed cation effect with decreasing water content. The total amount of water molecules coordinated in hydration spheres around cations adsorbed to clay surfaces can be found by multiplying the number of water molecules per hydration sphere ("hydration number" in Table 3; Ohtaki and Radnai, 1993) by the CEC of the mineral (assuming adsorbed cations have the same coordination arrangement when adsorbed compared to in solution). For the case of Mg exchanged Texas montmorillonite, this is 6 x 69.5 meq/100g = 417 mmol/100g. This quantity of coordinated water is then multiplied by molar mass of water (18g/mol) and converted into mol from mmol, yielding 7.506g water per 100g clay, or 7.5% water content. Above this threshold, the increasing proportion of bulk to adsorbed water will diminish the influence of the adsorbed cation effect.

Table 3. Ionic properties for materials used in this study. Hydration numbers from Ohtaki and Radnai (1993).

				Adsorbed Cation Molarity (mol/kg)	
Cation	Hydration #	K_D (mL/g)	K_D^*	AZ montmorillonite	TX montmorillonite
Mg^{2+}	6	13.5	33.75	0.30375	0.3475
Ca^{2+}	6	9.8	24.5	0.30375	0.3475
K^+	4	9	22.5	0.6075	0.695
Na^+	4	9	22.5	0.6075	0.695

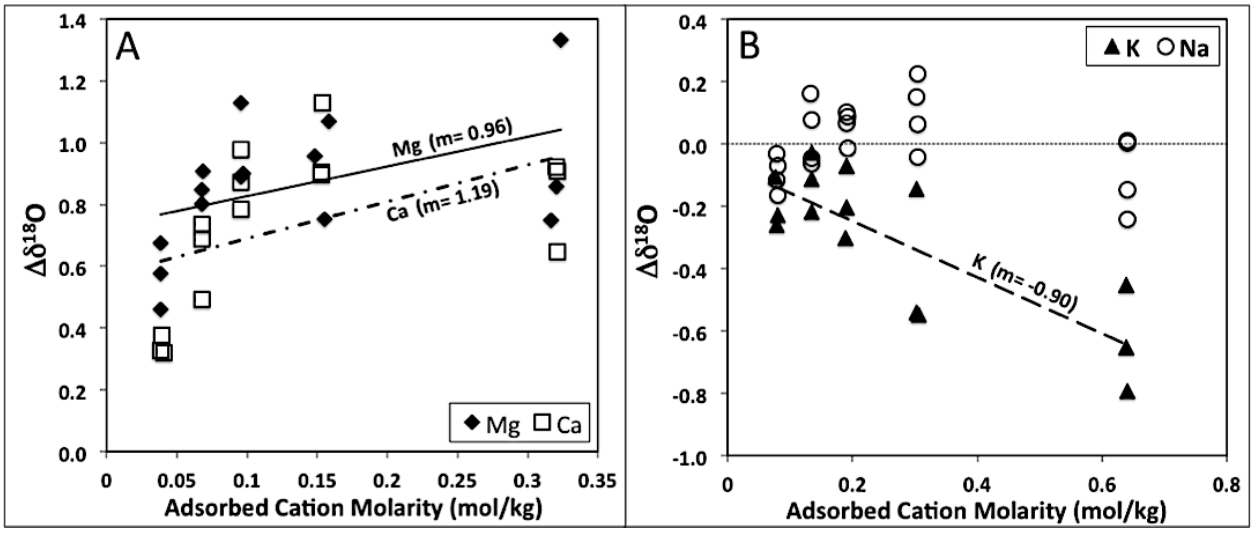

Figure 3. The relationship of $\Delta\delta^{18}O$ to the concentration of adsorbed cation concentration for **A**: Mg- and Ca-montmorillonite-water mixtures prepared by the acidic homoionic washing method and **B**: K- and Na-montmorillonite-water mixtures prepared by the acidic homoionic washing method.

Table 4. Measured isotope values and fraction factors per unit mole. All δ units are ‰ per mole of cation desorbed in solution (aq) or adsorbed to mineral surfaces (ad)

Cation	δ_{aq}	δ_{ad}	$1000\ln\propto$
Mg^{2+}	1.11	0.96	0.15
Ca^{2+}	0.47	1.19	-0.72
K^{+}	-0.16	-0.9	0.74
Na^{+}	0	0	0

Though it is somewhat approximate, the relationship of the adsorbed isotope effect component to the concentration of cations remaining adsorbed (in a net equilibration sense) to the clay particles in the mineral-water mixtures (which is, analogous to adsorbed cation molarity), is 0.96‰ per mole of adsorbed cation for Mg^{2+}, 1.19‰ for Ca^{2+} and -0.9‰ for K^{+} (Table 4). Not surprisingly, and similar to its behavior in solution, Na^{+} does not show an isotopic effect when adsorbed to smectite surfaces (Figures 3A and 3B).

The effects of Mg, both adsorbed and in solution, are relatively similar on a per mole basis. However, Ca shows a twice-greater effect when adsorbed, as compared to in solution, and is comparable to that of Mg. Xu et al. (2000), using infrared spectroscopy, found that as the water content of Mg- and Ca-montmorillonite decreases to <10 water molecules per exchangeable cation (~12.5% water for Texas montmorillonite in this study), the water molecules are clustered around the adsorbed cation and are restricted in their ability to form hydrogen bonds with the surrounding bulk water, a condition that would seem to favor water structure making and the attendant isotopic effects. Interestingly, both Mg- and Ca-montmorillonite behaved in a similar manner in the study of Xu et al. (2000), suggesting that once the clay surface is saturated by adsorbed cations, divalent base cations regardless of identity exert a similar effect on the structure of water. This may explain why the adsorbed cation isotope effects for Mg and Ca seen in this study are similar to each other in magnitude.

Somewhat surprisingly, K shows an effect more than 5 times greater when it is adsorbed compared to when in solution (Figure 3B: -0.9‰ $mole^{-1}$ for adsorbed K, Figure 1B: -0.16‰ $mole^{-1}$ for K in solution). This disproportionate effect suggests that there is likely another mechanism present that enhances the inclusion of isotopically light water in the vicinity of K-montmorillonite surfaces, thereby enriching the bulk water in $H_2{}^{18}O$. That is, the net effect of the structure-breaking cation seems to be enhanced. An aspect of the K^{+} ion that may be relevant is that its ionic size allows it to fit into the open crystal structure of phyllosilicate mineral sheets (Sposito, 2008). This ability to create a relatively "satisfied" surface both electrically and texturally may enhance the ability of the surface to create regions of hydrogen bonded water near to it, as discussed below.

The isotopic fractionation factor per unit mole between water surrounding desorbed cations in solution and water associated with adsorbed cations on clay surfaces can be calculated from the per mole δ values by the relationship:

$$\alpha_{aq\text{-}ad} = (1000 + \delta_{aq}) / (1000 + \delta_{ad}) \qquad (3)$$

where δ_{aq} and δ_{ad} are the molar components of the measured δ values as described above. Fractionation factors for the cations in this study are listed in Table 4, and expressed as $1000\ln\propto$ for utility.

There is some evidence that smectite surfaces themselves may exert an isotope effect on water by creating a very thin film of structurally broken water at the mineral surface. Bourg and Sposito (2011) conducted molecular dynamics simulations of the organization of water near smectite surfaces and found several regions with a higher density of water molecules in the electrical double layer at the mineral-water interface. Immediately adjacent to the clay (2.7 Å from surface), the density of water molecules in the first statistical water monolayer is more than three times larger than that in the bulk water, and that these molecules are hydrogen bonded to surface O atoms. In the region of the second statistical water monolayer (6.4 Å), water molecule density is between 1 and 3 times that of the bulk water. Their calculations reveal that diffusion of both water molecules and ions within these high water density regions is rapid enough to indicate that this water is not rigidly structured in an "ice-like" manner (Bourg and Sposito, 2011). The presence of regions of hydrogen bonded water and the lack of rigid structure in the vicinity of smectite surfaces seem to indicate that there is the potential for water isotope fractionation between this high water density region and the bulk water in a manner akin to that observed in aqueous solutions of structure breaking cations like K^+. The effects associated with smectite surfaces may be present in the interlayer space between phyllosilicate crystal structures and may be contributing to the macroscopic isotope effect that is observed in the bulk water. Moreover, the effects of the smectite clay surface may enhance the magnitude of the isotopic effects of the structure breaking cations when adsorbed to smectite surfaces.

Beyond these fundamental physical interactions there are practical implications of our observed effects on the use of stable isotopes in terrestrial ecosystem hydrology. First, the analytical method chosen to assess soil water oxygen isotope composition must be considered in view of the intended "pools" of soil water to be measured. Direct equilibration, used here, clearly measures a portion of soil water that is free for equilibration with CO_2, in contrast to water extracted by various methods which reflect the total soil water isotope composition. While direct equilibration of CO_2 with in situ soil water will not reflect the total soil water composition, it may in turn be a more reliable guide to the composition of water that is biologically available or reactive in mineral precipitation (such as calcite). Additionally, a spatial distribution of various pools of soil water may be analytically accessible through the use of the screening effect that the limited CO_2 diffusive path length in various soil water environments presents. The use of direct equilibration techniques has greatly increased in recent years for laboratory IRMS (e.g. Scrimgeour, 1995; Hsieh et al, 1998; Ignatev et al., 2013) and IRIS analyses (Wassenaar et al., 2008), as well as in field analyses (Breecker et al., 2008; Herbstritt et al, 2012, Rothfuss et al, 2013).

An especially vigorous area of research in ecohydrological science revolves around investigations into plant water use and its spatiotemporal variability. These approaches generally rely on variation in the isotopic profile of soil water as a function of depth in the soil horizon, which occurs when dry conditions drive soil surface evaporation (Barnes and Allison, 1988; Braud et al., 2009). These dry conditions are where we observe the greatest adsorbed cation fractionation effect. Research on plant water use utilizing both oxygen and hydrogen isotopes has recently demonstrated the possibility of two distinct soil water

pools: a more mobile pool of water that resembles the precipitation and stream water associated with the local meteoric water line, as well as a second and less mobile pool of water that is consistent with plant water use (Brooks et al., 2010; Goldsmith et al., 2012). The adsorbed cation isotope effect presented here may be relevant to the isotopic composition of plant available water in soils with some component of high-CEC clay and when soil water conditions are drying. Our experimental results combined with observations of aberrant soil water isotope signatures in field soils (Orlowski et al., 2013; Meißner et al., 2014) suggests that soil mineralogy may warrant greater consideration in isotopic studies of soil and plant water.

The results here are also relevant to interpreting the stable isotope composition of secondary, pedogenic carbonate in paleosols. Clay-rich soils (Vertisols, soils with a minimum of 40% expandable clay) are found on outcrops of clay rich rock or sediment, coastal or estuarine environments, basin deposits, or outcrops of shale or mudstone (Soil Survey Staff, 1999). Additionally, outcrops of basalt or ultramafic rock commonly weather, especially in semiarid settings, into clay rich Vertisols. Fossil Vertisols (buried clay-rich soils) are especially prominent in the geological record since they form at the distal ends of large subsiding basins. Additionally, these fossil soils are commonly rich in pedogenic carbonate ($CaCO_3$), and thus are similar to the Ca-rich smectite experiments in Table 2 and Figure 1B. It appears that the water recorded by the oxygen isotopes in carbonate forming in equilibrium with soil water may be about 1 per mil more depleted than that which would be recorded by carbonate forming in equilibrium with the meteoric waters that entered the soil, since pedogenic carbonate minerals precipitate when soils are at their driest (Breecker et al., 2009), soil moisture contents analogous to <15% in Figure 1B. While the net effect is likely modest, it may have significance in certain paleo-interpretations.

The biggest impact of these findings may be on the evolving efforts to use the O isotope composition of atmospheric CO_2 to serve as a probe of gross primary production and ecosystem exchange (e.g. Werner et al., 2012). One of the most complex parameters in these efforts is the net effect of soil respiration and abiotic exchange with the atmosphere (Stern et al., 2001). The additional issue of meteoric water reactions with soil minerals and salts adds yet an additional challenge for this approach, and even a few per mil shift in the soil water value on a global scale, has enormous impacts on global estimates of GPP (Stern et al., 2001; Yakir and Sternberg, 2000). The influence of soil on the $\delta^{18}O$ composition of the atmosphere has been investigated by analytic and numeric modeling studies, and one conclusion of this work is that some component of the atmospheric oxygen isotope composition is determined by the global-scale direct equilibration of atmospheric CO_2 with soil water (Tans, 1998; Stern et al., 1999).

As mentioned, soils that may be especially reactive in an oxygen isotope sense with atmospheric CO_2 are Vertisols, which are rich (>30%) in fine-grained, smectite clays and undergo intense shrink/swell behavior with desiccation cracks opening during the drying season to depths greater than 50 cm (Soil Survey Staff, 2010). These cracks increase the area of the soil-atmosphere interface, promoting isotopic exchange between soil water and the atmosphere. This enhanced atmospheric perfusion to considerable depths, coupled with the occurrence of Vertisols across 2.4% of Earth's surface (Dudal and Eswaran, 1988), suggests that adsorbed cation isotope effects on the $\delta^{18}O$ composition of the atmosphere may warrant further investigation.

6. Conclusions

We show that cations adsorbed to high-CEC clay mineral particles can create isotopically distinct "pools" of water that may not readily mix with each other or the bulk water in the soil solution. The measured $\delta^{18}O$ values of soil water in the vicinity of high-CEC clay minerals may therefore only be reflecting a portion of the total soil water. Investigations of oxygen isotope dynamics in soil water are of interest to a variety of disciplines ranging from soil science to stable isotope ecology to the study of global biogeochemical fluxes. Our ability to observe and accurately predict the role of clay mineralogy on soil water oxygen isotopes is a critical step towards the eventual evaluation of this isotope effect in natural soils and for incorporating the effect in biophysical applications.

7. References

Appelo, C.A.J., Postma, D., 1999. Geochemistry, groundwater and pollution. Taylor & Francis, 536 pp.

Araguas-Araguas, L., Rozanski, K., Gonfiantini, R., Louvat, D., 1995. Isotope effects accompanying vacuum extraction of soil water for stable isotope analyses. Journal of Hydrology, 168: 159-171.

Baes, C., Sharp, R., 1983. A proposal for estimation of soil leaching and leaching constants for use in assessment models. Journal of Environmental Quality, 12(1): 17-28.

Barnes, C.J., Allison, G.B., 1988. Tracing of Water-Movement in the Unsaturated Zone Using Stable Isotopes of Hydrogen and Oxygen. Journal of Hydrology, 100(1-3): 143-176.

Bourg, I.C., Sposito, G., 2011. Molecular dynamics simulations of the electrical double layer on smectite surfaces contacting concentrated mixed electrolyte ($NaCl–CaCl_2$) solutions. Journal of Colloid and Interface Science, 360(2): 701-715.

Braud, I., Biron, P., Bariac, T., Richard, P., Canale, L., Gaudet, J., and Vauclin, M., 2009. Isotopic composition of bare soil evaporated water vapor. Part I: RUBIC IV experimental setup and results. J Hydrol, 369(1): 1-16.

Breecker, D., Sharp, Z.D., 2008. A field and laboratory method for monitoring the concentration and isotopic composition of soil CO_2. Rapid Communications in Mass Spectrometry, 22(4): 449-454.

Breecker, D.O., Sharp, Z.D., McFadden, L.D., 2009. Seasonal bias in the formation and stable isotopic composition of pedogenic carbonate in modem soils from central New Mexico, USA. Geological Society of America Bulletin, 121(3-4): 630-640.

Brooks, J.R., Barnard, H.R., Coulombe, R., McDonnell, J.J., 2010. Ecohydrologic separation of water between trees and streams in a Mediterranean climate. Nature Geoscience, 3(2): 100-104.

Burgess, J., 1978. Metal ions in solution. Ellis Horwood Chichester, 481 pp.

Coplen, T.B., Hanshaw, B.B., 1973. Ultrafiltration by a compacted clay membrane—I. Oxygen and hydrogen isotopic fractionation. Geochimica et Cosmochimica Acta, 37(10): 2295-2310.

Dudal, R., Eswaran, H., 1988. Distribution, properties and classification of Vertisols. Publication Soil Management Support Services, US Department of Agriculture, Natural Resources Conservation Service, Washington DC: 1-22.

Epstein, S., Mayeda, T., 1953. Variation of ^{18}O content of waters from natural sources. Geochimica et Cosmochimica Acta, 4(5): 213-224.
Feder, H.M., Taube, H., 1952. Ionic hydration: an isotopic fractionation technique. The Journal of Chemical Physics, 20(8): 1335-1336.
Frank, H.S., Wen, W.Y., 1957. Ion-solvent interaction. Structural aspects of ion-solvent interaction in aqueous solutions: a suggested picture of water structure. Discussions of the Faraday Society, 24: 133-140.
Goldsmith, G.R. et al., 2012. Stable isotopes reveal linkages among ecohydrological processes in a seasonally dry tropical montane cloud forest. Ecohydrology, 5(6): 779-790.
Herbstritt, B., Gralher, B., Weiler, M., 2012. Continuous in situ measurements of stable isotopes in liquid water. Water Resources Research, 48(3).
Hsieh, J.C.C., Savin, S.M., Kelly, E.F., Chadwick, O.A., 1998. Measurement of soil-water delta ^{18}O values by direct equilibration with CO_2. Geoderma, 82(1-3): 255-268.
Hu, G., Clayton, R.N., 2003. Oxygen isotope salt effects at high pressure and high temperature and the calibration of oxygen isotope geothermometers. Geochimica et Cosmochimica Acta, 67(17): 3227-3246.
Ignatev, A., Velivetckaia, T., Sugimoto, A., Ueta, A., 2013. A soil water distillation technique using He-purging for stable isotope analysis. Journal of Hydrology. 498: 465-473.
Ingraham, N.L., Shadel, C., 1992. A comparison of the toluene distillation and vacuum/heat methods for extracting soil water for stable isotopic analysis. Journal of Hydrology, 140: 371-387.
Johnston, C., Sposito, G., Erickson, C., 1992. Vibrational probe studies of water interactions with montmorillonite. Clays and Clay Minerals, 40(6): 722-730.
Majoube, M., 1971. Fractionnement en oxygene-18 et en deuterium entre l'eau et sa vapeur. J. Chim. phys, 68(10): 1423-1436.
Marcus, Y., 2010. Effect of ions on the structure of water. Pure and Applied Chemistry, 82(10): 1889-1899.
Meißner, M., Köhler, M., Schwendenmann, L., Hölscher, D., Dyckmans, J., 2014. Soil water uptake by trees using water stable isotopes (δ^2H and $\delta^{18}O$)– a method test regarding soil moisture, texture and carbonate. Plant and Soil, 376(1-2): 327-335.
Nag, A., Chakraborty, D., Chandra, A., 2008. Effects of ion concentration on the hydrogen bonded structure of water in the vicinity of ions in aqueous NaCl solutions. Journal of Chemical Sciences, 120(1): 71-77.
Ohtaki, H., Radnai, T., 1993. Structure and dynamics of hydrated ions. Chemical Reviews, 93(3): 1157-1204.
O'Neil, J.R., 1968. Hydrogen and oxygen isotope fractionation between ice and water. The Journal of Physical Chemistry, 72(10): 3683-3684.
O'Neil, J.R., Truesdell, A.H., 1991. Oxygen isotope fractionation studies of solute-water interactions. Stable isotope geochemistry: A tribute to Samuel Epstein(3): 17.
Orlowski, N., Frede, H., Brüggemann, N., Breuer, L., 2013. Validation and application of a cryogenic vacuum extraction system for soil and plant water extraction for isotope analysis. Journal of Sensors and Sensor Systems, 2: 179-193.
Phillips, F.M., Bentley, H.W., 1987. Isotopic fractionation during ion filtration: I. Theory. Geochimica et Cosmochimica Acta, 51(3): 683-695.
Rothfuss, Y., Vereecken, H., Brüggemann, N., 2013. Monitoring water stable isotopic

composition in soils using gas-permeable tubing and infrared laser absorption spectroscopy. Water Resources Research, 49: 3747-3755.
Schoonheydt, R.A., Johnston, C.T., 2013. Surface and Interface Chemistry of Clay Minerals. In: Faïza, B., Gerhard, L. (Eds.), Developments in Clay Science. Elsevier, pp. 139-172.
Scrimgeour, C.M., 1995. Measurement of plant and soil water isotope composition by direct equilibration methods. Journal of Hydrology, 172: 264-274.
Soderberg, K., Good, S.P., Wang, L., Caylor, K., 2012. Stable isotopes of water vapor in the vadose zone: A review of measurement and modeling techniques. Vadose Zone Journal, 11(3).
Sofer, Z., Gat, J., 1975. The isotope composition of evaporating brines: effect of the isotopic activity ratio in saline solutions. Earth and Planetary Science Letters, 26(2): 179-186.
Sofer, Z., Gat, J.R., 1972. Activities and Concentrations of ^{18}O in Concentrated Aqueous Salt Solutions - Analytical and Geophysical Implications. Earth and Planetary Science Letters, 15(3): 232-238.
Soil Survey Staff, 1999. Soil taxonomy: a basic system of soil classification for making and interpreting soil surveys. Natural Resources Conservation Service, United States Department of Agriculture.
Soil Survey Staff, 2010. Keys to Soil Taxonomy. United States Department of Agriculture, Natural Resources Conservation Service.
Sposito, G., 2008. The Chemistry of Soils. Oxford University Press, 329 pp.
Stern, L., Baisden, W.T., Amundson, R., 1999. Processes controlling the oxygen isotope ratio of soil CO_2: Analytic and numerical modeling. Geochimica et Cosmochimica Acta, 63(6): 799-814.
Stern, L.A., Amundson, R., Baisden, W.T., 2001. Influence of soils on oxygen isotope ratio of atmospheric CO2. Global Biogeochem Cycles, 15(3): 753-759.
Tans, P.P., 1998. Oxygen isotopic equilibrium between carbon dioxide and water in soils. Tellus B, 50(2): 163-178.
Taube, H., 1954. Use of oxygen isotope effects in study of hydration of ions. The Journal of Physical Chemistry, 58(7): 523-528.
Turton, D. A., Hunger, J., Stoppa, A., Thoman, A., Candelaresi, M., Hefter, G., Walther, M., Buchner, R., and Wynne, K., 2011. Rattling the cage: Micro-to mesoscopic structure in liquids as simple as argon and as complicated as water. Journal of Molecular Liquids, 159(1): 2-8.
Wassenaar, L.I., Hendry, M.J., Chostner, V.L., Lis, G.P., 2008. High Resolution Pore Water ^{2}H and^{18}O Measurements by H_2O((liquid))-H_2O((vapor)) Equilibration Laser Spectroscopy. Environ Science and Technology, 42(24): 9262-9267.
Werner, C. et al., 2012. Progress and challenges in using stable isotopes to trace plant carbon and water relations across scales. Biogeosciences, 9: 3083-3111.
Xu, W., Johnston, C.T., Parker, P., Agnew, S.F., 2000. Infrared study of water sorption on Na-, Li-, Ca-, and Mg-exchanged (SWy-1 and SAz-1) montmorillonite. Clays and Clay Minerals, 48(1): 120-131.
Yakir, D., Sternberg, L., 2000. The use of stable isotopes to study ecosystem gas exchange. Oecologia, 123(3): 297-311.

Appendices: Supplementary Figures and Data Tables

Appendix 1: Chapter 1, Supplementary Figures and Data Tables

Supplementary Table 1. Soil CO_2 $\delta^{13}C$ and $\delta^{18}O$ values. Sample name denotes site, soil gas well gallery, and well depth: "A1_10" = Site A, Well Set 1, 10cm depth. Null values (-) are due to no sample collected or single sample (pCO_2 ±SD) collected during the sampling event.

Sampling Date: 18 May 2013

Site/ Sample Name	Depth (cm)	Sampling Time (24h)	Temp (°C) Ave of 24 hr. before sampling	Soil CO_2 $\delta^{13}C$ (‰ VPDB)	Soil CO_2 $\delta^{18}O$ (‰ VSMOW)	Soil pCO_2 (ppm)	Soil pCO_2 (± S.D.)
A_Atm	0	13:00	15.7	-9.07	38.98	393	-
A1_10	10	13:00	21.1	-10.11	46.22	443	15
A1_25	25	13:00	20.9	-10.92	44.42	522	56
A1_50	50	13:00	19.8	-11.60	42.20	646	24
A1_100	100	13:00	17.2	-12.72	37.71	685	12
A2_25	25	13:00	20.9	-10.22	46.28	476	-
A2_50	50	13:00	19.8	-10.36	43.06	624	-
A2_100	100	13:00	17.2	-11.67	38.45	655	-
A3_10	10	13:00	21.1	-10.11	43.69	420	-
A3_25	25	13:00	20.9	-11.75	40.85	557	-
A3_50	50	13:00	19.8	-11.99	41.91	473	-
A3_95	95	13:00	17.2	-12.67	37.65	-	-
B_Atm	0	11:30	15.7	-9.15	39.70	377	-
B_10	10	11:30	21.6	-9.86	46.72	422	5
B_25	25	11:30	21.5	-10.82	43.68	450	7
B_42	42	11:30	21.4	-11.39	40.26	540	2
B_100	100	11:30	18	-10.76	36.31	627	4
C_Atm	0	10:00	10.1	-8.92	39.78	346	-
C_10	10	10:00	14	-10.97	42.56	503	21
C_25	25	10:00	16.8	-13.47	40.09	755	14
C_50	50	10:00	15.9	-14.12	38.93	1079	10
C_75	75	10:00	15	-14.56	38.19	1310	-
D_Atm	0	8:30	5.5	-8.44	39.21	407	-
D_10	10	8:30	8.6	-14.53	36.80	712	6
D_25	25	8:30	7.7	-17.63	35.22	2728	-
D_37	37	8:30	9.1	-17.57	35.41	3438	-
D_100	100	8:30	8.4	-18.16	35.11	4361	290

Supplementary Table 1 (cont'd). Soil CO_2 $\delta^{13}C$ and $\delta^{18}O$ values. Sample name denotes site, soil gas well gallery, and well depth: "A1_10" = Site A, Well Set 1, 10cm depth. Null values (-) are due to no sample collected or single sample (pCO_2 ±SD) collected during the sampling event.

Sampling Date: 26 August 2013

Site/ Sample Name	Depth (cm)	Sampling Time (24h)	Temp (°C) Ave of 24 hr. before sampling	Soil CO_2 $\delta^{13}C$ (‰ VPDB)	Soil CO_2 $\delta^{18}O$ (‰ VSMOW)	Soil pCO_2 (ppm)	Soil pCO_2 (± S.D.)
A_Atm	0	13:00	23.2	-8.77	35.91	478	8
A1_10	10	13:00	28.3	-	-	-	-
A1_25	25	13:00	27.2	-8.61	42.56	464	33
A1_50	50	13:00	26	-9.29	41.42	579	-
A1_100	100	13:00	24.3	-10.47	37.65	690	86
A2_25	25	13:00	27.2	-8.87	42.45	435	7
A2_50	50	13:00	26	-9.58	40.81	516	15
A2_100	100	13:00	24.3	-9.98	38.65	623	31
A3_10	10	13:00	28.3	-9.23	42.52	469	-
A3_25	25	13:00	27.2	-	-	-	-
A3_50	50	13:00	26	-10.29	40.13	571	7
A3_95	95	13:00	24.3	-10.87	37.81	678	50
B_Atm	0	11:30	21.9	-10.29	36.49	478	8
B_10	10	11:30	25.9	-11.02	34.94	553	17
B_25	25	11:30	26	-13.34	36.67	758	34
B_42	42	11:30	24.7	-14.07	37.91	993	23
B_100	100	11:30	23.6	-13.24	36.43	911	40
C_Atm	0	10:00	17.7	-12.48	38.82	737	5
C_10	10	10:00	20.2	-12.84	34.00	710	10
C_25	25	10:00	22.5	-15.1	37.51	1242	105
C_50	50	10:00	20	-15.43	39.08	1537	90
C_75	75	10:00	20.6	-15.49	37.80	1780	30
D_Atm	0	8:30	13.7	-13.74	37.63	929	85
D_10	10	8:30	12.1	-15.19	37.73	2061	31
D_25	25	8:30	12.9	-15.27	38.32	4260	2
D_37	37	8:30	15.7	-15.38	36.71	5019	205
D_100	100	8:30	15.2	-16.48	34.32	4877	522

Supplementary Table 1 (cont'd). Soil CO_2 $\delta^{13}C$ and $\delta^{18}O$ values. Sample name denotes site, soil gas well gallery, and well depth: "A1_10" = Site A, Well Set 1, 10cm depth. Null values (-) are due to no sample collected or single sample (pCO_2 ±SD) collected during the sampling event.

Sampling Date: 30 November 2013

Site/ Sample Name	Depth (cm)	Sampling Time (24h)	Temp (°C) Ave of 24 hr. before sampling	Soil CO_2 $\delta^{13}C$ (‰ VPDB)	Soil CO_2 $\delta^{18}O$ (‰ VSMOW)	Soil pCO_2 (ppm)	Soil pCO_2 (± S.D.)
A_Atm	0	15:00	-0.1	-9.3	33.42	401	11
A1_10	10	15:00	1.9	-9.49	39.66	457	15
A1_25	25	15:00	5.1	-11.04	42.84	387	9
A1_50	50	15:00	8.6	-11.97	43.04	360	6
A1_100	100	15:00	13	-12.01	38.80	448	8
A2_25	25	15:00	5.1	-10.39	45.87	413	29
A2_50	50	15:00	8.6	-11.47	45.59	418	10
A2_100	100	15:00	13	-11.79	40.53	489	18
A3_10	10	15:00	1.9	-10.59	41.08	420	43
A3_25	25	15:00	5.1	-11.12	43.61	406	70
A3_50	50	15:00	8.6	-11.84	42.83	397	1
A3_95	95	15:00	13	-12.18	39.20	474	-
B_Atm	0	13:30	3.5	-9.77	33.07	424	4
B_10	10	13:30	3.6	-9.65	37.97	432	1
B_25	25	13:30	5.6	-10.45	39.47	427	8
B_42	42	13:30	8.7	-11.48	40.07	466	4
B_100	100	13:30	13.3	-12.21	37.98	527	18
C_Atm	0	11:00	0.8	-10.96	31.40	575	8
C_10	10	11:00	1.3	-10.99	34.19	559	4
C_25	25	11:00	2.2	-11.91	37.21	613	20
C_50	50	11:00	5.3	-13.23	38.20	694	3
C_75	75	11:00	9.6	-13.85	38.26	808	8
D_Atm	0	9:00	-2.7	-9.96	32.02	375	3
D_10	10	9:00	-0.8	-10.67	35.55	522	4
D_25	25	9:00	0.3	-12.44	36.70	737	42
D_37	37	9:00	1.5	-13.57	36.92	949	66
D_100	100	9:00	4.5	-14.42	35.22	1559	47

Supplementary Table 1 (cont'd). Soil CO_2 $\delta^{13}C$ and $\delta^{18}O$ values. Sample name denotes site, soil gas well gallery, and well depth: "A1_10" = Site A, Well Set 1, 10cm depth. Null values (-) are due to no sample collected or single sample (pCO_2 ±SD) collected during the sampling event.

Sampling Date: 19 April 2014

Site/ Sample Name	Depth (cm)	Sampling Time (24h)	Temp (°C) Ave of 24 hr. before sampling	Soil CO_2 $\delta^{13}C$ (‰ VPDB)	Soil CO_2 $\delta^{18}O$ (‰ VSMOW)	Soil pCO_2 (ppm)	Soil pCO_2 (± S.D.)
A_Atm	0	13:00	15.7	-10.75	31.45	562	18
A1_10	10	13:00	20.4	-11.27	42.29	539	8
A1_25	25	13:00	19.4	-11.15	36.87	532	3
A1_50	50	13:00	17.1	-11.34	39.48	572	4
A1_100	100	13:00	14.5	-11.77	36.93	582	12
A2_25	25	13:00	19.4	-10.68	35.70	535	1
A2_50	50	13:00	17.1	-10.54	40.20	585	13
A2_100	100	13:00	14.5	-11.01	38.08	573	8
A3_10	10	13:00	20.4	-10.70	36.84	523	11
A3_25	25	13:00	19.4	-11.29	37.15	538	20
A3_50	50	13:00	17.1	-11.42	39.91	548	14
A3_95	95	13:00	14.5	-11.81	37.93	575	23
B_Atm	0	8:00	15.5	-9.11	34.33	368	17
B_10	10	8:00	20.8	-10.92	36.52	455	24
B_25	25	8:00	20.2	-13.36	36.82	651	19
B_42	42	8:00	16.6	-14.16	39.56	899	24
B_100	100	8:00	14.4	-12.97	36.37	941	17
C_Atm	0	9:30	11.9	-10.39	31.42	604	44
C_10	10	9:30	15.2	-11.49	36.37	561	0
C_25	25	9:30	17	-13.58	35.89	827	18
C_50	50	9:30	13.4	-14.63	37.86	1187	46
C_75	75	9:30	11.7	-15.06	38.10	1451	30
D_Atm	0	10:30	7.5	-10.76	36.17	556	78
D_10	10	10:30	9.3	-12.43	33.72	578	15
D_25	25	10:30	7.5	-14.74	35.36	1140	133
D_37	37	10:30	8.7	-15.41	35.81	1540	1
D_100	100	10:30	5.4	-15.75	36.26	2347	148

Supplementary Table 1 (cont'd). Soil CO_2 $\delta^{13}C$ and $\delta^{18}O$ values. Sample name denotes site, soil gas well gallery, and well depth: "A1_10" = Site A, Well Set 1, 10cm depth. Null values (-) are due to no sample collected or single sample (pCO_2 ±SD) collected during the sampling event.

Sampling Date: 31 May 2014

Site/ Sample Name	Depth (cm)	Sampling Time (24h)	Temp (°C) Ave of 24 hr. before sampling	Soil CO_2 $\delta^{13}C$ (‰ VPDB)	Soil CO_2 $\delta^{18}O$ (‰ VSMOW)	Soil pCO_2 (ppm)	Soil pCO_2 (± S.D.)
A_Atm	0	12:00	21.3	-8.90	38.09	442	10
A1_10	10	12:00	25.9	-9.68	43.20	563	5
A1_25	25	12:00	25	-10.60	41.42	697	42
A1_50	50	12:00	22.8	-11.12	41.99	808	5
A1_100	100	12:00	18.8	-11.56	38.35	769	11
A2_25	25	12:00	25	-10.13	41.33	585	13
A2_50	50	12:00	22.8	-10.26	43.42	712	40
A2_100	100	12:00	18.8	-10.95	39.41	713	24
A3_10	10	12:00	25.9	-10.10	44.87	571	38
A3_25	25	12:00	25	-11.85	39.18	778	22
A3_50	50	12:00	22.8	-11.11	43.01	804	11
A3_95	95	12:00	18.8	-12.01	38.81	801	32
B_Atm	0	8:00	20.6	-8.73	33.90	470	33
B_10	10	8:00	25.6	-11.27	38.33	566	53
B_25	25	8:00	24.7	-11.94	37.26	644	19
B_42	42	8:00	21.5	-12.01	38.57	744	36
B_100	100	8:00	18.4	-12.61	36.62	1005	64
C_Atm	0	10:30	17.6	-10.88	34.64	508	39
C_10	10	10:30	20.9	-10.61	40.78	577	15
C_25	25	10:30	22.5	-12.72	38.16	807	77
C_50	50	10:30	18.3	-13.51	38.40	1115	31
C_75	75	10:30	15.7	-14.01	40.20	1393	57
D_Atm	0	9:30	12.4	-9.31	34.98	550	162
D_10	10	9:30	13.3	-13.23	35.71	836	0
D_25	25	9:30	11.1	-15.26	35.74	1799	155
D_37	37	9:30	14	-15.55	39.02	2917	83
D_100	100	9:30	9.6	-15.44	39.45	4558	415

Appendix 2: Chapter 2, Supplementary Figures and Data Tables

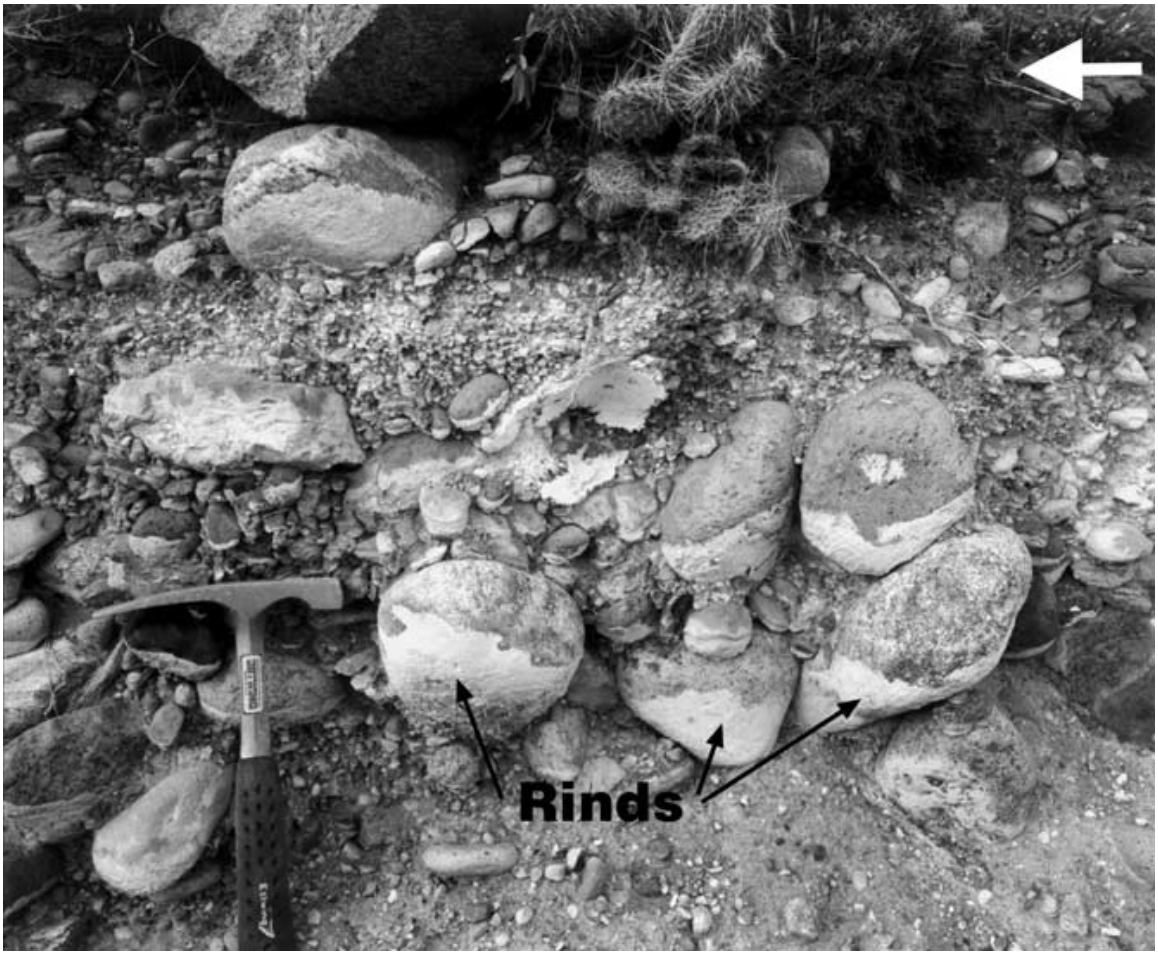

Supplementary Figure 1: Typical soil development in the Wind River Basin. Pedogenic carbonate rinds are located on the bottoms of clasts. White arrow denotes land surface (Sharp et al., 2003).

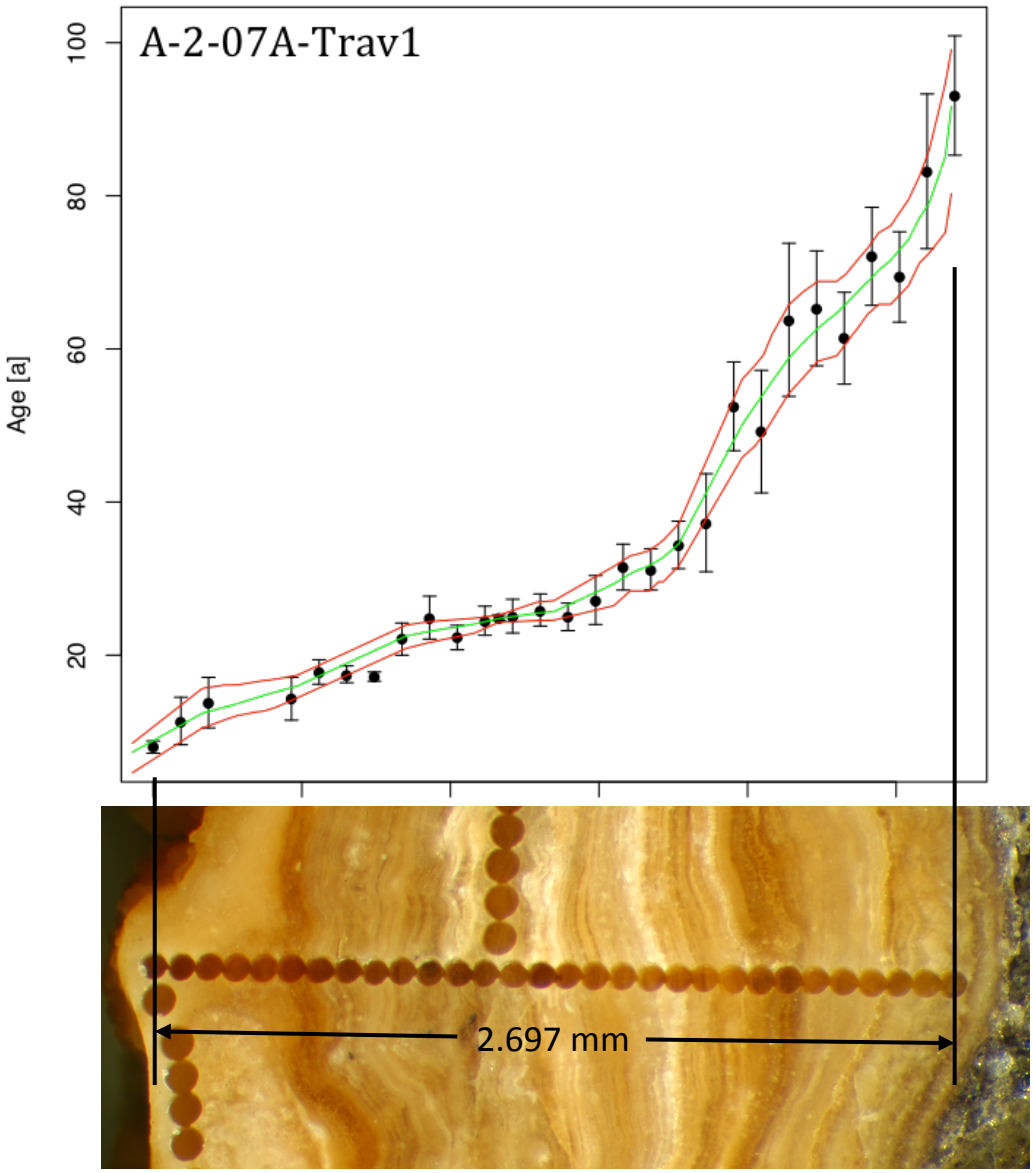

Supplementary Figure 2. StalAge model for sample A-2-07A, traverse 1. LA-ICPMS analyses along laminations on left side and midway along the transect are not presented.

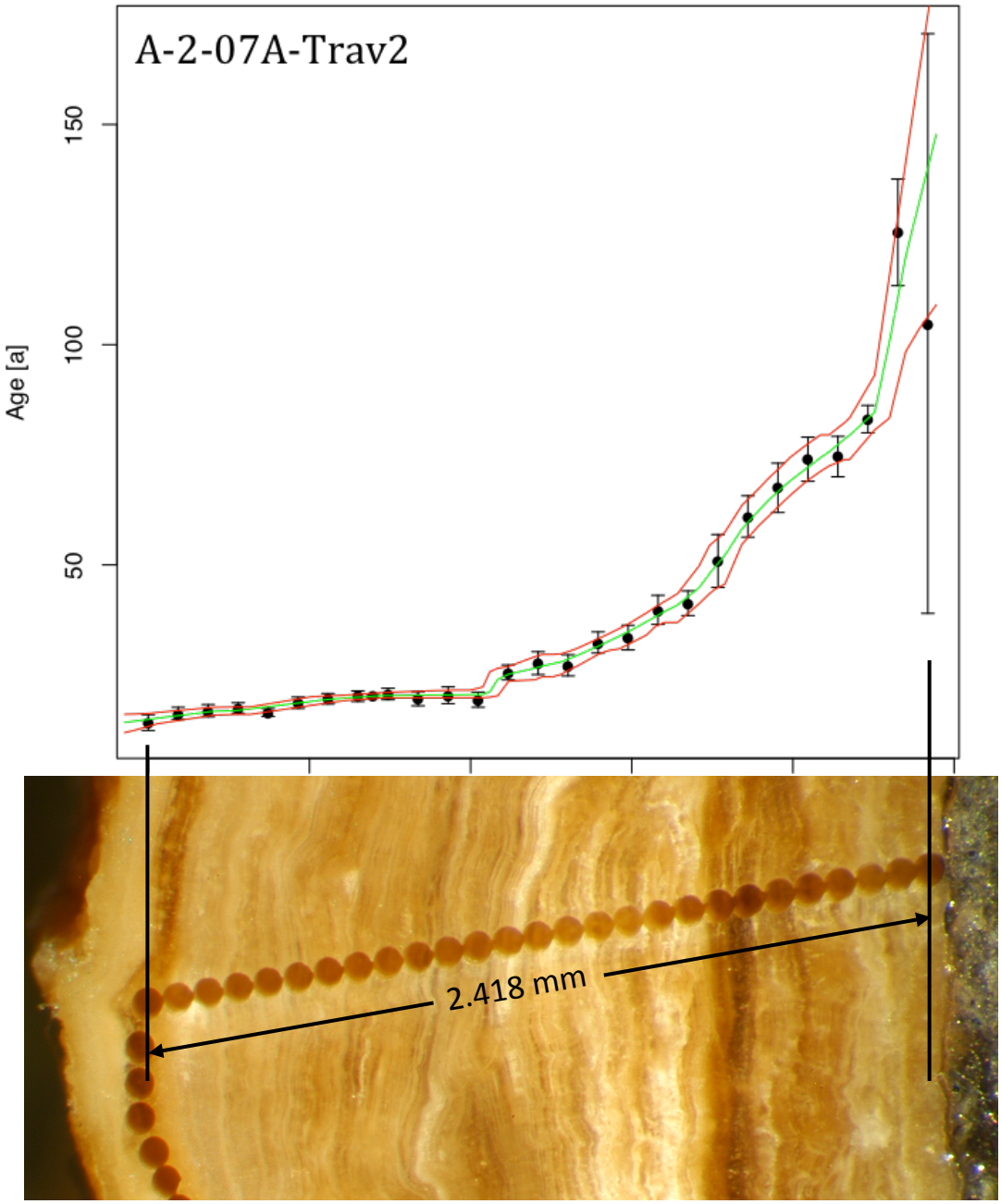

Supplementary Figure 3. StalAge model for sample A-2-07A, traverse 2. LA-ICPMS analyses along lamination on left side of sample are not presented.

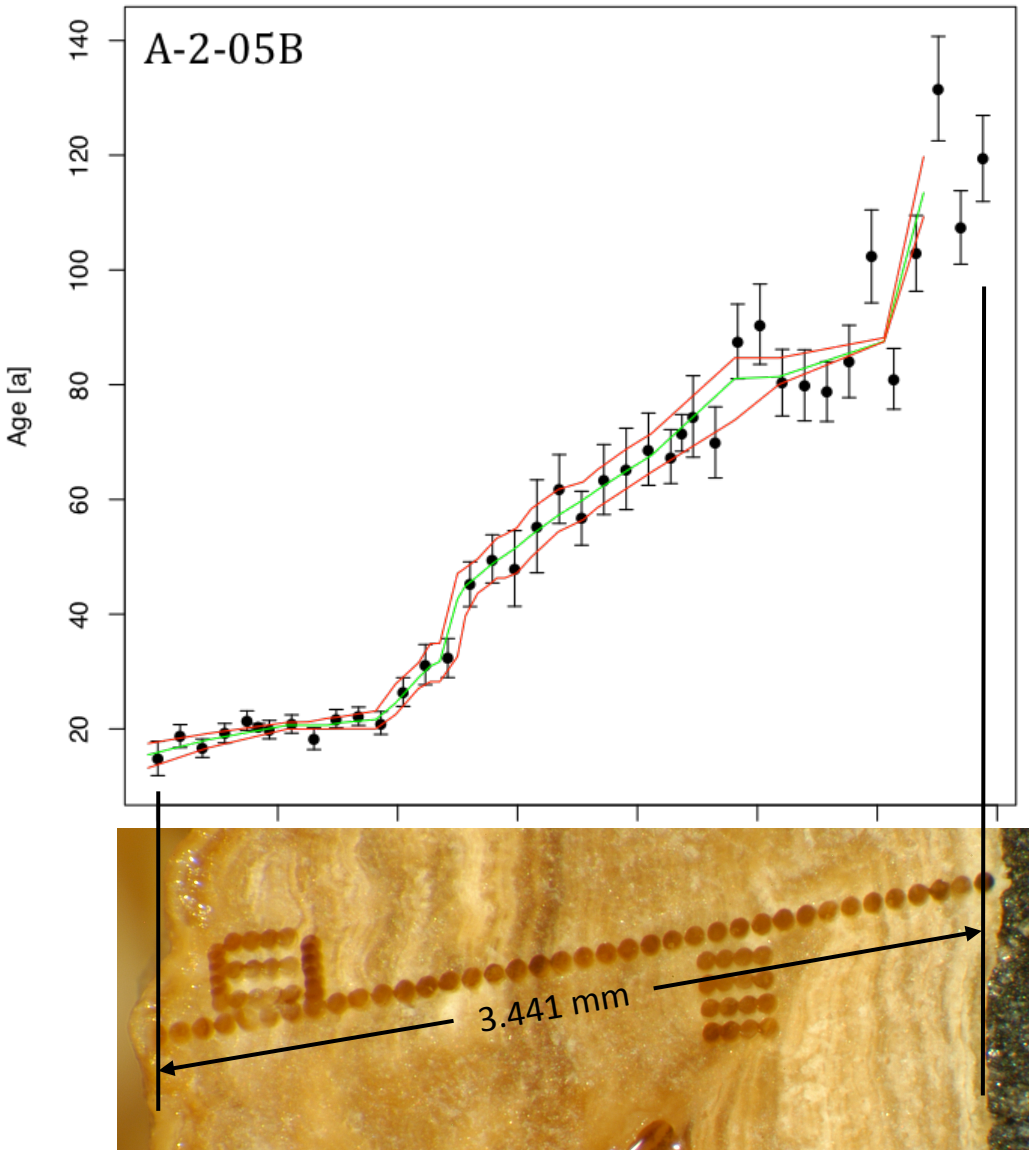

Supplementary Figure 4. StalAge model for sample A-2-05B. LA-ICPMS analyses in grid pattern on left side and midway along the transect are not presented.

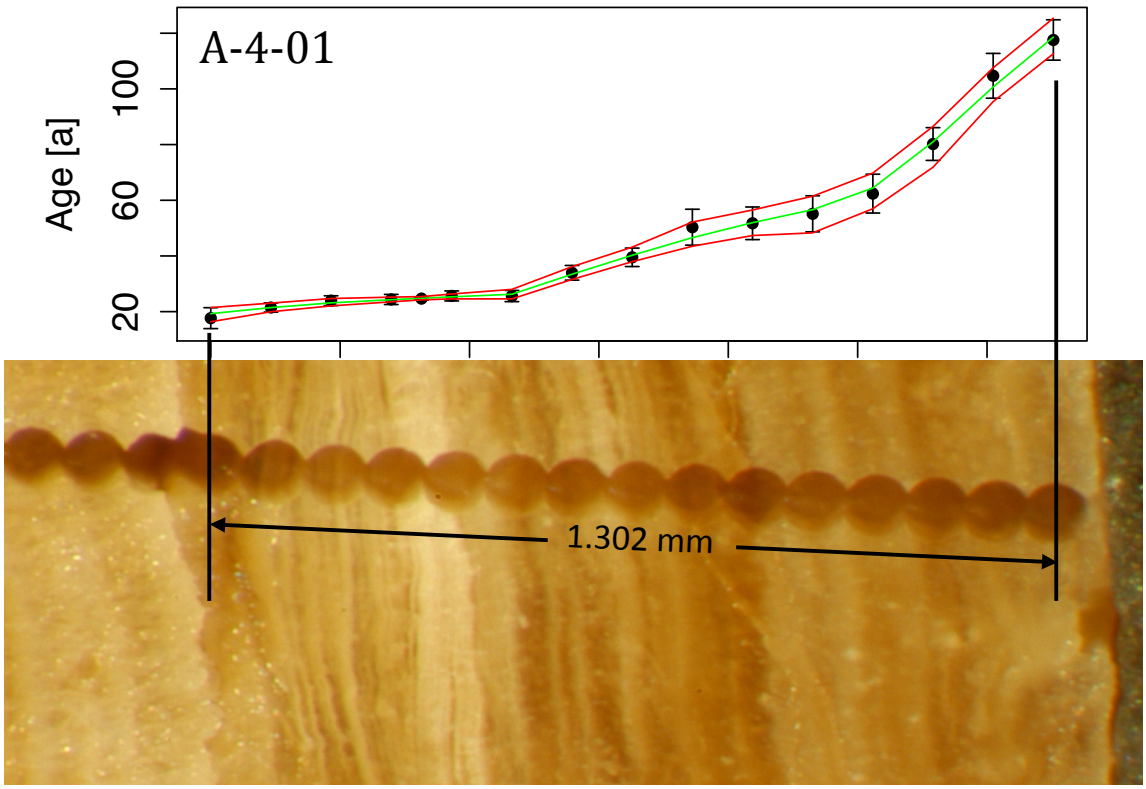

Supplementary Figure 5. Color photomicrograph and age model for sample A-4-01. Note visible discontinuity on left end of transect, LA-ICPMS analyses continued to the left, data yielded corrupt ^{230}Th/U ages and were not used.

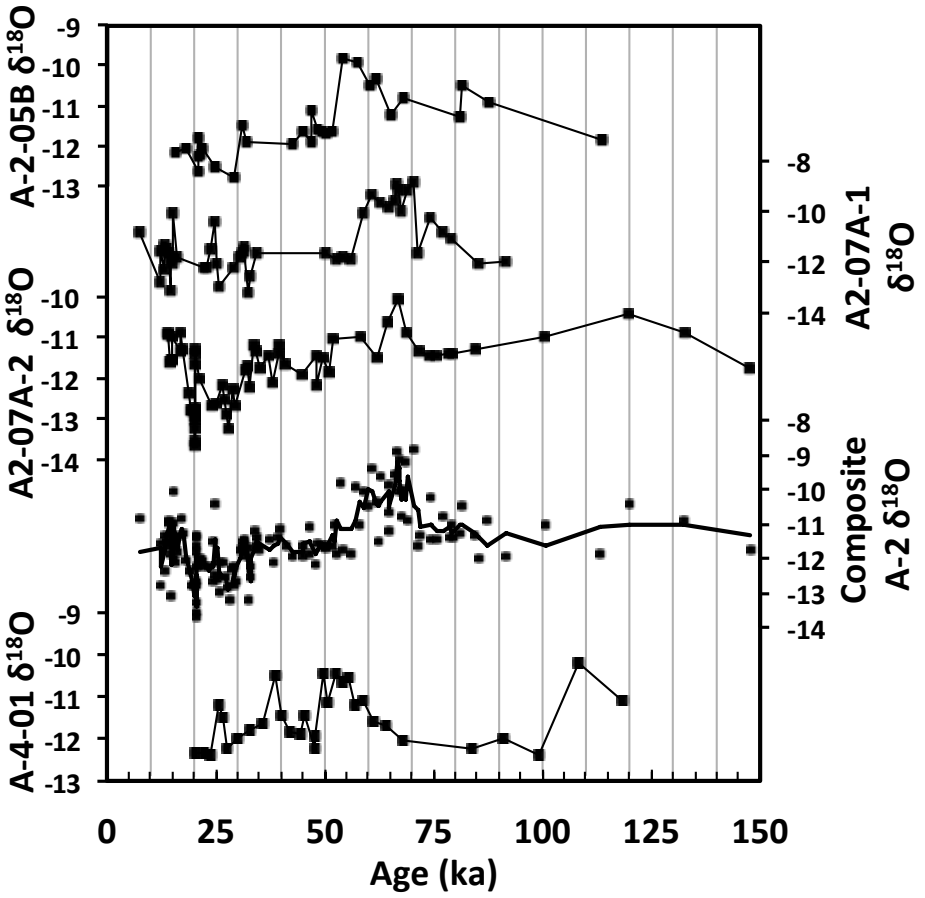

Supplementary Figure 6. Wind River pedogenic carbonate $\delta^{18}O_c$ values from samples at the Reservoir Locality. Composite A-2 record is merged data from samples A-2-05B, A-2-07A-1, and A-2-07A-2.

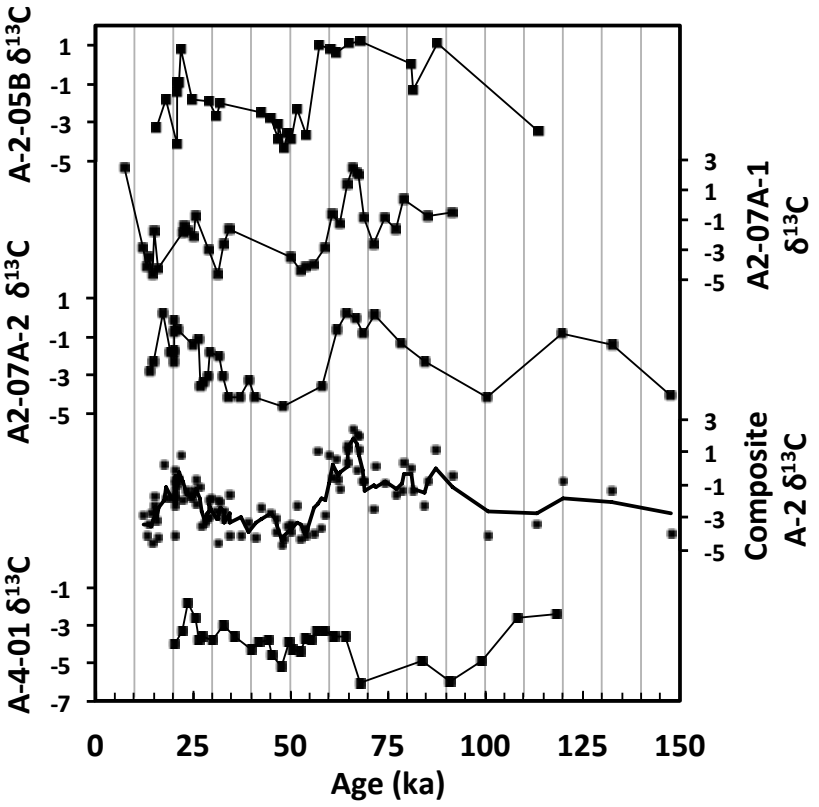

Supplementary Figure 7. Wind River pedogenic carbonate $\delta^{13}C_c$ values from samples at the Reservoir Locality. Composite A-2 record is merged data from samples A-2-05B, A-2-07A-1, and A-2-07A-2.

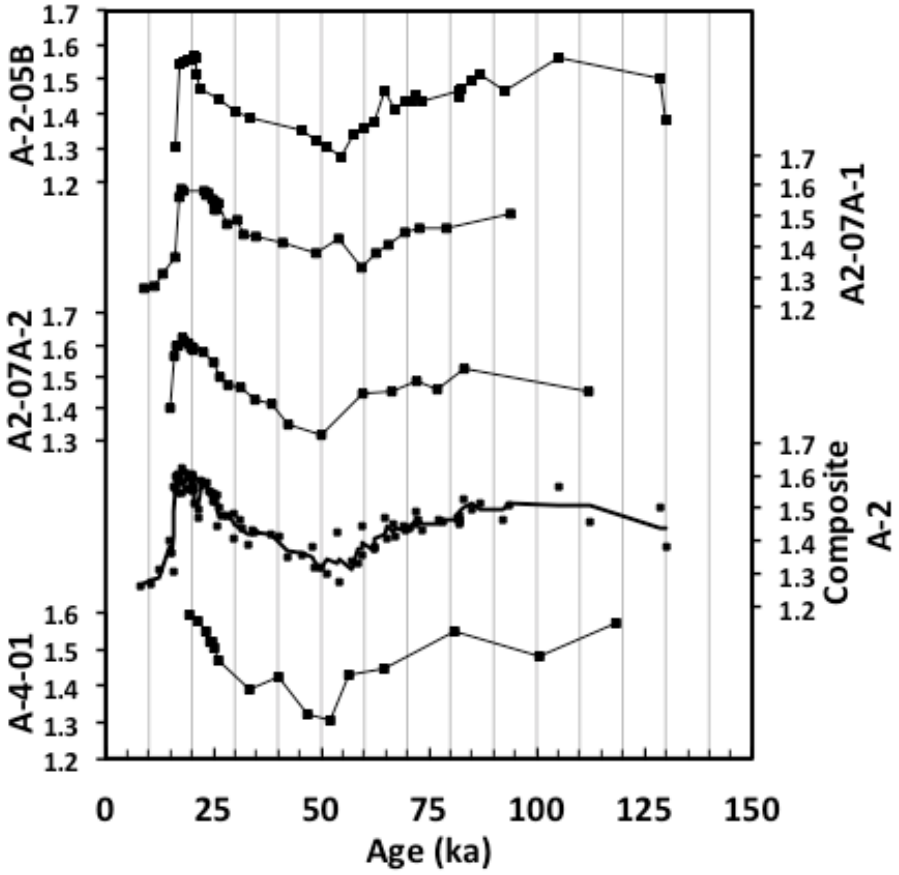

Supplementary Figure 8. Wind River pedogenic carbonate $^{234}U/^{238}U_i$ values from samples at the Reservoir Locality. Composite A-2 record is merged data from samples A-2-05B, A-2-07A-1, and A-2-07A-2.

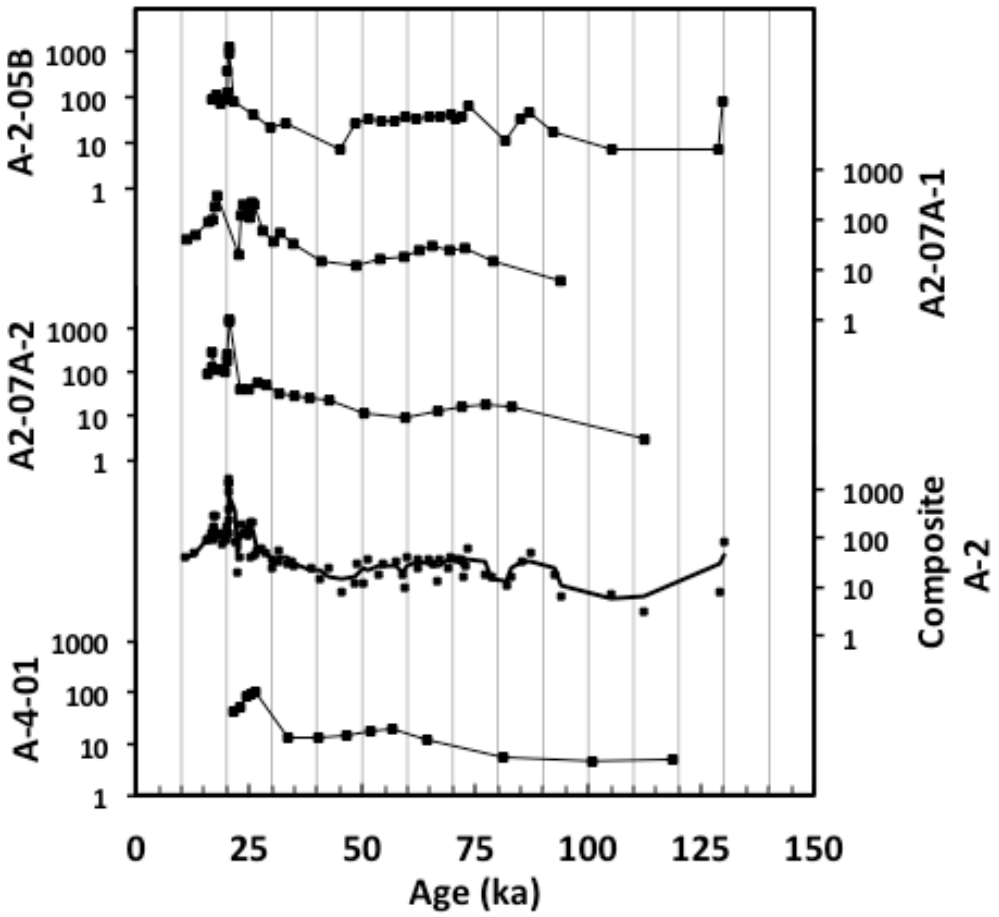

Supplementary Figure 9. Wind River pedogenic carbonate growth rate values from samples at the Reservoir Locality. Composite A-2 record is merged data from samples A-2-05B, A-2-07A-1, and A-2-07A-2. All growth rates are μm ka^{-1}, plotted on logarithmic scale.

Supplementary Table 1. Data from laser ablation ICP-MS U-series analyses

A-2-05B trav 1, laser ablation spot size 93 um

Spot no.	Dist. (um)	Err (um)	[232Th/ 238U]	Err (2s)	[230Th/ 238U]	Err (2s)	[234U/ 238U]	Err (2s)	Calibrated Age (ka)	Err (ka, 2se)	[234U/ 238U]i	Err (2se)
1	0	1	0.00318	0.00057	0.874	0.028	1.272	0.019	119.4	7.5	1.380	0.023
2	93	1	0.00171	0.00013	0.890	0.031	1.370	0.016	107.4	6.4	1.500	0.020
3	186	1	0.00106	0.00004	1.038	0.036	1.412	0.020	131.6	9.1	1.597	0.026
4	279	1	0.00043	0.00002	0.903	0.035	1.422	0.018	102.9	6.6	1.564	0.023
5	372	1	0.00015	0.00001	0.740	0.032	1.372	0.020	81.0	5.3	1.467	0.024
6	465	1	0.00020	0.00001	0.874	0.041	1.385	0.024	102.4	8.1	1.513	0.029
7	558	1	0.00020	0.00001	0.772	0.037	1.393	0.024	84.0	6.3	1.498	0.028
8	651	1	0.00017	0.00001	0.731	0.032	1.381	0.019	78.8	5.2	1.476	0.023
9	744	1	0.00020	0.00001	0.729	0.037	1.364	0.025	79.9	6.2	1.457	0.030
10	837	1	0.00020	0.00001	0.728	0.034	1.359	0.023	80.3	5.8	1.450	0.027
11	930	1	0.00026	0.00001	0.792	0.039	1.361	0.022	90.5	7.0	1.467	0.027
12	1023	1	0.00027	0.00001	0.777	0.038	1.366	0.020	87.5	6.5	1.469	0.024
13	1116	1	0.00027	0.00001	0.659	0.040	1.358	0.028	69.9	6.2	1.436	0.032
14	1209	1	0.00106	0.00007	0.695	0.045	1.368	0.026	74.5	7.1	1.455	0.031
drilled sample 1	1256	10	0.001064	0.0000011	0.6703	0.0075	1.358	0.0016	71.6	3.2	1.438	0.018
15	1302	1	0.00110	0.00006	0.642	0.031	1.360	0.022	67.5	4.7	1.435	0.025
16	1395	1	0.00091	0.00002	0.641	0.041	1.340	0.029	68.8	6.3	1.413	0.033
17	1488	1	0.00104	0.00003	0.642	0.051	1.390	0.029	65.3	7.1	1.470	0.034
18	1581	1	0.00091	0.00007	0.592	0.041	1.314	0.027	63.5	6.1	1.376	0.031
19	1674	1	0.00063	0.00004	0.539	0.033	1.305	0.023	56.7	4.7	1.358	0.026
20	1767	1	0.00177	0.00005	0.567	0.040	1.286	0.028	61.8	6.0	1.341	0.031
21	1860	1	0.00196	0.00004	0.499	0.055	1.236	0.040	55.3	8.1	1.276	0.045
22	1953	1	0.00098	0.00003	0.456	0.049	1.264	0.036	48.0	6.6	1.302	0.040
23	2046	1	0.00034	0.00002	0.474	0.031	1.279	0.025	49.6	4.2	1.321	0.027
24	2139	1	0.00039	0.00005	0.452	0.031	1.312	0.023	45.2	3.9	1.354	0.025
25	2232	1	0.00013	0.00001	0.352	0.031	1.356	0.030	32.3	3.4	1.390	0.032
26	2325	1	0.00027	0.00001	0.346	0.033	1.372	0.027	31.2	3.5	1.406	0.029
27	2418	1	0.00037	0.00001	0.307	0.026	1.411	0.026	26.4	2.5	1.443	0.027
28	2511	1	0.00042	0.00002	0.260	0.023	1.467	0.024	21.0	2.0	1.496	0.025
29	2604	1	0.00026	0.00001	0.268	0.017	1.441	0.018	22.2	1.6	1.470	0.019
30	2697	1	0.00026	0.00001	0.271	0.018	1.484	0.020	21.8	1.6	1.515	0.021
31	2790	1	0.00049	0.00002	0.239	0.022	1.532	0.026	18.3	1.9	1.560	0.027
32	2883	1	0.00034	0.00001	0.268	0.019	1.524	0.022	20.9	1.6	1.555	0.023
33	2976	1	0.00023	0.00001	0.258	0.018	1.532	0.022	19.9	1.6	1.563	0.023
drilled sample 2	3023	10	0.0001846	0.0000022	0.2658	0.0026	1.5363	0.0038	20.49	0.44	1.5682	0.0078
34	3069	1	0.00017	0.00001	0.275	0.020	1.525	0.019	21.4	1.7	1.558	0.020
35	3162	1	0.00021	0.00001	0.250	0.019	1.529	0.024	19.3	1.7	1.559	0.025
36	3255	1	0.00017	0.00001	0.217	0.019	1.524	0.022	16.6	1.6	1.550	0.023
37	3348	1	0.00029	0.00001	0.242	0.023	1.518	0.023	18.8	2.0	1.546	0.024
38	3441	1	0.00101	0.00003	0.165	0.031	1.292	0.038	14.9	3.0	1.304	0.039

Supplementary Table 1 (cont'd). Data from laser ablation ICP-MS U-series analyses

A-2-07A trav 1, laser ablation 93 um spot size

Spot no.	Dist. (um)	Err (um)	[232Th/ 238U]	Err (2s)	[230Th/ 238U]	Err (2s)	[234U/ 238U]	Err (2s)	Calibrated Age (ka)	Err (ka, 2s)	[234U/ 238U]i	Err (2se)
1	47	0.1	0.00039	0.00002	0.826	0.043	1.390	0.025	93.1	7.8	1.507	0.03
2	140	1	0.00141	0.00005	0.749	0.059	1.364	0.035	83.2	10.1	1.460	0.04
3	233	1	0.00323	0.00014	0.667	0.040	1.381	0.025	69.4	5.9	1.463	0.03
4	326	1	0.00115	0.00003	0.678	0.042	1.365	0.024	72.1	6.4	1.447	0.03
5	419	1	0.00024	0.00001	0.591	0.042	1.344	0.026	61.4	6.0	1.409	0.03
6	512	1	0.00561	0.00016	0.606	0.050	1.317	0.029	65.3	7.5	1.381	0.03
7	605	1	0.00792	0.00016	0.576	0.065	1.276	0.040	63.8	10.0	1.330	0.05
8	698	1	0.00742	0.00032	0.506	0.064	1.369	0.040	49.2	8.0	1.424	0.04
9	791	1	0.00095	0.00003	0.517	0.044	1.330	0.029	52.5	5.8	1.382	0.03
10	884	1	0.00107	0.00005	0.403	0.058	1.372	0.039	37.3	6.4	1.413	0.04
11	977	1	0.00087	0.00002	0.382	0.029	1.394	0.022	34.4	3.1	1.435	0.02
12	1070	1	0.00107	0.00006	0.353	0.026	1.402	0.021	31.2	2.7	1.439	0.02
13	1163	1	0.00268	0.00009	0.367	0.030	1.443	0.024	31.5	3.0	1.484	0.03
14	1256	1	0.00537	0.00009	0.322	0.033	1.440	0.026	27.2	3.2	1.475	0.03
15	1349	1	0.00122	0.00003	0.312	0.019	1.502	0.017	25.0	1.8	1.539	0.02
16	1442	1	0.00627	0.00038	0.318	0.022	1.487	0.019	25.9	2.1	1.524	0.02
17	1535	1	0.00201	0.00011	0.309	0.023	1.486	0.023	25.1	2.2	1.521	0.02
drilled sample 3	1582	10	0.003676	0.0000041	0.3118	0.0018	1.5110	0.0032	24.88	0.34	1.5481	0.0033
18	1628	1	0.00740	0.00059	0.309	0.022	1.518	0.021	24.5	1.9	1.555	0.02
19	1721	1	0.00776	0.00068	0.289	0.019	1.543	0.020	22.3	1.6	1.578	0.02
20	1814	1	0.00792	0.00138	0.316	0.031	1.532	0.025	24.9	2.8	1.571	0.03
21	1907	1	0.00893	0.00058	0.288	0.024	1.550	0.024	22.1	2.1	1.585	0.03
22	2000	1	0.00137	0.00005	0.229	0.007	1.552	0.010	17.2	0.6	1.580	0.01
23	2093	1	0.00553	0.00044	0.234	0.013	1.558	0.017	17.5	1.1	1.586	0.02
24	2186	1	0.00269	0.00018	0.233	0.019	1.534	0.022	17.8	1.6	1.561	0.02
25	2279	1	0.00158	0.00003	0.167	0.031	1.352	0.035	14.3	2.8	1.366	0.04
26*	2372	1	0.02461	0.00369	0.268	0.045	1.405	0.039	22.9	4.3	1.432	0.04
27*	2465	1	0.02294	0.00214	0.327	0.055	1.386	0.040	29.0	5.6	1.419	0.04
28	2558	1	0.00809	0.00118	0.155	0.034	1.298	0.035	13.8	3.3	1.310	0.04
29	2651	1	0.00527	0.00165	0.126	0.032	1.260	0.029	11.4	3.1	1.269	0.03
30	2744	1	0.00026	0.00001	0.089	0.009	1.256	0.015	8.0	0.8	1.262	0.01

*samples with unusually high 232Th/238U ratios; ages are of low reliability

A-2-07A trav 2, laser ablation 93 um spot size

Spot no.	Dist. (um)	Err (um)	[232Th/ 238U]	Err (2s)	[230Th/ 238U]	Err (2s)	[234U/ 238U]	Err (2s)	Calibrated Age (ka)	Err (ka, 2s)	[234U/ 238U]i	Err (2se)
1*	47	0.1	0.52314	0.035	0.876	0.278	1.369	0.255	104.8	65.8	1.496	0.30
2	140	1	0.03595	0.0014	0.937	0.047	1.320	0.024	125.5	12.1	1.456	0.032
3	233	1	0.00098	0.00015	0.781	0.019	1.418	0.012	83.1	3.1	1.528	0.014
4	326	1	0.00098	0.00002	0.701	0.030	1.376	0.018	74.6	4.6	1.465	0.021
5	419	1	0.00109	0.00003	0.708	0.033	1.398	0.021	74.0	5.0	1.490	0.024
6	512	1	0.00622	0.00029	0.650	0.038	1.374	0.023	67.5	5.6	1.452	0.026
7	605	1	0.00469	0.00008	0.603	0.034	1.378	0.025	61.0	4.7	1.449	0.028
8	698	1	0.00390	0.00006	0.483	0.044	1.275	0.032	50.9	6.0	1.318	0.035
9	791	1	0.00051	0.00002	0.419	0.023	1.313	0.017	41.3	2.8	1.351	0.019
10	884	1	0.00623	0.00059	0.426	0.029	1.374	0.022	39.8	3.3	1.419	0.024
11	977	1	0.00081	0.00002	0.372	0.026	1.390	0.022	33.5	2.8	1.428	0.024
12	1070	1	0.00266	0.00012	0.371	0.023	1.425	0.020	32.4	2.4	1.465	0.021
13	1163	1	0.00371	0.00010	0.321	0.025	1.439	0.025	27.2	2.4	1.474	0.026
14	1256	1	0.00497	0.00008	0.333	0.027	1.465	0.024	27.7	2.6	1.503	0.026
15	1349	1	0.00190	0.00007	0.319	0.019	1.506	0.018	25.6	1.7	1.544	0.019
16	1442	1	0.00352	0.00017	0.255	0.020	1.547	0.021	19.4	1.7	1.578	0.022
17	1535	1	0.00194	0.00003	0.270	0.022	1.561	0.021	20.4	1.9	1.594	0.022
18	1628	1	0.00678	0.00051	0.258	0.019	1.553	0.021	19.6	1.6	1.585	0.021
19	1721	1	0.00347	0.00021	0.273	0.016	1.558	0.016	20.7	1.3	1.592	0.016
drilled sample 4	1768	10	0.001009	0.0000021	0.2686	0.0022	1.5697	0.0028	20.24	0.37	1.6032	0.0029
20	1815	1	0.00168	0.00006	0.267	0.015	1.561	0.016	20.2	1.2	1.594	0.017
21	1908	1	0.00371	0.00010	0.261	0.014	1.571	0.015	19.6	1.2	1.603	0.016
22	2000	1	0.00559	0.00024	0.251	0.016	1.578	0.017	18.7	1.3	1.609	0.018
23	2093	1	0.00126	0.00003	0.226	0.012	1.594	0.015	16.5	0.9	1.622	0.015
24	2186	1	0.00671	0.00036	0.235	0.015	1.572	0.018	17.5	1.2	1.601	0.018
25	2279	1	0.00644	0.00050	0.227	0.017	1.568	0.019	16.9	1.4	1.596	0.020
26	2372	1	0.00713	0.00048	0.215	0.017	1.541	0.021	16.3	1.4	1.566	0.022
27	2465	1	0.00486	0.00061	0.170	0.020	1.388	0.025	14.2	1.8	1.404	0.026

* Very imprecise due Th correction

Supplementary Table 1 (cont'd). Data from laser ablation ICP-MS U-series analyses

A-4-01 trav 1, laser ablation 93 um spot size

Spot no.	Dist. (um)	Err (um)	[232Th/ 238U]	Err (2s)	[230Th/ 238U]	Err (2s)	[234U/ 238U]	Err (2s)	Calibrated Age (ka)	Err (ka, 2s)	[234U/ 238U]i	Err (2se)
1	0	0.1	0.01189	0.0021	0.972	0.033	1.410	0.017	117.6	7.3	1.572	0.022
2	93	1	0.00112	0.00004	0.868	0.039	1.358	0.023	104.7	8.0	1.481	0.029
3	186	1	0.00199	0.00006	0.773	0.038	1.438	0.022	80.2	5.9	1.550	0.027
4	279	1	0.00121	0.00005	0.614	0.050	1.377	0.031	62.4	7.0	1.449	0.035
5	372	1	0.00089	0.00002	0.554	0.049	1.367	0.036	55.1	6.5	1.429	0.041
6	465	1	0.00136	0.00011	0.485	0.042	1.265	0.033	51.7	5.9	1.306	0.037
7	558	1	0.00198	0.00012	0.481	0.047	1.281	0.036	50.3	6.4	1.324	0.041
8	651	1	0.00023	0.00002	0.425	0.029	1.377	0.025	39.5	3.3	1.422	0.027
9	744	1	0.00020	0.00002	0.367	0.024	1.357	0.021	33.9	2.6	1.392	0.023
10	837	1	0.00025	0.00007	0.304	0.021	1.439	0.023	25.6	2.0	1.472	0.024
11	930	1	0.00026	0.00003	0.311	0.019	1.469	0.020	25.6	1.8	1.504	0.021
drilled sample 5	977	10	0.0002238	0.0000031	0.3040	0.0026	1.4844	0.0065	24.68	0.53	1.5194	0.0068
12	1024	1	0.00024	0.00004	0.300	0.020	1.484	0.018	24.4	1.8	1.518	0.019
13	1117	1	0.00220	0.00004	0.302	0.020	1.515	0.020	23.9	1.8	1.551	0.021
14	1210	1	0.00098	0.00003	0.279	0.019	1.543	0.019	21.5	1.6	1.577	0.020
15	1303	1	0.00385	0.00045	0.236	0.046	1.564	0.044	17.7	3.8	1.593	0.046

Supplementary Table 2. Data table with modeled ages of C and O SIMS data

A-2-05B

Age (kya)	Age Uncert (+) (kya)	Age Uncert (-) (kya)	$\delta^{18}O$ (PDB)	$\delta^{18}O$ (PDB) (±2SD)	$\delta^{13}C$ (PDB)	$\delta^{13}C$ (PDB) (±2SD)
113.44	6.29	4.20	-11.86	0.32	-3.40	0.83
87.55	0.63	0.03	-10.91	0.32	1.09	0.83
81.39	3.28	1.35	-10.48	0.32	-1.34	0.83
81.06	3.61	7.23	-11.29	0.32	-0.03	0.83
67.69	3.80	2.91	-10.80	0.32	1.14	0.83
64.93	3.83	3.07	-11.20	0.32	1.10	0.83
61.68	3.51	3.10	-10.35	0.32	0.54	0.83
59.96	3.11	3.50	-10.50	0.32	0.78	0.83
57.23	4.51	2.87	-9.91	0.32	0.98	0.83
53.76	4.59	3.83	-9.81	0.32	-3.63	0.83
51.70	3.34	4.54	-11.66	0.32	-2.31	0.80
50.27	3.62	3.96	-11.70	0.24	-3.86	0.80
49.36	3.92	3.05	-11.61	0.32	-3.49	0.80
48.28	3.43	3.21	-11.56	0.24	-4.27	0.80
46.64	2.99	3.00	-11.10	0.24	-3.05	0.80
46.64	2.99	3.00	-11.88	0.32	-3.85	0.80
44.96	3.11	5.25	-11.61	0.24	-2.76	0.80
42.64	4.45	10.02	-11.93	0.32	-2.44	0.80
31.75	3.19	3.50	-11.92	0.24	-2.02	0.80
30.95	3.93	2.70	-11.50	0.24	-2.64	0.80
28.91	2.59	1.88	-12.79	0.24	-1.90	1.02
24.52	3.31	2.01	-12.51	0.24	-1.77	1.02
21.64	1.51	1.61	-12.04	0.24	0.78	1.02
21.11	1.04	1.08	-12.22	0.24	-0.99	1.02
20.64	1.21	0.66	-12.27	0.24	-0.92	1.02
20.64	0.58	0.67	-11.80	0.24	-1.42	1.02
20.63	0.51	0.66	-12.64	0.24	-4.15	1.02
18.10	1.10	1.41	-12.05	0.24	-1.79	1.02
15.48	1.98	2.28	-12.15	0.24	-3.21	1.02

Supplementary Table 2 (cont'd). Data table with modeled ages of C and O SIMS data

A-2-07A-1

Age (kya)	Age Uncert (+) (kya)	Age Uncert (-) (kya)	$\delta^{18}O$ (PDB)	$\delta^{18}O$ (PDB) (±2SD)	$\delta^{13}C$ (PDB)	$\delta^{13}C$ (PDB) (±2SD)
91.66	7.40	11.39	-11.97	0.15	-0.44	0.84
85.16	9.55	9.95	-12.02	0.15	-0.80	0.84
79.06	6.92	6.55	-11.03	0.15	0.38	0.84
77.12	5.45	5.88	-10.81	0.15	-1.63	0.84
74.28	5.22	6.04	-10.27	0.15	-0.92	0.84
71.60	4.48	5.78	-11.64	0.15	-2.56	0.84
70.24	4.91	4.43	-8.85	0.15	-	-
68.77	4.38	4.24	-9.19	0.15	-0.82	0.84
67.42	4.20	4.77	-10.02	0.15	1.98	0.49
66.98	4.09	4.85	-9.16	0.15	2.05	0.49
66.66	4.05	4.91	-8.93	0.15	-	-
65.94	3.89	5.17	-9.55	0.15	2.44	0.49
64.70	4.13	5.60	-9.85	0.15	1.34	0.49
62.70	6.12	4.30	-9.66	0.15	-1.23	0.84
60.79	6.65	4.58	-9.37	0.29	-0.59	0.84
58.78	6.97	4.62	-10.09	0.29	-2.90	0.49
55.81	6.16	5.11	-11.86	0.29	-4.01	0.49
54.15	5.10	5.31	-11.77	0.29	-4.07	0.67
52.55	5.28	5.25	-11.91	0.29	-4.27	0.49
50.10	5.95	4.27	-11.66	0.29	-3.45	0.49
34.60	2.66	2.86	-11.63	0.29	-1.55	0.67
32.78	2.24	3.20	-12.57	0.29	-2.66	0.67
32.40	2.13	2.82	-13.21	0.29	-	-
31.69	1.99	3.26	-11.55	0.32	-	-
31.64	1.98	3.25	-11.43	0.29	-4.60	0.49
31.00	2.14	2.61	-11.67	0.29	-	-
30.63	2.34	2.25	-11.78	0.29	-	-
29.30	2.30	2.84	-12.21	0.29	-2.91	0.49
25.69	1.43	1.11	-12.99	0.32	-0.70	0.67
25.48	1.44	0.97	-12.09	0.32	-2.13	0.67
24.77	0.45	0.49	-10.41	0.32	-	-
24.07	0.75	1.20	-11.49	0.32	-1.71	0.67
23.09	1.29	1.46	-12.24	0.32	-1.35	0.67
22.47	1.44	1.60	-12.23	0.32	-1.88	0.67
15.98	1.42	1.54	-11.85	0.32	-4.25	0.67
15.28	1.63	1.96	-10.04	0.32	-1.73	0.67
15.19	1.69	2.01	-12.02	0.32	-	-
14.83	1.86	2.05	-11.88	0.32	-4.54	0.67
14.71	1.95	2.04	-13.10	0.32	-	-
14.43	2.09	1.85	-11.65	0.32	-	-
13.64	2.47	1.56	-11.50	0.32	-3.42	0.67
13.31	2.78	1.60	-11.33	0.32	-4.07	0.67
13.20	2.90	1.67	-12.34	0.32	-	-
12.48	3.22	1.91	-11.57	0.32	-2.83	0.67
12.34	3.22	1.92	-12.78	0.32	-	-
7.31	1.18	2.69	-10.83	0.32	2.43	0.67

Supplementary Table 2 (cont'd). Data table with modeled ages of C and O SIMS data

A-2-07A-2 Age (kya)	Age Uncert (+) (kya)	Age Uncert (-) (kya)	$\delta^{18}O$ (PDB)	$\delta^{18}O$ (PDB) (±2SD)	$\delta^{13}C$ (PDB)	$\delta^{13}C$ (PDB) (±2SD)
147.74	39.56	78.27	-11.78	0.28	-4.00	0.56
132.61	29.76	58.67	-10.88	0.28	-1.36	0.56
119.95	21.45	43.00	-10.40	0.28	-0.82	0.56
100.67	14.94	32.27	-11.01	0.28	-4.10	0.56
84.66	8.42	12.43	-11.31	0.28	-2.29	0.56
79.42	3.93	9.44	-11.38	0.28	-	-
78.53	3.75	8.37	-11.38	0.28	-1.34	0.56
75.65	3.85	7.06	-11.45	0.28	-	-
74.33	5.17	8.28	-11.44	0.28	-	-
71.92	5.35	8.26	-11.35	0.28	0.16	0.56
69.13	5.34	8.63	-10.89	0.27	-0.78	0.56
67.17	5.02	8.49	-10.07	0.27	-0.07	0.56
64.80	5.02	8.65	-10.65	0.27	0.31	0.56
62.35	4.96	8.40	-11.52	0.27	-0.66	0.56
58.16	5.35	8.83	-11.01	0.27	-3.59	0.57
52.19	5.27	11.82	-11.04	0.27	-	-
50.88	5.55	11.34	-11.87	0.19	-4.09	0.57
49.58	5.94	11.01	-11.49	0.19	-4.14	0.57
48.09	6.37	10.94	-12.18	0.27	-4.67	0.57
48.04	6.39	10.94	-11.43	0.19	-4.19	0.57
44.84	4.93	8.58	-11.93	0.27	-	-
40.88	2.59	6.54	-11.63	0.27	-4.17	0.57
39.52	2.29	4.88	-11.18	0.19	-	-
39.38	2.31	4.75	-11.38	0.27	-3.26	0.57
38.21	2.17	4.39	-12.09	0.27	-	-
37.08	2.01	5.03	-11.43	0.27	-4.11	0.57
35.08	1.80	4.68	-11.75	0.27	-	-
34.45	1.73	4.60	-11.37	0.18	-4.12	0.57
33.87	1.73	4.63	-11.21	0.18	-	-
32.77	1.70	3.88	-12.22	0.18	-3.02	0.57
32.39	1.70	3.70	-11.69	0.18	-	-
31.69	1.72	3.52	-11.83	0.18	-1.98	1.07
29.41	1.61	4.03	-12.68	0.18	-1.83	1.07
28.77	1.66	4.18	-12.28	0.18	-3.03	1.07
28.00	1.80	4.66	-13.23	0.18	-3.33	1.07
27.53	2.15	5.10	-12.88	0.18	-	-
27.02	2.66	5.10	-12.54	0.18	-3.55	1.07
26.55	2.62	5.26	-12.15	0.18	-1.08	1.07
25.21	1.75	3.31	-12.62	0.18	-1.36	1.07
24.05	2.49	6.24	-12.69	0.18	-	-
21.21	4.55	5.80	-12.02	0.19	-0.63	1.07
20.54	1.76	2.46	-11.38	0.19	-0.69	1.07
20.52	1.05	1.75	-11.63	0.19	-0.16	1.07
20.48	1.09	1.75	-12.78	0.19	-	-
20.48	1.08	1.75	-13.04	0.19	-1.76	0.52
20.47	1.06	1.73	-12.93	0.19	-2.11	0.52
20.47	1.04	1.71	-13.58	0.19	-	-
20.46	1.02	1.68	-13.27	0.19	-2.27	0.52
20.46	1.02	1.68	-12.76	0.19	-2.46	0.52
20.42	0.90	1.52	-11.32	0.19	-1.78	0.52
20.33	0.67	1.21	-13.68	0.19	-1.71	0.52
19.77	0.65	1.21	-12.76	0.19	-	-
19.29	0.87	1.75	-12.80	0.19	-1.84	0.52
18.98	1.06	1.95	-12.39	0.19	-	-
17.32	0.44	1.70	-11.28	0.19	0.28	0.52
16.92	0.84	1.70	-10.87	0.19	-	-
16.76	0.91	1.79	-11.36	0.19	-	-
15.21	1.29	2.56	-11.00	0.19	-2.25	0.52
15.15	1.29	2.62	-11.54	0.19	-	-
14.99	1.32	2.78	-11.55	0.19	-	-
14.52	1.61	3.69	-11.60	0.19	-	-
14.27	1.84	4.10	-10.91	0.19	-2.73	0.52
14.23	1.84	4.15	-10.95	0.19	-	-

Supplementary Table 2 (cont'd). Data table with modeled ages of C and O SIMS data

A-4-01

Age (kya)	Age Uncert (+) (kya)	Age Uncert (-) (kya)	$\delta^{18}O$ (PDB)	$\delta^{18}O$ (PDB) (±2SD)	$\delta^{13}C$ (PDB)	$\delta^{13}C$ (PDB) (±2SD)
118.33	6.63	6.14	-11.09	0.20	-2.37	0.64
108.46	8.06	5.86	-10.19	0.20	-2.57	0.64
99.37	5.95	5.01	-12.39	0.20	-4.83	0.64
90.82	4.94	15.42	-11.97	0.20	-5.93	0.64
83.81	5.25	11.07	-12.22	0.20	-4.90	0.64
68.12	6.39	9.11	-12.01	0.20	-6.02	0.64
64.29	5.50	7.30	-11.70	0.20	-3.58	0.64
61.32	5.30	8.79	-11.57	0.20	-3.60	0.64
58.70	5.12	6.73	-11.06	0.20	-3.31	0.68
56.76	4.78	8.35	-11.17	0.20	-3.29	0.68
55.36	4.43	8.88	-10.52	0.20	-3.75	0.68
54.24	4.78	7.76	-10.62	0.20	-3.64	0.68
52.73	4.60	6.25	-10.44	0.20	-4.41	0.68
50.44	4.51	5.55	-11.13	0.37	-4.23	0.68
49.53	5.04	5.02	-10.45	0.37	-3.91	0.68
47.57	5.45	3.19	-11.93	0.37	-5.13	0.68
47.57	5.45	3.19	-12.24	0.37	-	-
45.25	5.97	3.08	-11.45	0.37	-4.60	0.68
44.31	6.07	3.05	-11.90	0.37	-3.81	0.68
41.75	3.23	2.43	-11.86	0.37	-3.84	0.76
40.03	3.00	2.28	-11.43	0.37	-4.27	0.76
38.83	3.09	2.26	-10.50	0.37	-	-
35.65	2.56	1.79	-11.62	0.37	-3.62	0.76
32.72	2.83	1.87	-11.78	0.37	-3.00	0.76
30.02	3.35	4.50	-11.99	0.37	-3.79	0.76
27.70	2.75	2.47	-12.25	0.37	-3.55	0.76
26.71	2.10	1.70	-11.49	0.37	-3.82	0.76
25.61	1.04	1.55	-11.20	0.37	-2.55	0.76
23.68	1.19	0.95	-12.36	0.37	-1.79	0.76
22.07	1.56	1.34	-12.31	0.37	-3.32	0.76
20.45	2.12	2.04	-12.31	0.37	-3.95	0.76

Supplementary Table 3. $\delta^{13}C_c$ and $\delta^{18}O_c$ values along laminations in sample A-2-07A

Sample	Age (ka)	Age + (ka)	Age - (ka)	δ18O [PDB]	δ18O ±2SD	δ13C (PDB)	δ13C ±2SD
A-2-07A Traverse 1	67.42	4.20	4.77	-10.02	0.15	1.98	0.49
	66.98	4.09	4.85	-9.16	0.15	2.05	0.49
	65.94	3.89	5.17	-9.55	0.15	2.44	0.49
Ave	66.78			-9.58		2.16	
St Dev of Ave	0.76			0.43		0.25	
A-2-07A Traverse 2	50.88	5.55	11.34	-11.87	0.19	-4.09	0.57
	49.58	5.94	11.01	-11.49	0.19	-4.14	0.57
	48.09	6.37	10.94	-12.18	0.27	-4.67	0.57
	48.04	6.39	10.94	-11.43	0.19	-4.19	0.57
Ave	49.15			-11.74		-4.27	
St Dev of Ave	1.36			0.35		0.27	
A-2-07A Trans B	20.48	1.08	1.75	-13.04	0.19	-1.76	0.52
	20.47	1.06	1.73	-12.93	0.19	-2.11	0.52
	20.46	1.02	1.68	-13.27	0.19	-2.27	0.52
	20.46	1.02	1.68	-12.76	0.19	-2.46	0.52
Ave	20.47			-13.00		-2.15	
St Dev of Ave	0.01			0.21		0.30	

Appendix 3: Chapter 3, Supplementary Figures and Data Tables

Supplementary Figure 1a. Geochemical mass balance plots for arid-climate El Tesoro paleosols

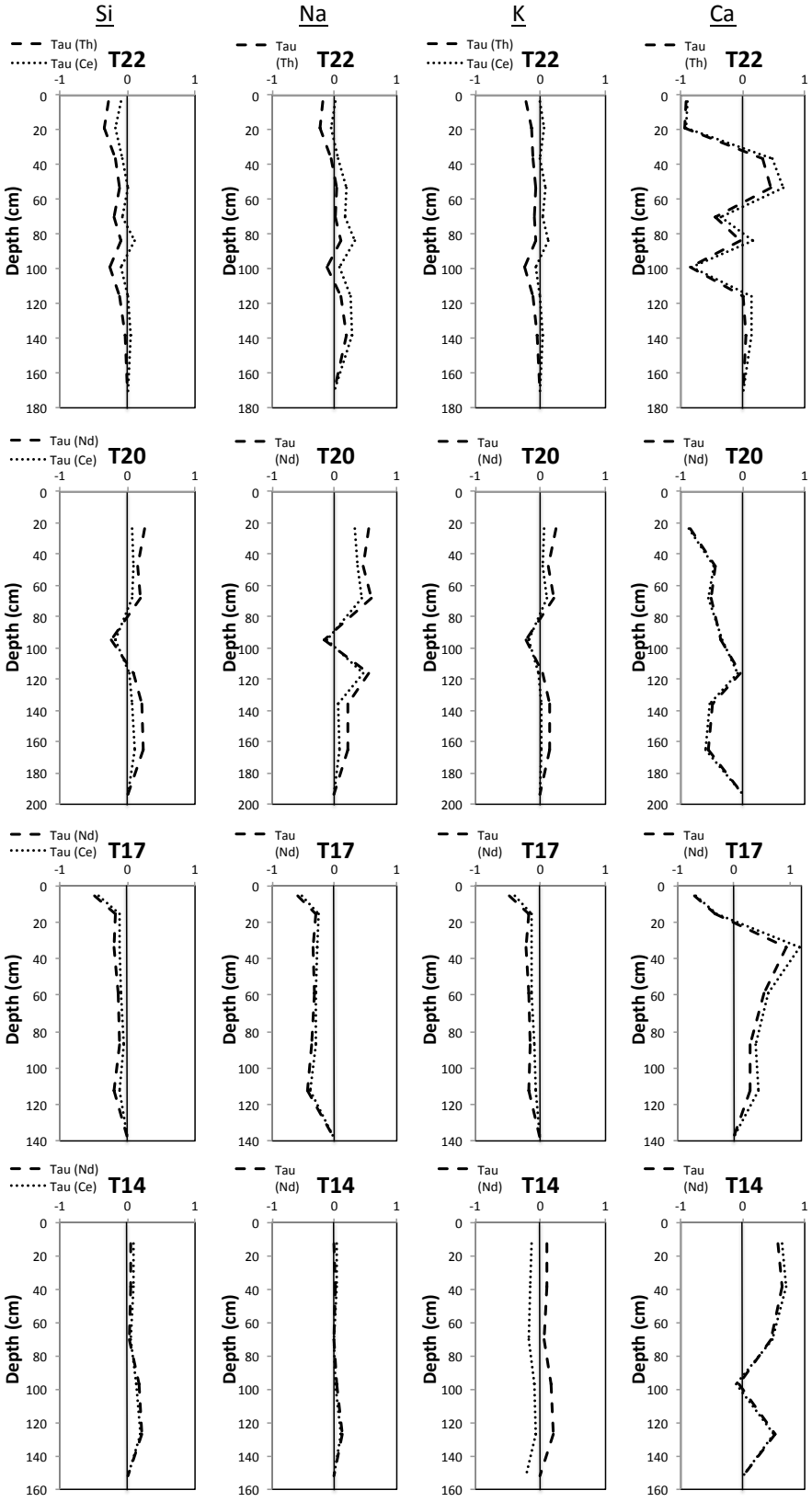

Supplementary Figure 1b. Geochemical mass balance plots for arid-climate El Tesoro paleosols

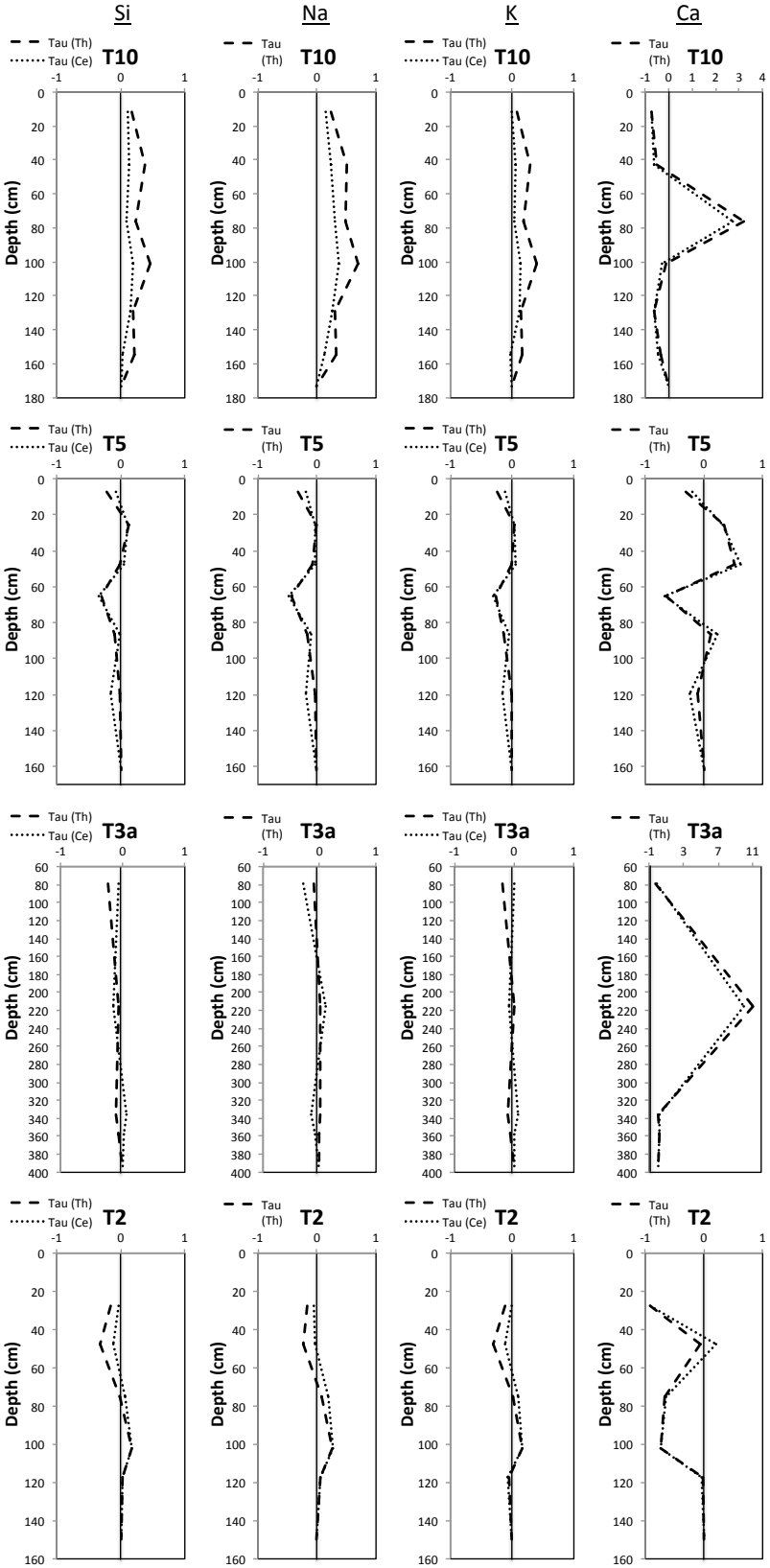

Supplementary Figure 1c. Geochemical mass balance plots for humid-climate El Tesoro paleosols

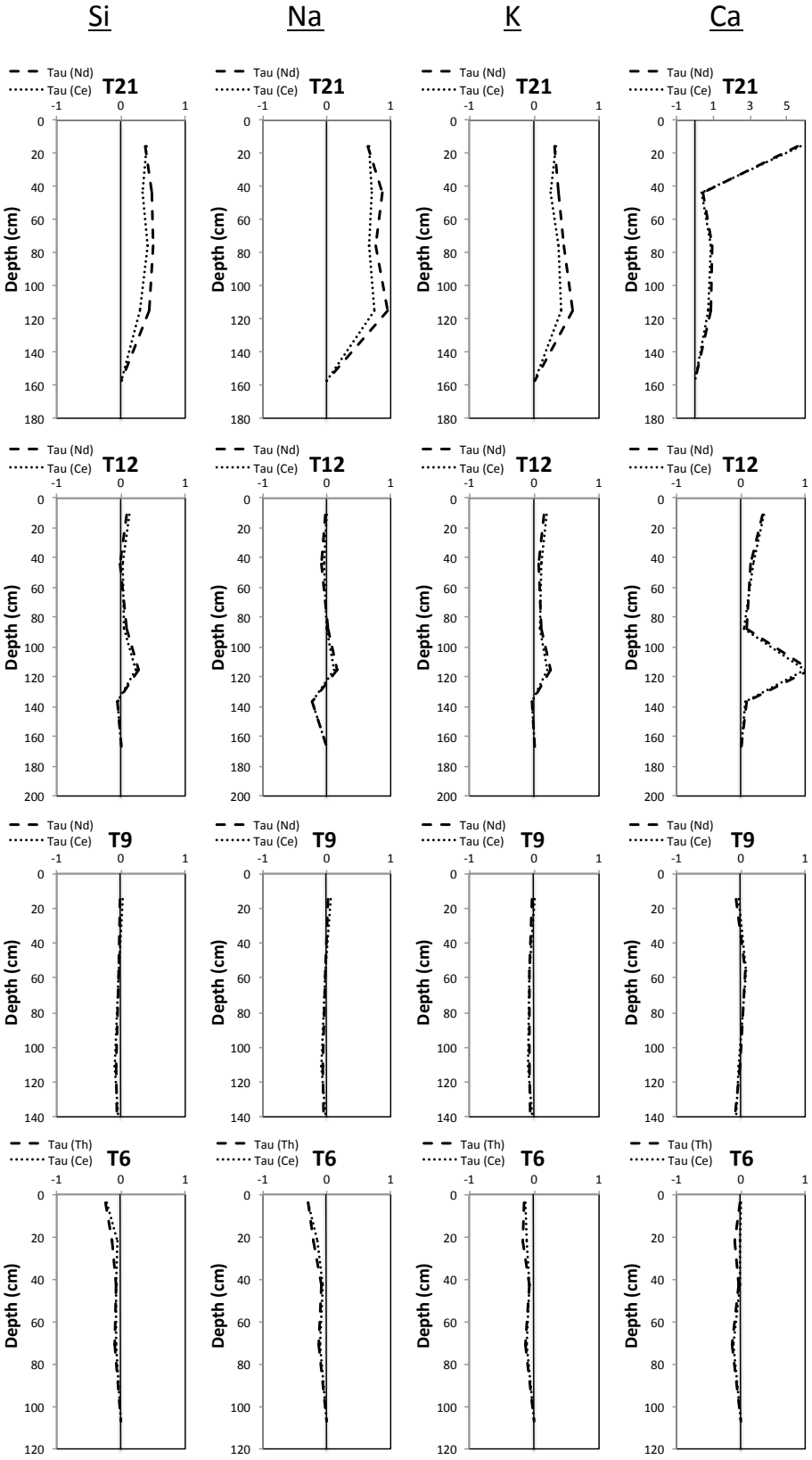

Table 1a. Geochemistry data for El Tesoro Paleosols

Paleosol-sample #	Paleosol Horizon	Depth from surface (cm)	SiO2 %	Al2O3 %	Fe2O3 %	CaO %	MgO %	Na2O %	K2O %	Cr2O3 %	TiO2 %	MnO %	P2O5 %	SrO %	BaO %	Ag ppm	As ppm	Bi ppm	C %	S %
22-1	C	0 - 10	50.3	14.05	6.02	7.67	1.79	3.03	2.6	<0.01	0.65	0.12	0.18	0.02	0.05	<0.5	145.5	0.61	1.34	0.23
22-2	A	10 - 18	59.8	14.85	6.77	1.8	1.72	3.58	2.86	0.01	0.76	0.11	0.11	0.03	0.06	<0.5	73.7	0.4	0.03	0.15
22-3	Bt	18 - 39	56.3	15.65	6.91	1.32	2.23	3.45	3.19	<0.01	0.7	0.1	0.07	0.04	0.06	<0.5	71.3	0.43	0.04	0.17
22-4	Bkm	39 - 54	42.6	10.7	5.19	17.15	1.39	2.58	2	<0.01	0.54	0.08	0.1	0.07	0.05	<0.5	79.7	0.3	3.34	0.33
22-5	Bk1	54 - 72	42.4	10.35	5.09	17.75	1.44	2.63	1.96	<0.01	0.53	0.08	0.1	0.03	0.05	<0.5	78	0.29	3.4	0.44
22-6	Bk2	72 - 88	49.6	13.25	5.97	8.79	1.77	3.31	2.43	<0.01	0.61	0.1	0.09	0.03	0.06	<0.5	81.6	0.34	1.53	0.37
22-7	Ab	88 - 100	47.8	11.8	5.53	12.75	1.62	3.03	2.12	<0.01	0.59	0.08	0.09	0.03	0.05	<0.5	80.4	0.3	2.31	0.53
22-8	Bkmb1	100 - 118	59.1	14	6.63	2.94	1.69	3.7	2.67	<0.01	0.74	0.1	0.07	0.03	0.06	<0.5	72.2	0.34	0.29	0.25
22-9	Bkmb2	118 - 134	47.8	11.5	5.36	13.6	1.46	3.1	2.04	<0.01	0.6	0.09	0.1	0.03	0.05	<0.5	75.3	0.31	2.46	0.48
22-10	Bkmb3	134 - 162	47.7	11.6	5.66	13.05	1.62	3.07	2.02	<0.01	0.6	0.09	0.15	0.03	0.05	<0.5	87.3	0.3	2.23	0.71
22-11	BC or C	162 - 200	48.8	11.9	5.94	12.4	1.57	2.57	2.12	<0.01	0.63	0.09	0.19	0.03	0.06	<0.5	102.5	0.4	2.18	0.5
21-1	C	0 - 28	53	13.8	5.96	6.14	1.55	2.75	2.28	<0.01	0.68	0.09	0.25	0.03	0.07	<0.5	104	0.51	0.34	2.05
21-2	AB	28 - 60	50.7	13.05	6.56	6.81	1.55	3.11	2.17	<0.01	0.64	0.11	0.18	0.03	0.06	<0.5	81.8	0.43	0.1	2.84
21-3	Bty	60 - 84	59.4	14.7	7.11	1.65	1.71	3.9	2.48	<0.01	0.75	0.11	0.11	0.03	0.06	<0.5	63.5	0.48	0.04	0.2
21-4	Bt1	84 - 123	58.5	15.95	7.66	2.13	2.01	3.54	2.54	<0.01	0.7	0.13	0.16	0.03	0.07	<0.5	73.4	0.45	0.03	0.35
21-5	Bt2	123 - 163	56.5	15.8	7.45	2.08	2.04	3.95	2.79	<0.01	0.73	0.13	0.16	0.03	0.07	<0.5	62.5	0.39	0.05	0.29
21-6	BC or C	163 - 208	58.5	14.9	7.79	1.64	1.82	3.02	2.62	<0.01	0.78	0.12	0.19	0.03	0.07	<0.5	61.8	0.34	0.03	0.17
20-1	C	0 - 20	53.1	14.2	7.2	5.05	1.84	3.88	2.4	<0.01	0.71	0.14	0.21	0.04	0.07	<0.5	122.5	0.47	0.69	0.47
20-2	A	20 - 48	59.5	14.6	6.54	1.44	1.63	3.78	2.55	<0.01	0.73	0.1	0.12	0.04	0.06	<0.5	70.1	0.38	0.07	0.09
20-3	Bt1	48 - 67	54.6	13.45	6.85	5.53	1.56	3.58	2.28	<0.01	0.68	0.1	0.14	0.03	0.06	<0.5	80.7	0.37	0.94	0.15
20-4	Bt2	67 - 90	54.1	13.95	6.92	4.69	1.7	3.74	2.4	<0.01	0.67	0.1	0.14	0.03	0.07	<0.5	84.7	0.45	0.68	0.31
20-5	Btk	90 - 119	51.6	13.05	7.4	8.85	1.7	2.91	2.26	<0.01	0.67	0.09	0.2	0.03	0.05	<0.5	111	0.45	1.63	0.22
20-6	Bk1	119 - 134	49.8	11.7	6.16	9.17	1.53	3.68	2.04	<0.01	0.71	0.09	0.16	0.04	0.05	<0.5	80	0.26	1.79	0.12
20-7	Bk2	134 - 157	56.6	13.5	7.4	5.01	1.73	2.91	2.31	<0.01	0.74	0.09	0.14	0.03	0.06	<0.5	79.7	0.26	0.86	0.2
20-8	Bk3	157 - 194	57	13.55	7.68	4.19	1.77	2.89	2.27	<0.01	0.73	0.1	0.16	0.04	0.08	<0.5	79.6	0.28	0.69	0.2
20-9	Bk4	194- 214	48.4	12.15	5.83	10.05	1.69	2.5	2.1	<0.01	0.66	0.07	0.19	0.04	0.06	<0.5	63.1	0.23	1.92	0.27
18-2	Bk1	0 - 8	60.6	13.3	6.55	2.95	1.44	2.53	2.24	<0.01	0.76	0.07	0.16	0.03	0.07	<0.5	38.1	0.28	0.49	0.14
18-3	Bkm	8 - 31	65	13.65	4.81	2.7	1.55	4.3	2.44	<0.01	0.51	0.1	0.13	0.03	0.07	<0.5	17.5	0.06	0.26	0.04
18-4	Bk'	31 - 47	68.4	14.1	3.58	1.81	0.95	4.35	2.76	<0.01	0.38	0.09	0.1	0.03	0.07	<0.5	14.2	0.07	0.09	0.03

Table 1b. Geochemistry data for El Tesoro Paleosols

Paleosol-sample #	Ba ppm	Ce ppm	Cd ppm	Co ppm	Cr ppm	Cs ppm	Cu ppm	Dy ppm	Er ppm	Eu ppm	Ga ppm	Gd ppm	Hf ppm	Hg ppm	Ho ppm	La ppm	Lu ppm	Mo ppm	Nb ppm	Nd ppm	Ni ppm	Pr ppm
22-1	434	43.4	1.5	15	30	6.16	244	2.88	1.63	0.93	15.5	3.53	3.3	0.017	0.58	22.5	0.26	8	9	21.3	16	5.35
22-2	533	54.1	<0.5	13	30	5.57	219	3.13	1.77	0.94	17.3	3.46	5.5	0.011	0.63	23.5	0.3	5	10.1	21.7	11	5.56
22-3	512	56.1	<0.5	15	30	7.25	447	2.94	1.78	0.88	19.7	3.32	4.4	0.015	0.62	24.5	0.31	8	9.9	21.4	15	5.54
22-4	449	37.2	2.1	10	20	4.13	375	2.54	1.51	0.84	12.3	3.13	3.2	0.013	0.51	20.5	0.25	7	6.8	18.6	6	4.67
22-5	403	34.2	1.7	10	20	3.96	409	2.28	1.39	0.79	12.3	2.75	3	0.014	0.48	18	0.22	9	6.7	16.7	7	4.22
22-6	519	43.4	1.1	11	30	6.53	368	2.64	1.54	0.88	15.9	3.19	3.7	0.015	0.55	21.8	0.27	7	8.1	19.5	9	5.09
22-7	447	35	1	9	20	4.77	401	2.37	1.4	0.82	13.4	2.88	3.3	0.014	0.48	18.8	0.24	9	7.1	16.8	7	4.29
22-8	530	53.1	<0.5	14	30	5.84	307	3.04	1.75	0.93	16.3	3.4	4.9	0.007	0.6	23.6	0.29	9	9.8	21.6	11	5.57
22-9	447	38.1	1.2	11	20	4.63	332	2.83	1.55	0.92	13.5	3.41	3.6	0.01	0.57	20.9	0.26	8	7.6	19.6	7	4.99
22-10	476	36.6	1.1	10	20	4.28	417	2.6	1.48	0.93	13.3	3.19	3.2	0.012	0.54	19.6	0.23	10	7	18.3	7	4.58
22-11	503	39.5	1.3	11	20	4.67	287	2.77	1.49	1.03	13.4	3.53	3.3	0.015	0.56	20.2	0.23	11	7.2	20.1	5	5.04
21-1	492	36.7	0.8	11	20	4.07	253	4.01	2.3	1.62	17.9	5.36	4.3	0.019	0.78	18.8	0.31	9	10.1	17.1	10	4.77
21-2	394	31.9	<0.5	14	20	3.32	205	3.78	2.09	1.54	16.3	5.32	3.6	0.014	0.74	16.1	0.27	7	8.7	15	10	4.17
21-3	430	39.1	<0.5	14	30	4.39	196	4.08	2.36	1.61	20.1	5.53	4.6	0.015	0.78	18.3	0.31	6	11.1	16.4	14	4.69
21-4	426	36.6	<0.5	16	20	4.3	201	3.87	2.19	1.57	20.2	5.22	4.4	0.02	0.74	17.6	0.29	6	9.8	15.8	13	4.41
21-5	475	38.8	0.5	18	30	4.88	578	4.05	2.26	1.5	20.2	5.34	4.9	0.027	0.78	17.8	0.31	9	10.6	15.9	13	4.46
21-6	644	51.8	<0.5	13	30	4.25	1060	3.33	1.96	1.1	19.5	4.11	4	0.016	0.69	25.1	0.31	19	10.1	23.8	20	6.01
20-1	465	34.5	1	16	30	4.56	466	4.19	2.38	1.63	19.9	5.82	3.9	0.083	0.81	16.7	0.31	8	10.7	15.4	11	4.28
20-2	372	36.2	<0.5	14	30	4.19	177	3.84	2.17	1.4	19.4	5	5.5	0.024	0.75	16.5	0.3	6	10.9	14.5	14	4.18
20-3	362	32.8	1.1	13	20	3.59	275	3.71	2.13	1.43	18.4	4.89	4.5	0.022	0.72	16.1	0.29	6	9.9	14.4	10	4.04
20-4	466	32.7	0.9	15	30	4.23	335	3.5	1.97	1.34	18.7	4.66	4.1	0.024	0.7	15.7	0.27	7	9.7	13.9	11	3.93
20-5	486	41.4	1.2	12	30	5.56	575	3.02	1.76	1.05	15.5	3.31	3.3	0.014	0.6	21.3	0.25	10	9	20.5	7	5.13
20-6	394	31.6	0.8	13	20	3.18	729	3.37	1.92	1.32	15.4	4.46	3.8	0.018	0.66	15.5	0.26	14	8.8	14	7	3.86
20-7	434	34.3	0.5	13	20	3.75	935	3.33	1.96	1.3	17.4	4.34	4	0.016	0.65	16.5	0.28	17	9.2	14.2	8	3.98
20-8	529	33.5	<0.5	12	20	3.63	1005	3.22	1.9	1.32	16.9	4.2	4	0.017	0.64	16.3	0.27	17	8.9	14.1	8	3.98
20-9	454	31.5	0.7	11	20	3.81	1090	3.56	2.09	1.42	16.7	4.6	3.8	0.016	0.69	15.8	0.28	15	8.8	14.8	6	4.06
18-2	430	30.7	<0.5	10	20	2.91	895	3.06	1.78	1.27	18.6	4.13	4.5	0.014	0.59	15.1	0.25	25	9.8	13	7	3.67
18-3	420	31.7	<0.5	9	20	2.22	28	4.4	2.56	1.33	19.5	5.27	6	0.007	0.84	15.9	0.35	1	9.9	14.5	6	4.05
18-4	453	31	<0.5	7	10	2.23	24	3.91	2.33	1.24	18.7	5.05	5.4	0.006	0.77	14.5	0.32	1	8.8	12.9	4	3.71

Table 1c. Geochemistry data for El Tesoro Paleosols

Paleosol-sample #	Rb ppm	Pb ppm	Sb ppm	Se ppm	Sm ppm	Sn ppm	Sr ppm	Ta ppm	Tb ppm	Te ppm	Th ppm	Tl ppm	Tm ppm	U ppm	V ppm	W ppm	Y ppm	Yb ppm	Zn ppm	Zr ppm	LOI %
22-1	93.3	60	2.59	1.2	4.13	2	175.5	0.7	0.52	0.32	6.49	<0.5	0.25	2.18	132	2	17.5	1.69	308	125	11.85
22-2	98	43	1.68	0.8	4.13	2	250	0.7	0.54	0.22	9.22	<0.5	0.29	2.59	139	4	17.8	1.9	176	209	7.4
22-3	112.5	43	1.69	0.8	3.95	3	324	0.7	0.51	0.26	9.45	<0.5	0.3	2.61	133	6	17.2	2.03	188	173	9.9
22-4	69.6	43	1.63	0.9	3.32	2	574	0.5	0.45	0.29	5.67	<0.5	0.24	1.76	109	3	15.2	1.54	137	122	18.5
22-5	69.2	38	1.64	0.9	3.2	2	226	0.5	0.41	0.28	5.29	<0.5	0.23	1.67	108	3	14	1.45	143	116	17.9
22-6	89.6	42	1.87	0.9	3.76	2	264	0.6	0.49	0.23	6.85	<0.5	0.27	2.03	125	2	15.6	1.65	168	140	13.3
22-7	75.8	36	1.85	0.9	3.21	2	259	0.5	0.41	0.23	5.76	<0.5	0.23	1.78	114	3	14.2	1.55	153	126	15
22-8	95.8	49	1.83	0.9	4.14	2	266	0.7	0.52	0.2	8.86	<0.5	0.29	2.38	137	3	17.2	1.83	171	193	8.2
22-9	73.6	37	1.79	1	3.89	2	276	0.6	0.52	0.23	5.89	<0.5	0.26	1.84	110	3	17	1.67	158	139	14.95
22-10	71.9	42	2.09	1.1	3.5	2	275	0.5	0.47	0.24	5.38	<0.5	0.25	1.73	113	7	15.4	1.52	183	123	14.8
22-11	78.9	48	2.46	1.2	3.95	2	251	0.5	0.51	0.32	5.37	<0.5	0.24	1.74	125	4	16.4	1.48	197	124	13.1
21-1	104	48	1.92	2.4	3.55	2	356	0.6	0.78	0.36	6.68	<0.5	0.35	2.09	121	3	22.1	1.96	231	178	13.05
21-2	92.5	51	1.92	2.9	3.14	2	330	0.5	0.74	0.32	6.41	<0.5	0.31	1.83	113	3	20.8	1.77	191	159	12.7
21-3	115.5	44	1.63	1.1	3.36	2	350	0.6	0.79	0.27	8.93	<0.5	0.35	2.1	135	3	24.4	2.07	186	212	7.9
21-4	110	49	1.83	1.2	3.24	2	357	0.6	0.73	0.29	7.68	<0.5	0.32	2	125	3	21.6	1.89	199	188	8.17
21-5	116.5	44	1.58	1.2	3.3	2	331	0.6	0.78	0.33	8.87	<0.5	0.33	2.17	124	3	23.1	2.03	184	214	9.69
21-6	103	53	1.63	1	4.48	3	280	0.7	0.61	0.38	7.36	<0.5	0.32	2.05	163	4	19.8	2.01	163	159	7.3
20-1	114.5	55	2.43	1.4	3.33	2	391	0.6	0.79	0.43	7.19	<0.5	0.35	2.47	134	2	24.7	2.07	277	175	11.7
20-2	116.5	47	1.5	1.1	2.98	2	408	0.7	0.69	0.27	9.45	<0.5	0.33	2.3	121	3	22.7	1.96	180	250	7.36
20-3	103.5	49	1.68	1.2	3.03	2	367	0.6	0.7	0.27	7.66	<0.5	0.32	2.04	123	1	21.9	1.88	184	204	10.4
20-4	105	48	1.76	1.5	2.92	2	382	0.6	0.66	0.29	7.49	<0.5	0.31	2.05	121	4	20.5	1.81	202	194	11.2
20-5	83.4	43	2.66	1.3	4.4	2	290	0.5	0.52	0.33	6.34	<0.5	0.26	1.84	148	3	16	1.67	204	139	12.1
20-6	82.6	46	1.53	1	2.87	2	354	0.5	0.65	0.3	6.05	<0.5	0.29	1.71	114	5	18.1	1.68	127	171	14.6
20-7	94.8	48	1.78	1.1	2.9	2	351	0.5	0.61	0.3	6.46	<0.5	0.31	1.9	130	4	17.6	1.78	138	176	9.97
20-8	91.4	50	1.75	1	2.96	2	384	0.5	0.6	0.34	5.98	<0.5	0.29	1.88	130	5	17.2	1.7	151	174	8.76
20-9	90.9	37	1.34	0.9	3.01	3	375	0.5	0.67	0.27	5.82	<0.5	0.31	1.75	116	2	20.1	1.76	133	170	15.35
18-2	102.5	50	2.32	1	2.67	3	325	0.5	0.58	0.35	7.4	<0.5	0.27	2.14	120	5	19.4	1.65	101	226	7.71
18-3	112	15	0.39	0.6	3.08	1	287	0.6	0.79	0.11	8.06	<0.5	0.4	1.55	66	3	27.9	2.34	98	288	4.19
18-4	124.5	15	0.36	0.5	2.73	1	287	0.6	0.72	0.07	9.24	<0.5	0.34	1.5	52	2	24.2	2.09	64	257	3.29

Table 1d. Geochemistry data for El Tesoro Paleosols

Paleosol-sample #	Paleosol Horizon	Depth from surface (cm)	SiO2 %	Al2O3 %	Fe2O3 %	CaO %	MgO %	Na2O %	K2O %	Cr2O3 %	TiO2 %	MnO %	P2O5 %	SrO %	BaO %	Ag ppm	As ppm	Bi ppm	C %	S %
17-1	C	0 - 12	56.1	13.85	7.34	3.93	1.72	2.92	2.23	<0.01	0.73	0.08	0.28	0.03	0.08	<0.5	60.8	0.38	0.55	0.33
17-2	A	12 - 19	59.4	13.95	7.19	1.4	1.56	3.15	2.35	<0.01	0.73	0.08	0.16	0.03	0.07	<0.5	42.5	0.28	0.06	0.17
17-3	Bt/Bw	19 - 32	59.7	13.75	7.72	1.97	1.55	3.16	2.26	<0.01	0.77	0.08	0.17	0.03	0.07	<0.5	48.3	0.29	0.18	0.13
17-4	Bk1	32 - 55	56.7	12.8	7.05	5.68	1.48	2.91	2.11	<0.01	0.72	0.07	0.2	0.03	0.07	<0.5	43.8	0.25	1.03	0.11
17-5	Bk2	55 - 83	58.6	12.8	7.24	4.29	1.36	2.92	2.13	<0.01	0.71	0.08	0.19	0.03	0.08	<0.5	43.5	0.25	0.7	0.15
17-6	Bk3	83 - 111	59.6	12.5	7.94	3.59	1.29	2.75	2.17	<0.01	0.73	0.07	0.22	0.03	0.08	<0.5	40.5	0.27	0.54	0.17
17-7	Bk4	111 - 134	59.1	13.6	7.12	3.92	1.53	2.62	2.37	<0.01	0.71	0.08	0.24	0.03	0.07	<0.5	47.5	0.43	0.6	0.18
17-8	Bk5	134 - 163	65.6	13.4	4.36	2.69	1.21	4.14	2.51	<0.01	0.47	0.11	0.1	0.03	0.07	<0.5	14.7	0.05	0.25	0.04
14-1	C	0 - 16	61.3	14.1	5.76	2.53	1.56	3.89	2.48	<0.01	0.65	0.09	0.22	0.03	0.08	<0.5	22.6	0.18	0.19	0.26
14-2	A	16 - 30	56.9	14.65	5.72	3.1	1.87	3.7	2.49	<0.01	0.65	0.09	0.24	0.02	0.07	<0.5	16.2	0.15	0.42	0.21
14-3	Bk1	30 - 67	57.6	14.95	5.02	3.25	1.77	3.75	2.48	<0.01	0.58	0.13	0.2	0.03	0.08	<0.5	13.9	0.13	0.39	0.28
14-4	Bk2	67 - 94	57.5	14.6	5.95	2.94	1.77	3.72	2.41	<0.01	0.6	0.18	0.2	0.03	0.14	<0.5	22.2	0.17	0.27	0.41
14-5	Bk3	94 - 120	62.4	13.95	6.02	1.8	1.38	3.78	2.55	<0.01	0.58	0.12	0.16	0.03	0.09	<0.5	16.6	0.14	0.06	0.26
14-6	Bk4	120 - 153	60.5	14.25	5.99	2.74	1.62	3.81	2.45	<0.01	0.63	0.1	0.2	0.03	0.08	<0.5	16.1	0.14	0.32	0.14
14-7	Bk5	153 - 171	59.1	14.95	6.46	2.14	1.94	4.03	2.44	<0.01	0.7	0.11	0.22	0.03	0.08	<0.5	18.1	0.16	0.12	0.23
12-1	C	0-18	65.8	13.35	3.82	0.92	1.05	4.24	2.72	<0.01	0.4	0.09	0.09	0.02	0.06	<0.5	9.5	0.1	0.02	0.02
12-2	A	18-41	66.2	13.1	3.95	1.38	1.07	3.94	2.77	<0.01	0.45	0.08	0.13	0.02	0.06	<0.5	8.8	0.11	0.12	0.02
12-3	Bt1	41-83	64.5	13.6	3.88	1.28	1.03	4.01	2.75	<0.01	0.38	0.07	0.1	0.02	0.06	<0.5	10.7	0.13	0.02	0.17
12-4	BC	83-128	66.2	13.5	3.92	1.14	1.09	4.22	2.7	<0.01	0.41	0.08	0.08	0.02	0.07	<0.5	11.4	0.11	0.04	0.02
12-5	C1	128-139	68.7	13.05	3.47	1.92	0.74	4.18	2.67	<0.01	0.33	0.07	0.08	0.02	0.08	<0.5	9.5	0.1	0.22	0.02
12-6	C2	139-170	67.3	13.8	4.4	1.32	1.21	3.66	2.74	<0.01	0.47	0.1	0.09	0.02	0.06	<0.5	11.7	0.12	0.06	0.01
12-7	C3	170-200	66.4	13.6	3.94	1.14	1.1	4.46	2.64	<0.01	0.43	0.09	0.09	0.02	0.06	<0.5	13.5	0.11	0.04	0.02
10-1	C	0 - 16	70	13.7	3.71	1.32	1.01	4.21	2.76	<0.01	0.43	0.07	0.03	0.02	0.07	<0.5	12.1	0.18	0.02	0.2
10-2	A	16 - 28	68.2	13.6	4.56	1.02	1.02	3.9	2.66	<0.01	0.51	0.07	0.04	0.02	0.07	<0.5	9.7	0.17	0.02	0.01
10-3	Bt	28 - 77	65.7	13.9	4.21	1.37	1.27	3.92	2.65	<0.01	0.53	0.07	0.06	0.02	0.07	<0.5	7.8	0.15	0.06	0.04
10-4	Btk	77 - 96	52.4	11.05	3.52	11.05	1.11	3.48	2.17	<0.01	0.42	0.06	0.07	0.02	0.05	<0.5	6.5	0.13	2.27	0.03
10-5	Bk1	96 - 126	65.1	13.3	3.81	2.34	1.16	4.14	2.67	<0.01	0.44	0.07	0.07	0.02	0.06	<0.5	7.1	0.13	0.3	0.02
10-6	Bk2	126 - 152	68.1	13.45	4.04	1.34	1	4.1	2.84	<0.01	0.39	0.07	0.08	0.02	0.06	<0.5	6	0.11	0.02	0.05
10-7	Bk3	152 - 177	65.5	13.6	4.6	2.13	1.39	3.93	2.68	<0.01	0.53	0.07	0.04	0.02	0.06	<0.5	6.5	0.12	0.19	0.03
10-8	Bk4	177 - 190	62.5	13.3	4.41	3.84	1.21	3.44	2.69	<0.01	0.43	0.08	0.09	0.03	0.06	<0.5	5.2	0.07	0.02	1.4

Table 1e. Geochemistry data for El Tesoro Paleosols

Paleosol-sample #	Ba ppm	Ce ppm	Cd ppm	Co ppm	Cr ppm	Cs ppm	Cu ppm	Dy ppm	Er ppm	Eu ppm	Ga ppm	Gd ppm	Hf ppm	Hg ppm	Ho ppm	La ppm	Lu ppm	Mo ppm	Nb ppm	Nd ppm	Ni ppm	Pr ppm
17-1	715	46.3	0.5	11	30	3.96	1280	4.67	2.66	1.6	15.2	5.31	3.4	0.026	0.91	28.8	0.34	23	8.1	27.8	7	7.02
17-2	659	47.1	<0.5	9	30	4.94	1040	3.37	1.92	1.15	16.3	3.52	4.4	0.015	0.66	26.1	0.29	19	9.2	22.9	8	6.07
17-3	456	31.2	<0.5	11	20	2.72	1005	3.44	1.98	1.36	21.1	4.44	4.3	0.016	0.68	16.2	0.28	21	9.8	13.9	8	3.84
17-4	433	29.3	0.6	10	20	2.44	982	3.7	2.17	1.46	19	4.95	4.2	0.017	0.72	15.1	0.28	20	9.2	13.8	7	3.75
17-5	486	29.9	<0.5	12	20	2.5	1060	3.54	2.05	1.38	19.1	4.7	3.8	0.02	0.67	14.8	0.28	22	9.1	13.1	7	3.66
17-6	476	28.8	<0.5	9	20	1.89	986	3.08	1.75	1.3	18.9	4.25	3.9	0.017	0.6	14.7	0.25	24	9.1	13.1	5	3.67
17-7	450	30.8	0.5	10	20	3.26	1225	3.42	1.96	1.46	20.1	4.71	4.2	0.02	0.66	15.6	0.27	24	9.2	14.4	7	3.95
17-8	429	30.1	<0.5	8	20	1.95	25	4.11	2.46	1.24	19.1	4.95	7.1	0.007	0.79	13.4	0.35	2	10.1	12.7	4	3.53
14-1	701	46	<0.5	10	20	3.11	455	3.52	1.95	1.19	15.5	4.35	4.3	0.033	0.71	25.2	0.31	8	8	23.8	6	6.06
14-2	634	50.6	<0.5	12	30	4.08	392	3.98	2.25	1.23	16.4	4.97	4.4	0.027	0.8	30.1	0.35	6	9.6	27.8	10	7.02
14-3	681	51.2	<0.5	11	20	4.08	293	3.93	2.18	1.25	17.2	5.02	3.9	0.025	0.79	31	0.36	7	8.4	28	9	7.24
14-4	1280	53.6	<0.5	14	20	4	431	3.97	2.26	1.28	17.3	4.75	4.4	0.024	0.81	32.6	0.37	13	8.3	28.4	11	7.27
14-5	862	53.4	<0.5	11	30	3.94	344	3.73	2.06	1.08	16.6	4.21	4.7	0.016	0.74	28	0.33	6	8.7	27.2	8	6.97
14-6	633	48.8	<0.5	12	20	3.42	224	3.79	2.03	1.19	15.2	4.31	3.9	0.013	0.74	28	0.33	5	7.8	25.3	9	6.45
14-7	724	57.3	<0.5	15	30	4.28	256	4.37	2.36	1.4	17.6	5.42	4.7	0.012	0.86	31.3	0.37	6	9.3	30.2	9	7.64
12-1	540	55.6	<0.5	7	10	3.82	34	4.68	2.83	1.15	11.9	4.86	5.7	0.008	0.9	29.8	0.39	3	9.5	27.3	5	6.96
12-2	395	34	<0.5	7	20	2.84	28	4.85	2.87	1.34	19.6	5.88	7.2	0.008	0.98	18.9	0.43	2	10.9	16.5	6	4.6
12-3	388	36.2	<0.5	7	20	3.29	37	5.25	3.08	1.51	20.9	6.47	5.2	0.011	1.05	21.5	0.43	2	10	17.7	7	5.08
12-4	418	36.3	<0.5	7	10	2.92	31	4.85	2.99	1.35	20.9	5.79	6.2	0.006	0.97	20.5	0.43	3	10.7	16.7	5	4.81
12-5	480	32.3	<0.5	6	10	2.28	46	3.97	2.45	1.16	18.5	4.8	5.4	0.009	0.8	18	0.35	3	9	14.6	3	4.22
12-6	389	41.4	<0.5	9	20	3.24	43	5.13	3.05	1.44	22.1	6.26	6.4	0.006	1.01	22.8	0.45	2	12.6	19.3	6	5.62
12-7	395	38.4	<0.5	9	10	2.96	46	4.79	2.95	1.39	22	5.82	5.8	0.01	0.97	21.4	0.42	4	11.1	18.1	4	5.15
10-1	397	31.1	<0.5	6	10	2.79	25	3.41	2.19	0.76	25.5	3.52	6.1	0.005	0.69	15.3	0.33	4	9.4	13	4	3.83
10-2	424	36	<0.5	7	20	3.18	23	4.05	2.61	0.83	25	3.96	7.7	<0.005	0.81	17.6	0.38	3	11	14.4	7	4.35
10-3	433	33.8	<0.5	8	20	3.81	29	3.64	2.3	0.86	25.9	3.91	5.5	<0.005	0.74	18.4	0.32	3	10	14.4	8	4.28
10-4	312	28.1	0.5	6	20	2.91	35	3.76	2.51	0.84	20.9	4.11	4.7	0.009	0.79	19.8	0.32	3	8.2	14.8	8	4.32
10-5	378	31.8	<0.5	7	20	3.24	40	3.54	2.29	0.82	25.2	3.83	4.7	0.005	0.74	16.2	0.31	3	9.1	13.5	6	3.86
10-6	397	34.5	<0.5	6	20	2.6	45	3.98	2.49	0.86	24.2	4.21	5.1	0.009	0.81	17.6	0.34	3	9.4	14.9	6	4.45
10-7	366	37.1	<0.5	7	20	3.23	38	3.59	2.31	0.78	24.9	3.5	6.4	0.008	0.73	18.1	0.33	3	10.2	13.8	9	4.23
10-8	400	36.4	<0.5	7	20	2.52	54	3.75	2.4	0.9	24.9	4.24	4.5	0.007	0.76	17.9	0.31	3	9.6	16.1	6	4.67

Table 1f. Geochemistry data for El Tesoro Paleosols

Paleosol-sample #	Rb ppm	Pb ppm	Sb ppm	Se ppm	Sm ppm	Sn ppm	Sr ppm	Ta ppm	Tb ppm	Te ppm	Th ppm	Tl ppm	Tm ppm	U ppm	V ppm	W ppm	Y ppm	Yb ppm	Zn ppm	Zr ppm	LOI %
17-1	80.5	37	1.67	1.5	5.98	2	229	0.5	0.82	0.54	5.59	<0.5	0.38	1.93	170	4	27.2	2.3	115	138	8.5
17-2	86.3	34	1.57	1.1	4.84	2	245	0.6	0.59	0.34	6.68	<0.5	0.31	1.91	152	4	19.1	1.89	123	182	7.5
17-3	106	39	1.68	1.2	2.85	2	349	0.6	0.63	0.39	7.26	<0.5	0.3	2.32	156	5	23.4	1.82	110	203	7.78
17-4	95.1	34	1.65	1.2	2.84	2	331	0.5	0.67	0.37	6.67	<0.5	0.31	2.19	140	5	25.5	1.95	99	203	9.78
17-5	94.9	33	1.89	1.2	2.77	2	359	0.5	0.63	0.39	6.74	<0.5	0.3	2.15	139	4	23	1.78	101	195	8.53
17-6	92.1	38	1.98	1.2	2.65	2	340	0.5	0.58	0.35	5.91	<0.5	0.25	1.99	151	4	21.4	1.58	93	193	7.56
17-7	105.5	37	2.25	1.2	3.05	2	345	0.5	0.67	1.01	6.42	<0.5	0.29	2.07	130	7	23.5	1.71	116	202	7.9
17-8	116.5	16	0.43	0.6	2.72	1	304	0.7	0.73	0.11	9.51	<0.5	0.38	1.61	64	<1	26.4	2.26	77	334	3.39
14-1	86.8	22	0.87	0.9	4.76	2	275	0.6	0.66	0.75	6.29	<0.5	0.32	1.59	127	3	21.3	2.02	85	166	6.7
14-2	90.2	20	0.5	0.9	5.44	2	205	0.7	0.72	0.9	8.01	<0.5	0.35	1.61	109	3	23.5	2.29	97	164	9.2
14-3	96.2	20	0.46	0.9	5.43	2	231	0.6	0.73	0.88	7.46	<0.5	0.35	1.62	101	3	23.7	2.26	87	150	9.2
14-4	93	32	0.69	1	5.45	2	267	0.7	0.73	0.96	7.43	<0.5	0.36	1.71	124	3	23.5	2.32	95	165	9.19
14-5	100.5	23	0.56	0.7	5.52	2	252	0.7	0.63	0.56	9.37	<0.5	0.33	1.64	122	2	22	2.22	87	175	5.4
14-6	87.5	26	0.57	0.7	4.86	2	230	0.6	0.66	0.77	8.02	<0.5	0.33	1.69	117	6	21.3	2.21	97	146	6.89
14-7	94.6	29	0.58	0.9	5.95	2	253	0.7	0.79	0.85	7.91	<0.5	0.38	1.74	128	4	25.3	2.46	113	187	7.6
12-1	104.5	22	0.27	1.1	5.43	2	138	0.7	0.75	0.08	10.65	<0.5	0.42	1.4	51	2	25.2	2.64	76	208	5.3
12-2	137	18	0.36	1.2	3.5	2	210	0.7	0.87	0.09	12.95	<0.5	0.47	2.12	60	2	36.7	2.74	78	351	5.27
12-3	139	20	0.35	1.5	3.56	1	224	0.6	0.93	0.11	13.65	<0.5	0.47	2.24	60	3	35.8	2.75	79	252	6
12-4	134	16	0.37	1.2	3.39	2	231	0.7	0.85	0.12	12.4	<0.5	0.45	2.15	60	3	33.2	2.7	81	292	5
12-5	131	19	0.28	0.8	2.93	1	242	0.6	0.71	0.08	10.45	<0.5	0.39	1.73	52	3	28.4	2.24	59	251	4.19
12-6	149	23	0.33	0.7	3.88	2	241	0.8	0.86	0.07	15.45	<0.5	0.49	2.25	65	3	36.6	2.84	85	308	3.39
12-7	137	25	0.39	1.1	3.61	2	245	0.7	0.84	0.11	11.5	<0.5	0.45	1.96	62	2	34.7	2.68	85	278	5.19
10-1	139.5	18	0.27	0.9	2.71	2	280	0.6	0.6	0.09	10.2	<0.5	0.29	1.76	66	4	28	2.11	72	310	3.8
10-2	141.5	18	0.36	0.8	3.01	2	267	0.8	0.7	0.07	14	<0.5	0.33	2.25	80	3	32.3	2.62	71	368	4.35
10-3	146.5	17	0.46	0.9	3.02	2	323	0.7	0.66	0.06	11.5	<0.5	0.29	2.25	75	4	29.9	2.21	66	280	5.71
10-4	117.5	14	0.36	1.1	2.95	1	275	0.6	0.68	0.09	10.35	<0.5	0.31	1.92	64	3	32.5	2.26	57	226	14.2
10-5	149	15	0.36	0.9	2.76	2	307	0.7	0.66	0.06	10.75	<0.5	0.29	1.96	64	3	29.2	2.12	61	236	6.63
10-6	148.5	14	0.31	0.8	3.21	2	289	0.8	0.73	0.05	13.9	<0.5	0.32	1.9	65	4	31.1	2.35	56	253	4.4
10-7	144	18	0.4	0.9	2.8	2	299	0.8	0.63	0.05	13.05	<0.5	0.29	2.09	77	4	29.9	2.27	68	319	7
10-8	136.5	16	0.27	0.8	3.4	2	363	0.8	0.7	0.04	15.15	<0.5	0.3	1.95	71	3	30.7	2.2	62	223	7.49

Table 1g. Geochemistry data for El Tesoro Paleosols

Paleosol-sample #	Paleosol Horizon	Depth from surface (cm)	SiO2 %	Al2O3 %	Fe2O3 %	CaO %	MgO %	Na2O %	K2O %	Cr2O3 %	TiO2 %	MnO %	P2O5 %	SrO %	BaO %	Ag ppm	As ppm	Bi ppm	C %	S %
9-1	C	0 - 17	71.6	13.4	3.4	1.06	0.87	3.96	2.8	<0.01	0.38	0.09	0.07	0.02	0.07	<0.5	7.2	0.12	0.02	0.01
9-2	Bt1	17 - 46	65.8	14.65	4.82	1.61	1.24	3.7	2.88	<0.01	0.39	0.08	0.08	0.03	0.06	<0.5	8.4	0.13	0.03	0.02
9-3	Bt2	46 - 100	64.7	14.45	4.82	1.9	1.33	3.6	2.83	<0.01	0.42	0.08	0.08	0.03	0.07	<0.5	8	0.12	0.02	0.19
9-4	Btb1	100 - 155	63.6	14.55	5.11	1.76	1.61	3.5	2.85	<0.01	0.48	0.1	0.08	0.03	0.07	<0.5	10.3	0.13	0.06	0.02
9-5	Btb2	155 - 190	64.5	14.75	4.82	1.54	1.57	3.58	2.94	<0.01	0.45	0.09	0.08	0.02	0.06	<0.5	8.9	0.12	0.04	0.01
9-6	Btb3	190 - 218	65.7	14.7	4.88	1.72	1.53	3.59	2.96	<0.01	0.47	0.1	0.1	0.02	0.07	<0.5	8.4	0.1	0.04	0.01
7a-1	C	0 - 15	67.2	13.3	3.58	2.23	1	3.77	2.95	<0.01	0.39	0.08	0.08	0.02	0.06	<0.5	14.9	0.17	0.39	0.03
7a-2	A	15 - 25	68.9	12.95	3.29	1.46	0.85	3.8	3.04	<0.01	0.36	0.06	0.09	0.02	0.06	<0.5	10.6	0.12	0.14	<0.01
7a-3	Bk1	25 - 43	67.2	13.3	3.68	2.09	1.01	3.64	3.01	<0.01	0.38	0.07	0.09	0.02	0.06	<0.5	11.1	0.17	0.26	0.01
7a-4	Bk2	43 - 55	67.4	12.8	3.23	2.94	0.89	3.62	2.95	<0.01	0.36	0.07	0.08	0.02	0.06	<0.5	11.3	0.14	0.48	0.01
7a-5	Bk3	55 - 75	66.5	13.55	3.69	2.55	1.2	3.44	3.01	<0.01	0.42	0.08	0.1	0.02	0.06	<0.5	13.1	0.21	0.36	0.01
7a-6	Bk4	75 - 88	67.2	13.25	3.81	1.72	0.98	3.55	3.07	<0.01	0.4	0.07	0.1	0.02	0.06	<0.5	10.8	0.17	0.19	0.01
6-1	C	0 - 18	67.5	13.95	3.97	1.23	1.2	3.84	2.66	<0.01	0.44	0.08	0.1	0.02	0.06	<0.5	14.1	0.13	0.03	0.02
6-2	Bt1	18 - 26	63.9	14.5	5.12	1.4	1.47	3.18	2.76	<0.01	0.58	0.09	0.15	0.03	0.06	<0.5	12.7	0.2	0.02	0.01
6-3	Bt2	26 - 54	68.6	13.8	4.45	1.23	1.12	3.34	2.54	<0.01	0.5	0.07	0.02	0.02	0.06	<0.5	10.5	0.15	0.02	0.01
6-4	BC	54 - 67	68	14.1	4.48	1.24	1.15	3.72	2.72	<0.01	0.51	0.07	0.09	0.02	0.06	<0.5	11.5	0.14	0.02	0.01
6-5	C1	67 - 110	67.1	13.5	3.99	1.1	1.06	3.54	2.53	<0.01	0.49	0.07	0.19	0.03	0.06	<0.5	12	0.14	0.02	<0.01
6-6	C2	110 - 140	67.2	13.5	4.07	1.15	1	3.64	2.64	<0.01	0.47	0.07	0.1	0.02	0.06	<0.5	11.3	0.13	0.01	<0.01
5-1	C	0 - 10	66.7	13.5	4.01	2.05	1.15	3.47	2.89	<0.01	0.42	0.08	0.11	0.02	0.06	<0.5	11	0.13	0.2	0.05
5-2	A	10 - 25	62.5	13.3	4.9	3.37	1.09	3.19	2.63	<0.01	0.52	0.07	0.21	0.03	0.06	<0.5	9.7	0.15	0.47	0.01
5-3	Bk1	25 - 47	65.4	12.9	2.82	4.79	0.73	3.32	2.62	<0.01	0.29	0.05	0.21	0.03	0.07	<0.5	6	0.08	0.89	0.02
5-4	Bk2	47 - 68	62.2	12.7	3.15	5.95	0.82	3.37	2.74	<0.01	0.32	0.06	0.38	0.03	0.06	<0.5	7.1	0.1	0.98	0.15
5-5	Ab	68 - 83	59.5	14.7	5.55	1.82	2.04	2.81	2.77	<0.01	0.69	0.12	0.18	0.03	0.06	<0.5	14	0.18	0.08	0.02
5-6	Bk1	85 - 108	62.6	12.85	3.87	4.81	0.99	3.31	2.62	<0.01	0.44	0.05	0.12	0.03	0.07	<0.5	6	0.11	0.81	0.02
5-7	Bk2	108 - 151	64.1	13.3	3.49	3.6	1.05	3.6	2.77	<0.01	0.37	0.12	0.19	0.03	0.12	<0.5	8.3	0.12	0.46	0.13
5-8	Bk3	151 - 193	63.2	13	3.53	3.9	0.85	3.67	2.75	<0.01	0.33	0.08	0.17	0.03	0.07	<0.5	7.5	0.11	0.6	0.02

Table 1h. Geochemistry data for El Tesoro Paleosols

Paleosol-sample #	Ba ppm	Ce ppm	Cd ppm	Co ppm	Cr ppm	Cs ppm	Cu ppm	Dy ppm	Er ppm	Eu ppm	Ga ppm	Gd ppm	Hf ppm	Hg ppm	Ho ppm	La ppm	Lu ppm	Mo ppm	Nb ppm	Nd ppm	Ni ppm	Pr ppm
9-1	458	38	<0.5	5	10	3.02	31	4.06	2.66	0.83	26.8	4.08	7.2	<0.005	0.83	21.3	0.4	3	10.8	15.5	4	4.77
9-2	400	41.5	<0.5	7	20	3.51	46	4.28	2.62	0.95	29.1	4.6	4.2	0.007	0.86	25.2	0.35	3	8.9	18.5	6	5.6
9-3	429	43.8	<0.5	7	30	3.46	35	4.03	2.49	0.91	29.2	4.38	4.4	0.006	0.81	26.3	0.33	3	9.5	18.9	6	5.79
9-4	400	45.6	<0.5	9	20	4.07	69	4.11	2.6	0.97	28.7	4.63	4.9	0.009	0.82	28.1	0.36	4	9.7	19.2	9	5.94
9-5	402	42.2	<0.5	9	20	4.03	134	3.83	2.33	0.88	29.9	4.37	4.4	<0.005	0.75	28.7	0.33	4	9	19.2	11	6.02
9-6	428	42.8	<0.5	9	20	3.4	45	4.09	2.49	0.97	28.8	4.57	4.6	0.005	0.81	24.8	0.35	3	9.6	18.4	8	5.53
7a-1	546	69.1	<0.5	6	10	4.44	107	5.39	3.39	1.19	15.5	5.25	6.4	0.009	1.12	32.2	0.49	4	11	30.6	4	8.08
7a-2	544	52.2	<0.5	5	10	3.17	18	3.92	2.54	0.95	14.2	4.18	7.2	0.008	0.83	27.1	0.43	3	9.6	25.2	4	6.79
7a-3	529	59	<0.5	6	10	4.03	36	4.59	3.02	1.07	15.2	4.54	6	0.011	0.98	29.3	0.48	3	10	26.9	5	7.11
7a-4	542	52.4	<0.5	5	10	3.13	30	4.05	2.71	0.98	13.8	4.11	7.3	0.006	0.86	27.8	0.46	3	9.4	24.6	4	6.82
7a-5	530	61.6	<0.5	7	10	4.2	38	4.42	2.85	1.02	15.8	4.53	5.8	0.009	0.94	28.8	0.46	3	9.9	26.5	6	7.07
7a-6	571	56.1	<0.5	5	10	3.89	22	3.83	2.59	0.91	14.6	3.9	6	0.01	0.81	25.4	0.41	3	9.6	23.5	5	6.37
6-1	542	49.7	<0.5	7	10	4	1465	3.4	2.21	0.91	15.2	3.45	5.6	0.011	0.72	21.4	0.37	2	8.8	20.3	35	5.36
6-2	486	51.7	<0.5	10	20	5.72	1555	4.34	2.72	1.13	15.9	4.43	6.8	0.013	0.88	31.1	0.43	2	9.6	26	34	6.83
6-3	543	46	<0.5	8	20	4.58	1605	3.62	2.28	0.95	15	3.64	5.8	0.009	0.74	25.1	0.37	2	8.9	22.2	22	5.87
6-4	547	46.9	<0.5	6	20	4.52	1835	3.7	2.36	0.97	15.1	3.93	6.6	0.009	0.74	25.1	0.39	2	8.9	22.5	23	6.05
6-5	545	46	<0.5	7	10	4.04	1980	3.47	2.24	0.94	14.4	3.47	6.6	0.01	0.73	23	0.38	2	8.8	20.9	25	5.63
6-6	534	42.5	<0.5	7	10	3.68	2010	3.43	2.23	0.91	14.3	3.58	6.2	0.006	0.72	22.2	0.36	2	8.2	20.8	21	5.61
5-1	542	51.9	<0.5	7	10	4.23	2080	3.21	2.11	0.81	14.6	3.06	5.3	0.007	0.69	20.2	0.34	2	8.4	18.1	24	4.93
5-2	519	45.6	0.8	7	20	3.95	2160	4.29	2.9	1.06	14.1	4.39	7	0.011	0.94	32.7	0.45	2	9.2	24.6	19	6.67
5-3	621	39.2	1.2	4	10	3.31	1270	3.77	2.41	1.11	13.4	4.19	3.8	0.007	0.79	33.5	0.37	2	5.7	25.9	10	7.04
5-4	576	39.8	1.5	5	10	3.44	1520	4.13	2.77	1.1	13.2	4.53	5.1	0.007	0.87	37.5	0.43	2	6.2	26.9	14	7.42
5-5	571	61	0.5	13	20	8.26	4060	4.02	2.55	1.07	17.9	4.29	5.5	0.014	0.84	27.9	0.4	3	11.1	25.3	60	6.75
5-6	631	42.2	1.1	6	10	5.28	2220	3.19	2.18	0.92	13.5	3.45	7.1	0.009	0.71	23.2	0.36	2	8.1	20.9	20	5.6
5-7	1145	51.1	0.8	7	10	3.89	2090	3.78	2.4	1.08	14	3.95	4.5	0.013	0.79	29.6	0.36	3	7.3	24.4	17	6.67
5-8	652	42.4	0.9	5	10	3.19	1650	3.5	2.3	0.98	13.8	3.68	4.9	0.008	0.73	27.7	0.36	2	7	22.8	12	6.21

Table 1i. Geochemistry data for El Tesoro Paleosols

Paleosol-sample #	Rb ppm	Pb ppm	Sb ppm	Se ppm	Sm ppm	Sn ppm	Sr ppm	Ta ppm	Tb ppm	Te ppm	Th ppm	Tl ppm	Tm ppm	U ppm	V ppm	W ppm	Y ppm	Yb ppm	Zn ppm	Zr ppm	LOI %
9-1	157	14	0.19	0.7	3.2	2	263	0.7	0.71	0.04	12.35	<0.5	0.35	1.9	51	3	34.5	2.69	59	358	3.39
9-2	157.5	15	0.29	0.8	3.69	2	344	0.7	0.79	0.05	15.95	<0.5	0.33	1.91	80	3	35.5	2.46	64	212	5.29
9-3	156	17	0.31	0.8	3.66	2	349	0.8	0.74	0.04	15.05	<0.5	0.31	1.92	82	3	33.5	2.43	66	223	5.48
9-4	154	19	0.34	0.9	3.79	2	321	0.8	0.75	0.04	16	<0.5	0.33	2.04	85	7	33	2.41	80	246	6.43
9-5	162.5	151	0.31	0.7	3.52	2	317	0.7	0.69	0.04	14.55	<0.5	0.3	1.9	78	4	30.2	2.25	107	209	4.49
9-6	160	18	0.31	0.8	3.56	2	331	0.7	0.76	0.03	14.65	<0.5	0.32	1.88	78	2	33.6	2.32	74	227	4.15
7a-1	103.5	16	0.42	0.8	6.44	2	156	0.7	0.84	0.07	11.55	<0.5	0.51	1.77	46	2	31.2	3.23	62	221	5.72
7a-2	102	13	0.24	0.6	5.17	2	152.5	0.7	0.66	0.05	10.05	<0.5	0.4	1.5	41	1	24	2.69	49	254	4.08
7a-3	104	15	0.26	0.8	5.53	2	160	0.7	0.71	0.07	10.9	<0.5	0.47	1.61	46	1	28.2	3.02	56	210	5.39
7a-4	99.8	14	0.26	0.7	5.05	2	148	0.7	0.67	0.06	9.97	<0.5	0.43	1.53	41	2	24.8	2.84	48	256	5
7a-5	104.5	18	0.27	0.8	5.35	2	158	0.7	0.71	0.09	11	<0.5	0.45	1.63	52	2	27.2	2.94	68	194	5.48
7a-6	105	15	0.28	0.6	4.81	2	154	0.7	0.61	0.07	10.1	<0.5	0.4	1.52	47	1	23.8	2.6	55	211	4.46
6-1	92.6	21	0.44	0.6	4.17	2	193.5	0.6	0.56	0.08	8.63	<0.5	0.35	1.3	59	1	20.2	2.23	692	206	4.96
6-2	98.4	22	0.67	0.7	5.27	2	203	0.7	0.69	0.08	9.91	<0.5	0.43	1.75	75	2	24.8	2.64	598	246	7.35
6-3	97.7	18	0.46	0.5	4.68	1	209	0.7	0.57	0.07	9.35	<0.5	0.35	1.5	67	1	21.6	2.4	420	218	5.08
6-4	95.2	16	0.44	0.5	4.79	2	207	0.6	0.61	0.08	8.82	<0.5	0.38	1.52	68	1	21.4	2.48	455	243	4.25
6-5	93.6	16	0.43	0.5	4.2	2	199	0.6	0.57	0.08	8.79	<0.5	0.36	1.46	63	1	20.3	2.36	514	248	3.97
6-6	90.1	16	0.39	0.5	4.37	2	195	0.6	0.56	0.08	7.97	<0.5	0.34	1.35	62	1	20.2	2.2	497	223	4.18
5-1	103	19	0.39	0.5	3.82	2	189	0.6	0.51	0.07	10.05	<0.5	0.33	1.33	59	1	20.3	2.22	429	194	4.88
5-2	95.5	17	0.48	0.7	4.94	2	210	0.7	0.71	0.07	10.3	<0.5	0.44	1.6	76	1	29.8	2.91	344	253	7.37
5-3	101.5	13	0.24	0.6	5.02	1	227	0.4	0.61	0.04	7.51	<0.5	0.37	1.06	43	1	26.5	2.41	198	132	5.89
5-4	96.6	15	0.47	0.7	5.17	1	206	0.5	0.65	0.06	8.15	<0.5	0.42	1.16	49	1	31.1	2.65	244	186	7.73
5-5	113.5	40	0.49	0.7	5.35	2	230	0.8	0.68	0.06	11	<0.5	0.4	1.82	83	2	24.2	2.51	1160	195	9.53
5-6	93.8	14	0.29	0.5	4.09	2	210	0.6	0.53	0.04	8.92	<0.5	0.34	1.32	59	1	21.2	2.32	430	261	7.67
5-7	98.8	24	0.4	0.6	4.85	1	247	0.5	0.61	0.05	8.35	<0.5	0.37	1.21	52	1	24.7	2.39	302	165	8.13
5-8	98.2	17	0.3	0.5	4.51	1	224	0.5	0.56	0.05	8.16	<0.5	0.34	1.2	50	1	23.4	2.26	241	179	6.19

Table 1j. Geochemistry data for El Tesoro Paleosols

Paleosol-sample #	Paleosol Horizon	Depth from surface (cm)	SiO2 %	Al2O3 %	Fe2O3 %	CaO %	MgO %	Na2O %	K2O %	Cr2O3 %	TiO2 %	MnO %	P2O5 %	SrO %	BaO %	Ag ppm	As ppm	Bi ppm	C %	S %
3a-4	Bw3	52 - 105	63.1	14.05	4.17	2.44	1.14	3.24	2.68	<0.01	0.44	0.07	0.11	0.03	0.07	<0.5	6.8	0.12	0.24	0.05
3a-5	Bkm	105 - 325	38.2	9.01	2.57	22.5	0.86	2.47	1.63	<0.01	0.28	0.05	0.15	0.03	0.05	<0.5	8.8	0.09	4.71	0.07
3a-6	Bk1	325 - 348	60.8	14.1	4.57	3.22	1.23	3.1	2.39	<0.01	0.5	0.07	0.16	0.04	0.06	<0.5	8.9	0.11	0.37	0.01
3a-7	Bk2	348 - 368	60.9	13.95	5.37	3.26	1.19	3.27	2.41	<0.01	0.53	0.08	0.15	0.03	0.07	<0.5	11.1	0.13	0.39	0.02
3a-8	Bk3	368 - 428	61.9	13.95	3.88	2.82	1.28	3.36	2.44	<0.01	0.42	0.08	0.22	0.04	0.07	<0.5	10.8	0.13	0.33	0.04
2-1	Bt1	15-40	58.9	14.5	5.29	2.41	1.41	2.88	2.32	<0.01	0.63	0.08	0.12	0.03	0.05	<0.5	8.5	0.13	0.18	0.08
2-2	2Bkm1	40-55	35	9.37	3.39	23.1	0.96	1.94	1.35	<0.01	0.43	0.07	0.12	0.03	0.05	<0.5	6.2	0.09	4.73	0.04
2-3	2Bkm2	55-95	53	13	4.63	8.43	1.11	2.92	2.08	<0.01	0.53	0.1	0.15	0.03	0.06	<0.5	7.6	0.11	1.51	0.03
2-4	Bk	95-110	57.4	13.9	4.04	5.91	1.22	3.09	2.17	<0.01	0.44	0.09	0.16	0.04	0.06	<0.5	9.5	0.1	0.87	0.26
2-5	Bkm1'	110-125	41.6	10.05	4.17	18.75	1.16	2.14	1.44	<0.01	0.46	0.07	0.2	0.03	0.04	<0.5	14.3	0.11	4.05	0.05
2-6	Bkm2'	125-175	41	10.2	3.59	19.6	1.11	2.05	1.56	<0.01	0.41	0.08	0.14	0.03	0.05	<0.5	11.7	0.09	4.05	0.03

Paleosol-sample #	Ba ppm	Ce ppm	Cd ppm	Co ppm	Cr ppm	Cs ppm	Cu ppm	Dy ppm	Er ppm	Eu ppm	Ga ppm	Gd ppm	Hf ppm	Hg ppm	Ho ppm	La ppm	Lu ppm	Mo ppm	Nb ppm	Nd ppm	Ni ppm	Pr ppm
3a-4	588	38.5	0.6	7	10	8.77	497	2.32	1.49	0.77	14.7	2.48	4.5	0.007	0.48	17.5	0.23	<1	6.9	15.9	5	4.32
3a-5	427	25.8	7	5	10	3.38	271	2.08	1.32	0.74	9.3	2.33	2.4	0.008	0.44	15.6	0.22	<1	4.2	14	3	3.72
3a-6	568	32.6	0.8	8	10	5.22	949	2.44	1.51	0.9	14.7	2.78	3.8	0.012	0.49	17.9	0.23	1	6.3	16.5	5	4.42
3a-7	580	34.6	0.7	9	10	4.97	906	2.47	1.52	0.89	14.4	2.58	4.3	0.014	0.48	18.3	0.22	1	6.3	16.7	6	4.45
3a-8	584	35.5	0.6	8	10	5.43	1175	2.79	1.66	1.03	14.3	3.12	3.6	0.011	0.55	20.3	0.25	1	5.8	19	7	5.14
2-1	457	39.3	0.5	9	20	7.64	1725	2.78	1.73	0.86	15.8	3.04	4.7	0.013	0.56	18.3	0.29	2	8.4	16.4	10	4.43
2-2	389	25.9	5.9	6	10	4.47	342	2.19	1.33	0.69	9.9	2.53	3.1	0.012	0.46	14.8	0.21	<1	5.3	13.4	8	3.52
2-3	495	31.9	3	9	10	4.66	1080	2.59	1.62	0.93	13.9	2.96	3.9	0.009	0.52	17.5	0.25	2	6.5	16.4	9	4.4
2-4	543	31.4	1.9	8	10	4.84	1090	2.51	1.52	0.94	14	2.87	3.4	0.007	0.49	17.3	0.22	1	5.4	16.4	7	4.32
2-5	375	26.3	7.6	8	10	3.91	286	2.06	1.27	0.74	10.6	2.33	2.9	0.012	0.4	14.5	0.19	1	4.8	13.2	5	3.46
2-6	398	26.5	3.9	8	10	5.02	191	2.02	1.2	0.74	10.5	2.33	2.9	0.016	0.4	14.1	0.2	<1	4.7	13.1	7	3.41

Paleosol-sample #	Rb ppm	Pb ppm	Sb ppm	Se ppm	Sm ppm	Sn ppm	Sr ppm	Ta ppm	Tb ppm	Te ppm	Th ppm	Tl ppm	Tm ppm	U ppm	V ppm	W ppm	Y ppm	Yb ppm	Zn ppm	Zr ppm	LOI %
3a-4	103	18	0.28	0.3	3.2	1	252	0.5	0.37	0.04	7.36	<0.5	0.23	1.06	68	2	13	1.45	97	168	7
3a-5	57.3	12	0.4	0.4	2.84	1	226	0.3	0.36	0.08	3.6	<0.5	0.22	0.88	43	1	13	1.39	89	85	22.3
3a-6	85.2	14	0.34	0.4	3.44	1	296	0.4	0.41	0.06	5.96	<0.5	0.23	1.05	80	1	13.9	1.46	97	138	8.19
3a-7	85	17	0.41	0.5	3.34	1	287	0.4	0.4	0.06	5.76	<0.5	0.23	1.05	98	1	14.1	1.48	104	160	7.2
3a-8	88	15	0.48	0.6	3.78	1	277	0.4	0.47	0.06	5.45	<0.5	0.25	1.03	66	1	15.8	1.57	103	131	8.37
2-1	82.3	15	0.37	0.5	3.41	2	270	0.6	0.45	0.06	7.02	<0.5	0.27	1.28	97	2	15.8	1.77	184	177	9.8
2-2	45.5	8	0.25	0.5	2.69	1	252	0.3	0.37	0.14	5.17	<0.5	0.21	0.88	62	1	12.7	1.31	115	115	23.5
2-3	70.2	15	0.42	0.5	3.4	1	269	0.4	0.42	0.07	5.43	<0.5	0.26	1.02	81	1	15.5	1.59	137	143	13.55
2-4	76.4	20	0.31	0.6	3.27	1	278	0.4	0.39	0.07	4.95	<0.5	0.24	1.02	69	1	14	1.49	134	125	11.2
2-5	52.4	15	0.35	0.4	2.71	1	264	0.3	0.33	0.11	4.07	<0.5	0.18	0.98	74	1	11.8	1.19	147	107	20.4
2-6	55.7	21	0.51	0.4	2.6	1	253	0.3	0.34	0.1	4.16	<0.5	0.18	0.9	61	1	11.6	1.25	127	108	19.85